UC San Diego

UC San Diego Electronic Theses and Dissertations

Title

The Nearshore Heat Budget

Permalink

https://escholarship.org/uc/item/7nt521mv

Author

Sinnett, Gregory

Publication Date

2018

Peer reviewed|Thesis/dissertation

eScholarship.org Powered by the California Digital Library
University of California

UNIVERSITY OF CALIFORNIA SAN DIEGO

The Nearshore Heat Budget

A dissertation submitted in partial satisfaction of the
requirements for the degree
Doctor of Philosophy

in

Oceanography

by

Gregory Sinnett

Committee in charge:

Professor Falk Feddersen, Chair
Professor Sarah Giddings
Professor Peter Franks
Professor Andrew Lucas
Professor Geno Pawlak

2018

Copyright
Gregory Sinnett, 2018
All rights reserved.

The dissertation of Gregory Sinnett is approved, and it is acceptable in quality and form for publication on microfilm and electronically:

_____

_____

_____

_____

_____

Chair

University of California San Diego

2018

DEDICATION

To Maia, may the path you choose ignite curiosity and wonder.

TABLE OF CONTENTS

Signature Page iii

Dedication iv

Table of Contents v

List of Figures vii

List of Tables xi

Acknowledgements xii

Vita xiv

Abstract of the Dissertation xv

Chapter 1 The surf zone heat budget: The effect of wave heating 1
- 1.1 Abstract 2
- 1.2 Introduction 2
- 1.3 Experiment 4
- 1.4 Surfzone Heat Budget 6
- 1.5 Results 9
- 1.6 Discussion 12
- 1.7 Summary 18
- 1.8 Acknowledgments 19

Chapter 2 Observations and parameterizations of surfzone albedo 21
- 2.1 Abstract 22
- 2.2 Introduction 22
- 2.3 Methods and Observations 25
  - 2.3.1 Experiment Description 25
  - 2.3.2 Observations 29
- 2.4 Results 31
  - 2.4.1 Albedo dependence on θ_s and waves 31
  - 2.4.2 Image-Based Parameterization 32
  - 2.4.3 Wave Model Based Albedo Parameterization 36
- 2.5 Discussion 41
- 2.6 Summary 44
- 2.7 Acknowledgments 45

Chapter 3 Observations of Nonlinear Internal Wave Runup to the Surfzone 46
3.1 Abstract 47
3.2 Introduction 47
3.3 Experimental Details 50
3.3.1 Location and Overview 50
3.3.2 Instrumentation 52
3.3.3 Background Conditions 54
3.4 Month-long Nonlinear Internal Wave observations from 18 m depth to shore 55
3.5 Coherent Upslope Evolution of Individual Nonlinear Internal Wave Events 64
3.5.1 Example NLIW Event Characteristics 66
3.5.2 Individual NLIW Event Characteristics 71
3.5.3 Upslope NLIW Evolution 76
3.5.4 Scaling upslope NLIW evolution 79
3.6 Discussion 84
3.6.1 Internal runup and comparison to laboratory and numerical studies 84
3.6.2 Potential vertical mixing during the NLIW rundown 87
3.6.3 Complexity of NLIW runup in the internal swashzone . . . 90
3.7 Summary 92
3.8 Acknowledgments 93

Chapter 4 The Competing Effects of Breaking Waves on the Surfzone Heat Budget . 95
4.1 Abstract 96
4.2 Introduction 96
4.3 Methods 100
4.3.1 Instrumentation and Data Processing 100
4.3.2 Analysis 102
4.4 Observations and Results 109
4.4.1 Observed $Q_{\mathrm{sw}}^{\mathrm{d}}$, H_{s}, F_{wave} and Albedo 109
4.4.2 Competing Wave Effects: $\Delta Q_{\mathrm{sw}}^{\mathrm{w}}$ and Q_{wave} 111
4.4.3 Surfzone Adiabatic Temperature Change 114
4.5 Discussion 115
4.5.1 Q_{wave} and $\Delta Q_{\mathrm{sw}}^{\mathrm{w}}$ in Context 116
4.5.2 Scaling for an idealized surfzone 116
4.5.3 Application to the Surfzone Heat Budget 119
4.6 Summary 120
4.7 Acknowledgments 121

Bibliography 122

LIST OF FIGURES

Figure 1.1: Cross-shore x location of pier-mounted thermistors (dots) denoted A ($x = 49$ m), B ($x = 105$ m), C ($x = 160$ m), and D ($x = 216$ m). Bathymetry profile (black) and mean sea-level at $z = 0$ m (blue) and $\pm$ tide level (blue dashed). The outer surfzone boundary L_{sz} is set at $x = 132$ m (vertical dashed). . . . 5

Figure 1.2: Time series of: (a) water temperature at locations A, D, and E, and air temperature at SIO Pier. (b) Pier tidal elevation and significant wave height H_s in 10 m depth. (c) Surfzone energy flux terms $Q_{sw}L_{sz}$, $Q_{lw}L_{sz}$ $Q_{sen}L_{sz}$, $Q_{lat}L_{sz}$, and F_{wave}. (d) Cross-shore integrated dH/dt and F_{net}. 10

Figure 1.3: Surfzone heat budget (1.6): Binned-mean dH/dt versus F_{net} (solid red circles) and standard deviations (vertical red bars). The best-fit line (red dashed) has a slope of 1.20 and an intercept of -6×10^3 W m^{-1}, with best-fit skill of $r^2 = 0.89$. 12

Figure 1.4: A 4-hour cold event on July 8th (indicated by a magenta dot on day 32 in Figure 1.2a): (a) SIO water temperature T at locations A, B, C, and D versus time. (b) Net surfzone heat flux F_{net} (red) and the residual $F_{res} = dH/dt - F_{net}$ (black dashed) versus time t. 15

Figure 1.5: (a) Temperature at A (blue, $x = 49$ m, and $h = 1.5$ m) and D (red, $x = 216$ m, $h = 4$ m) and (b) net surfzone heat flux F_{net} and the residual $F_{res} = dH/dt - F_{net}$ versus time of day. Periods of differential warming (DW, 9:00 - 14:30) and equilibration (EQ, 15:00 - 18:00) are highlighted. 16

Figure 2.1: (a) Scripps Institution of Oceanography (SIO) pier (La Jolla, California) and nearshore region at low tide. (b) Mean cross-shore bathymetric profile with mean tide level and approximate tidal extents. The radiometer is located at $x_R = -100$ m (orange marker), a location frequently within the surfzone. . 26

Figure 2.2: (a) Photo of the radiometer deployed over the surfzone. (b) Detail of the NR01 radiometer. (c) Boom mount schematic. 27

Figure 2.3: Hourly time-series of (a) water depth h_R at the radiometer location ($x_R = -100$ m), (b) pier-end significant wave height H_s, (c) wind speed $|u_w|$, (d) solar zenith angle θ_s, (e) observed downwelling Q_d (red) and upwelling Q_u (blue) short-wave solar radiation, and (f) observed albedo $\alpha_o = Q_u/Q_d$. . . 28

Figure 2.4: One-minute averaged observed albedo α_o versus $\cos(\theta_s)$ under (a) clear sky conditions ($T_r > 0.6$) and (b) diffuse light conditions ($T_r < 0.3$). Binned means (red diamonds) and $\pm$ one standard deviation (red vertical lines) of α_o are mostly elevated over the θ_s-only based parameterization α_{θ_s} (red dashed). 32

Figure 2.5: Hourly averaged observed albedo $\langle \alpha_o \rangle$ versus a) hourly-observed $H_s^{(p)}/h_R$ where $H_s^{(p)}$ is the significant wave height measured at the pier-end ($x = -270$ m) and h_R is the water depth at the radiometer, and b) hourly averaged wind speed. 33

Figure 2.6: Images of water below the radiometer (a) during a breaking event and (b) under calm non-breaking conditions when. Cropped and grayscale converted images of (c) a breaking wave and (d) non-breaking. Grayscale PDF values for (e) breaking conditions and (f) non-breaking conditions. 35
Figure 2.7: Gridded logarithmic density (gray scale) of image-derived albedo α_I versus observed albedo α_o. 36
Figure 2.8: Ten-minute time series of image-derived albedo α_I (red), observed albedo α_o (black) and parameterized open ocean albedo α_θ (dashed) beginning near noon on September 11, 2015. 37
Figure 2.9: (a) Modeled significant wave height H_s, (b) modeled wave-roller dissipation $\langle \varepsilon_r \rangle$, (c) inferred mean foam fraction $\langle \zeta_w \rangle$, (d) wave-model parameterized albedo $\langle \alpha_w \rangle$, and (e) bathymetry profile $h(x)$ versus cross-shore coordinate x for noon on February 8, 2015. 39
Figure 2.10: Hourly-averaged observed albedo $\langle \alpha_o \rangle$ versus the wave-model albedo parameterization $\overline{\langle \alpha_w \rangle}$ ($N = 1169$). The 1:1 line (dotted) is shown with binned means (red diamonds) and $\pm$ standard deviation (red lines). The best fit slope $m = 398$ and skill $r^2 = 0.68$ (binned-mean $r^2 = 0.94$). 40
Figure 2.11: Six day time series (October 25-30, 2014) of (a) solar zenith angle θ_s, (b) depth normalized significant wave height H_s/h at x_R with expected threshold of significant wave breaking (dotted) (c) observed albedo $\langle \alpha_o \rangle$ (black) and wave parameterized albedo $\langle \alpha_w \rangle$ (red). Nighttime ($\theta_s > 90$) is shaded. . . . 42

Figure 3.1: (a) The experiment site and surrounding nearshore waters. A moored temperature chain (green star, S18), bottom mounted thermistors (red dots) and the SIO pier (black line) are shown. (b) Cross-shore (x) instrument deployment locations (symbols). 51
Figure 3.2: Observed (a) SIO pier tidal elevation η, (b) wind speed u_w, (c) significant wave height H_s at the SIO pier-end (S8) and (d) air (black) and surface ocean in 18-m depth (red) temperature versus time. 55
Figure 3.3: Temperature versus vertical location below the mean tide level (MTL) z and time at cross-shore locations (a) $x = -100$ m, $h \approx 2$ m, denoted S2 (b) $x = -155$ m, $h \approx 4$ m, denoted S4 (c) $x = -219$ m, $h \approx 6$ m, denoted S6 (d) $x = -273$ m, $h \approx 8$ m, denoted S8 (e) $x = -657$ m $h \approx 18$ m, denoted S18. 56
Figure 3.4: Similar to Figure 3.3, but with the time axes of all plots zoomed to highlight 3.5 days of internal wave activity. The black bar on the abscissa indicates the timespan included in Figure 3.5. 58
Figure 3.5: Similar to Figure 3.4, but with the time axes of all plots zoomed to highlight 9 hours beginning on 7 October 2014 00:15 PDT. The black bar on the abscissa indicates the timespan included in Figure 3.6 60
Figure 3.6: Similar to Figure 3.5, but with the time axes of all plots zoomed to highlight 1.5 hours beginning on 7 October 2014 at 5:49 PDT. The 18.1°C, 19.6°C and 21.1°C isotherms are highlighted with a black curve in all panels. 61

Figure 3.7: **Top panels:** Mid-water column temperature at (a) S18 (green star in Figure 3.1) at $z = -9$ m and (b) S6 at $z = -4$ m, versus time. **Bottom panels:** Temperature spectra vs frequency at both S18 and S6 for (c) period I and (d) period II. 63
Figure 3.8: Five-hour time series of a NLIW runup event at S8 beginning at 8:13 am PDT on 26 October 2014: (a) S8 1 Hz temperature from near surface to near bed, (b) Cross-shore baroclinic current U' and (c) alongshore baroclinic current V' versus depth and time. 65
Figure 3.9: NLIW event example bottom temperature versus time beginning at 8:13 am PDT on 26 October 2014 for (a) the cross-shore locations and (b) the pier-end (S8) alongshore locations (red dots in Figure 3.1a), offset by 0.1°C in both (a) and (b) for visibility. 69
Figure 3.10: Number (N) and ΔT distribution (shading) of NLIW events observed between 9 and 30 October 2014 at cross-shore locations S8, S6 and S4 (highlighted in Figure 3.1b). Of the $N = 14$ events observed at S8, only six were observed at S4, and none with $\Delta T > 1.5$°C. 73
Figure 3.11: (a) NLIW event front speed $c_{\rm f}$ and incident angle θ at S8 for the 14 observed events between 9 and 30 October 2014. (b) NLIW two-layer gravity current front speed $c_{\rm gc}$ (3.10) versus event front speed $c_{\rm f}$ (3.4) for the 14 NLIW events observed at S8. 73
Figure 3.12: Bottom temperature versus time beginning at 7:37 on 12 October 2014 for (a) cross-shore locations and (b) alongshore locations (as in Figure 3.9) offset by 0.1°C for visibility. 74
Figure 3.13: NLIW event A-D front propagation distance Δx versus elapsed time Δt (colored dots) and quadratic fit (curves) as in (3.11). 76
Figure 3.14: NLIW event A-D (colored) (a) ΔT and (b) equivalent two layer interface amplitude $z_{\rm IW}$ vs upslope distance relative to S8 ($x - x_{\rm S8}$). Note, $z_{\rm IW}$ is only estimated at locations with at least four thermistors in the vertical. Events A and D are first estimated at $x - x_{\rm S8} = 27$ m as S8 was pre-stratified. 79
Figure 3.15: NLIW event A-D (colored) (a) normalized temperature anomaly $\Delta T/\Delta T_0$ and (b) normalized $z_{\rm IW}/z_{\rm IW_0}$ versus normalized upslope propagation distance $\Delta x/\Delta x_{\rm R}$. 81
Figure 3.16: (a) Best-fit gravity current speed $c_{\rm gc0}$ (3.10) versus NLIW front speed $c_{\rm f0}$ (3.11) at x_0 with rms error 0.013 m s^{-1} and best-fit slope 1.17. (b) Best-fit upslope gravity current deceleration $d_{\rm gc}$ (3.12) versus NLIW front deceleration $d_{\rm f}$ (3.11) with rms error 0.2×10^{-5} m s^{-2} and best-fit slope 0.84. 82
Figure 3.17: Predicted NLIW event A-D (colored) propagation distance $\Delta x_{\rm R}$ versus observed $\Delta x_{\rm R}$ using (a) best fit front velocity $c_{\rm f0}$ at x_0 and deceleration $d_{\rm f}$, and (b) two-layer gravity current velocity $c_{\rm gc}$ and deceleration $d_{\rm gc}$. The rms error is (a) 13 m and (b) 102 m. 82
Figure 3.18: NLIW event A-D (colored) normalized $z_{\rm IW}/h$ versus upslope propagation distance $\Delta x/\Delta x_{\rm R}$. 86

Figure 3.19: Five hour time series during event C of (a) event-induced change in horizontally-averaged potential energy $\Delta\langle \mathrm{PE} \rangle$ (3.17) (b) mid-water squared buoyancy frequency N^2 at S8, (c) squared mid-water shear S^2 at S8, and (d) the gradient Richardson number $\mathrm{Ri} = N^2/S^2$ at S8. 88

Figure 4.1: (a) Google earth image of the SIO pier experiment site. (b) Cross-section along the SIO pier depicting mean tide level (MTL) and mean bathymetry $z = -h(x)$ versus cross-shore coordinate x with wave gauge and radiometer locations indicated. 101

Figure 4.2: Example cross-shore (x) variation of hourly-averaged parameters (a) Bathymetry $h(x)$ and mean water level η, (b) significant wave height H_s and associated cross-shore wave energy flux F_{wave} (c) non-dimensionalized roller energy dissipation $\langle \widehat{\varepsilon_r} \rangle$ and foam fraction ζ and (d) albedo α_{sz}. 103

Figure 4.3: Schematic depicting the shortwave solar radiation (Q_{sw}, arrows) at different locations: the top of the atmosphere (dotted line) Q_{sw}^{top}, downwelling to the ocean surface Q_{sw}^{d}, upwelling (reflected) at the ocean surface Q_{sw}^{u}, and water-entering Q_{sw}. The solar zenith angle is θ_s. 105

Figure 4.4: Yearlong time series of (a) daily maximum solar radiation at the top of atmosphere and hourly averaged downwelling shortwave solar radiation to the ocean surface, (b) daily percent reduction of downwelling solar shortwave radiation (c) pier-end significant wave height H_s, and (d) surfzone width L_{sz}. 107

Figure 4.5: Hourly (a) pier-end wave energy flux F_{wave} (4.2) and (b) cross-shore averaged surfzone albedo α_{sz} (4.15) versus time of year. 110

Figure 4.6: Daily ensemble averaged albedo with no wave breaking α_θ (blue) and daily ensemble averaged cross-shore averaged surfzone albedo α_{sz} [Sinnett and Feddersen, 2016] (red) versus normalized time of day. Shading is $\pm$ one standard deviation from the mean. 111

Figure 4.7: Yearlong time series of daily (24-hour) averaged wave-heating Q_{wave} (4.6), and reduction in solar heating through the breaking wave albedo reduction in solar heating ΔQ_{sw}^{w} (4.16) as indicated in the legend. 112

Figure 4.8: Daily averaged change to solar heating ΔQ_{sw}^{w} versus the daily averaged wave heating Q_{wave} for each season. 113

Figure 4.9: Yearly time series of daily adiabatic surfzone temperature change ΔT due to the competing wave effects of wave heating Q_{wave} and albedo-induced reduction of solar heating ΔQ_{sw}^{w}. 115

Figure 4.10: Daily-averaged change in water-entering shortwave solar radiation ΔQ_{sw}^{w} between the surfzone and inner-shelf versus observed daily-averaged downwelling solar radiation Q_{sw}^{d}. 118

LIST OF TABLES

Table 1.1: Mean and standard deviation of cross-shore integrated surfzone heat flux terms (1.6) and (1.5): short-wave ($Q_{\mathrm{sw}}L_{\mathrm{sz}}$), long-wave ($Q_{\mathrm{lw}}L_{\mathrm{sz}}$), latent ($Q_{\mathrm{lat}}L_{\mathrm{sz}}$), sensible ($Q_{\mathrm{sen}}L_{\mathrm{sz}}$) heat fluxes, wave energy flux (F_{wave}), net surfzone heat flux F_{net}, and surfzone heat content time-derivative $\mathrm{d}H/\mathrm{d}t$. Note that $L_{\mathrm{sz}} = 132$ m. . 11

Table 3.1: Summary of example events A–D detailed in section 3.5. Left to right: Event designator, S8 H_{s}, $\mathrm{u_w}$, c_{f}, $|U_{\mathrm{b}}'|/c_{\mathrm{f}}$, θ, ΔT_0, z_{IW0}, d_{f} and standard error, and Δx_{R}. 72

ACKNOWLEDGEMENTS

The work described in this dissertation is the finished product of a truly enjoyable time working at Scripps and living in San Diego. Many thanks to my advisor Falk Feddersen, who has made this possible and helped guide my progress. I am a far better scientist having benefited from his guidance. Thanks also to the members of our lab: Kai Hally-Rosendahl, Derek Grimes, Michael Kovatch and post-docs Nirnimesh Kumar, Ata Suanda and Jacqueline McSweeney for all the helpful feedback, support and encouragement.

My committee members, Sarah Giddings, Peter Franks, Drew Lucas, and Geno Pawlak, have made many helpful suggestions and provided significant support in the development of this work. Thank you all for the careful guidance, and for the many discussions about both science and career. Scripps is an amazing place to learn, and many other talented Scripps scientists have made my time here truly enjoyable. Friends and colleagues here are too numerous to name individually, but each significantly contributed to my experience; thank you. I'd also like to sincerely thank Neal Pettigrew, Huijie Xue and many others at the University of Maine for guiding my first steps from engineering into oceanography.

My family and friends are a tremendous inspiration and provided vital support throughout. Marilyn, you are beside me at every major decision, temporary failure and eventual success. I love you. To my parents: thank you for fostering in me a love for science and the ocean. Dave: your encouragement has taken me from a reluctant dive partner to an oceanographer, thank you for helping me try new things.

This work was generously supported by grants from NSF (OCE-1558695), ONR (N00014-15-1-2117) NOAA (NA14OAR4170075/ECKMAN), California Sea Grant (R/HCME-26) and the Scripps GK12 program (DGE-0841407). Many professors, technicians and students helped collect data used for this dissertation, including Brian Woodward, Bill Boyd, Kent Smith, Rob Grenzeback, Christian McDonald, Rich Walsh, Stephanie Mumma, Greg Boyd, Lucian Parry, Bill O'Reilly, Corey Olfe, Dennis Darnell, Dan Cayan, Spencer Kawamoto, Jen MacKinnon, Amy

Waterhouse, Maddie Hamann, Julia Fiedler, Sean Crosby, Bonnie Ludka and many volunteer science divers who dove with me (sometimes on very short notice) to help maintain the pier-mounted sensors. Stephen Monismith and five anonymous reviewers provided feedback to significantly improve the chapters contained herein.

Chapter 1, in full, is a reprint of material as it appears in Sinnett, G., and F. Feddersen (2014), "The surf zone heat budget: The effect of wave heating," Geophys. Res. Lett., 41, 72177226. The dissertation author was the primary investigator and author of this paper.

Chapter 2, in full, is a reprint of material as it appears in Sinnett, G., and F. Feddersen (2016), "Observations and parameterizations of surfzone albedo", Methods Oceanogr., 17, 319334. The dissertation author was the primary investigator and author of this paper.

Chapter 3, in full, is a reprint of material as it appears in Sinnett, G., F. Feddersen, A. J. Lucas, G. Pawlak, and E. Terrill (2018), "Observations of nonlinear internal wave run-up to the surfzone", Journal of Physical Oceanography, 48(3), 531554. The dissertation author was the primary investigator and author of this paper.

Chapter 4, in part, is currently being prepared for submission for publication of the material. Sinnett, G., F. Feddersen. The dissertation author was the primary investigator and author of this paper.

VITA

2004	Bachelor of Science, Engineering Physics *cum laude*, University of Maine, Orono
2004-2010	Development Engineer, Fairchild Semiconductor, Portland, Maine
2010-2012	Research Assistant, University of Maine, Orono
2012	Master of Science, University of Maine, Orono
2012-2018	Research Assistant, Scripps Institution of Oceanography, University of California San Diego
2018	Doctor of Philosophy, Scripps Institution of Oceanography, University of California San Diego

PUBLICATIONS

Sinnett, G., and F. Feddersen (2014), "The surf zone heat budget: The effect of wave heating", *Geophys. Res. Lett*., 41, 72177226, doi:10.1002/2014GL061398.

Sinnett, G., and F. Feddersen (2016), "Observations and parameterizations of surfzone albedo", *Methods in Oceanography*., 17, 319-334, https://doi.org/10.1016/j.mio.2016.07.001

Sinnett, G., F. Feddersen, A.J. Lucas, G. Pawlak, and E. Terrill (2018) "Observations of Nonlinear Internal Wave Run-Up to the Surfzone", *J. Phys. Oceanogr*., 48, 531554, https://doi.org/10.1175/JPO-D-17-0210.1

ABSTRACT OF THE DISSERTATION

The Nearshore Heat Budget

by

Gregory Sinnett

Doctor of Philosophy in Oceanography

University of California San Diego, 2018

Professor Falk Feddersen, Chair

The nearshore region (surfzone and adjacent inner-shelf) are biologically and economically important and are affected by temperature changes from a variety of unique nearshore processes. Three such processes are explored here, along with their affect on the nearshore heat budget. Surfzone incident wave energy flux is dissipated by wave breaking which through viscosity generates heat (termed wave heating). A primative surfzone heat budget (including wave heating) closes on diurnal and longer time scales. Solar radiation was the dominant term, and wave heating the second most variable with mean heating contribution roughly one fourth that of solar radiation.

Breaking waves also generate foam, creating an albedo-induced surfzone solar heating reduction. Surfzone albedo observations were elevated above open-ocean observations, with

average albedo of 0.15 and one-minute averaged albedo as high as 0.45. New image- and wave-based surfzone albedo parameterizations were tested versus observations and have high skill ($r^2 = 0.90$ and $r^2 = 0.68$ respectively).

Nonlinear internal waves propagate across the inner-shelf, sometimes into the surfzone. The cross-shore evolution of nonlinear internal waves were tracked from 8-m depth to shore. Coherently propagating fronts had associated temperature drops up to 1.7°C with frontal velocities between 1.4 and 7.4 $\mathrm{cm\,s^{-1}}$. Front position was quadratic in time, decelerating in a manner consistent with gravity current scalings. Frontal temperature drop and equivalent two-layer height collapsed as a linearly decaying function of normalized cross-shore distance. During the rundown, near-surface cooling and near-bottom warming at 8-m depth coincide with a critical gradient Richardson number, indicating shear-driven mixing.

Together, waves act to both warm the surfzone (through wave heating) at a daily-averaged rate of $\approx 28\ \mathrm{W\,m^{-2}}$ and cool the surfzone (through albedo-induced reduction of solar heating) at a daily-averaged rate of $\approx 41\ \mathrm{W\,m^{-2}}$. Both wave-heating and albedo-induced reduction in solar heating varied predictably with commonly observed nearshore parameters.

Chapter 1

The surf zone heat budget: The effect of wave heating

1.1 Abstract

Surfzone incident wave energy flux is dissipated by wave-breaking which through viscosity generates heat. This effect is not present in shelf heat budgets, and has not previously been considered. Pier-based observations of water temperature in 1–4 m depth, meteorology and waves are used to test a surfzone heat budget, which closes on diurnal and longer time-scales. Wave energy flux is the second most variable term with mean contribution 1/4 of the mean short-wave radiation. The heat-budget residual has semi-diurnal and higher frequency variability and net cooling. Cross-shore advective heat flux driven by internal wave events, rip currents and undertow contribute to this residual variability and net cooling. In locations with large waves, steeper beaches or less solar radiation, the ratio of wave energy flux to short-wave radiation may be > 1.

1.2 Introduction

The nearshore (defined as ≤ 6 m water depth) region is ecologically and economically critical. Invertebrates, fish, and birds make their home in the nearshore. The region is a center of tourism and recreation, fueling economic activity. Nearshore waters are often impacted by poor water quality [Dorfman and Rosselot, 2009], creating health risks for bathers e.g., [Haile et al., 1999], thereby affecting coastal economies. The surfzone is the near-beach region where depth-limited wave-breaking occurs (with typical width $L_{\rm sz} = O(100)$ m, and depth typically twice the significant wave height). The region just seaward of the surfzone is denoted here as the inner-shelf. Thus, the nearshore includes both the surfzone and inner-shelf.

Water temperature variations play a critical ecological role in the nearshore, and are linked to variation in mussel and barnacle growth rates [Phillips, 2005], egg-mass production rates of the coastal crab *Cancer setosus* [Fischer and Thatje, 2008], as well as barnacle recruitment rates [Broitman et al., 2005]. Temperature is also a tracer for nutrient delivery to coastal waters e.g., [Omand et al., 2012]. Pathogen ecology in swimming waters is affected by temperature, in-

cluding *Staphylococcus* [Goodwin et al., 2012], *Enterroccus* [Halliday, 2012], and *Campylobacter* [Hokajarvi et al., 2013].

Previous nearshore temperature observations have typically been made using a vertical array to measure temporal variability and vertical structure e.g., [Winant, 1974, Pineda, 1991]. Observations from the Scripps Institution of Oceanography (SIO) pier (La Jolla) in the Southern California Bight (http://cordc.ucsd.edu/projects/Piers/SIO/TChain/) reveal substantial temperature variability in 6 m water depth at high frequency ($<$ 11 hr), semi-diurnal (11-14.5 hr), diurnal (18-33 hr) and subtidal ($>$ 33 hr) time-scales as defined by [Lerczak et al., 2003]. In water as shallow as 1.5 m, high-frequency nonlinear internal waves with 1 °C variation were observed on the summertime Dutch coast [van Haren et al., 2012]. However, the dominant processes governing surfzone temperature variability are not known, and a surfzone heat budget has never previously been studied.

Heat budgets on the Northern California outer shelf (60-130 m water depth) show cross-shelf advection exports heat off shelf year-round [Lentz, 1987, Dever and Lentz, 1994]. In shallower water (12-26 m) net cross-shore heat advection keeps shallow waters cooler than predicted by local surface heating [Fewings and Lentz, 2011]. This cross-shore heat advection is influenced at subtidal time scales by stratification, along-shelf winds [Austin, 1999], and cross-shore wave-driven mass transport [Fewings and Lentz, 2011]. In addition, significant shelf temperature variations can be driven at diurnal time-scales by sea-breeze driven upwelling e.g., [Woodson et al., 2007] or solar heating e.g., [Davis et al., 2011], and also driven at semi-diurnal and shorter time-scales by internal waves e.g., [Omand et al., 2011, Walter et al., 2012].

In contrast to the shelf, an additional process is *unique* to the surfzone heat budget. Incident wave energy flux F_{wave}, due to surfzone wave breaking, leads to turbulent dissipation e.g., [Feddersen, 2012a, Feddersen, 2012b], which by viscosity converts mechanical energy to heat. In addition, incident waves can also drive surfzone currents, which are largely frictionally balanced e.g., [Feddersen et al., 1998], also generating heat. Incident F_{wave} is not fully converted

into heat as there can be surfzone export of mechanical energy. However, as discussed in Section 5, this is much smaller than the incident F_{wave}.

Observations from a cross-shore thermistor array mounted on the SIO pier (Section 2) are used to test a simplified surfzone heat budget (Section 3). The previously unconsidered wave energy flux term is significant and the binned-mean heat budget closes to first order (Section 4), although significant semi-diurnal and higher frequency variability in heat content is not resolved. The implications of wave energy flux heating of the surfzone, and cross-shore advective heat flux are discussed in Section 5. Results are summarized in Section 6.

1.3 Experiment

A surfzone heat budget was tested with observations at the SIO pier for 47 days from June 6 – July 23, 2013. Six thermistors (Onset TidBit) were attached at $z = -0.9$ m below mean sea level to the north (shaded) portion of pier pilings at cross-shore (x) locations between $x = 49$ m and $x = 216$ m (where $x = 0$ m is at the mean low-tide shoreline) in mean water depths spanning $h = 1.5$ m to $h = 4$ m (Figure 2.1). The surfzone and inner shelf bathymetry profile (Figure 2.1) was measured on day 46 of the experiment by a jet ski bathymetry surveying system. Four specific thermistor locations are denoted, from onshore to offshore, as A, B, C, and D. An additional deeper thermistor was deployed at C, 1.6 m below the upper thermistor and was active for 20 days. Offshore surface water temperature was recorded at the Scripps Coastal Data Information Program (CDIP) mooring site 201 (location E) 1.2 km from shore in approximately 39 m water depth. Data was removed during extreme low tides (vertical extents > 0.69 m), when the thermistors might have been exposed to air ($\approx 10\%$ of all data).

Air temperature, humidity, winds, and tidal elevation were measured at the end of the SIO pier (near D). Incoming short-wave radiation also was measured on the SIO Pier with a LI-200SA Pyranometer sensor maintained by the SIO Climate Research Division. Hourly wave

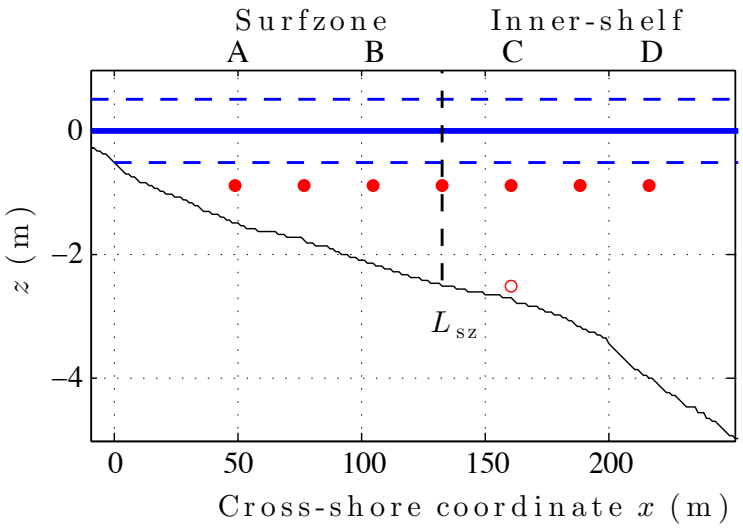

Figure 1.1: Cross-shore x distribution of thermistors mounted to the SIO pier (dots). A cross-shore bathymetry profile at the SIO pier is shown in black with mean sea-level at $z = 0$ m (blue) and $\pm$ tide level (blue dashed). Seven thermistors (red) were deployed from June 5th to July 23th 2013. Specific cross-shore sensor locations are denoted A ($x = 49$ m), B ($x = 105$ m), C ($x = 160$ m), and D ($x = 216$ m). An additional thermistor was temporarily deployed from June 5th to June 25th at location C (open dot) 1.6 m below the near-surface thermistor. The outer surfzone boundary L_{sz} is set at $x = 132$ m (vertical black dashed line).

statistics, including significant wave height H_s, were provided by a virtual buoy (monitored and predicted points "MOP") at the SIO pier, from the real-time CDIP spectral refraction wave model, initialized from offshore buoys [O'Reilly and Guza, 1991, O'Reilly, W.C. and Guza, R.T., 1998]. This wave model has been used in studies of beach erosion [Yates et al., 2009] and shoreline ground motions [Young et al., 2013] in the Southern California Bight. During times when the pier-mounted SIO wave gauge was operational (May and late July to August 2013), the model demonstrates very high skill.

1.4 Surfzone Heat Budget

The surfzone heat budget is written as a cross-shore and vertically integrated box model for heat content H, similar to a North Carolina inner-shelf heat budget in 13-26 m water depth [Austin, 1999]. With alongshore (y) uniform conditions, the surfzone heat content H ($\mathrm{J\,m^{-1}}$) in a region from the shoreline $x = 0$ to the fixed surfzone width $x = L_{\mathrm{sz}}$ is,

$$H = \rho c_p \int_0^{L_{\mathrm{sz}}} \int_{-h(x)}^{0} T(x,z)\, dz\, dx, \tag{1.1}$$

where ρ is the density and c_p is the specific heat capacity and h is the water depth. The upper-limit ($z = 0$ m) of the vertical integral is the mean sea surface. Heat content time-variation is driven by the total heat-fluxes F_{tot} into and out of the box, *i.e.*,

$$\frac{\mathrm{d}H}{\mathrm{d}t} = F_{\mathrm{tot}}. \tag{1.2}$$

The total surfzone heat flux F_{tot} is,

$$F_{\mathrm{tot}} = (Q_{\mathrm{sw}} + Q_{\mathrm{lw}} + Q_{\mathrm{lat}} + Q_{\mathrm{sen}})L_{\mathrm{sz}} + F_{\mathrm{wave}} + F_{\mathrm{adv}} \tag{1.3}$$

where the Q ($\mathrm{W\,m^{-2}}$) terms are surface vertical heat fluxes, consisting of the water-entering short-wave (Q_{sw}) radiation, net long-wave (Q_{lw}) radiation, and latent (Q_{lat}) and sensible (Q_{sen}) heat fluxes. As written in (1.3), the Q terms are assumed cross-shore uniform, but may differ between the surfzone, where waves are breaking, and farther offshore (but within the nearshore).

The F terms in (1.3) are cross-shore heat fluxes ($\mathrm{W\,m^{-1}}$) evaluated at the surfzone boundary $x = L_{\mathrm{sz}}$. The surfzone-specific cross-shore heat flux contribution from breaking surface gravity waves, F_{wave} ($\mathrm{W\,m^{-1}}$), as in (1.4) is considered here for the first time. For narrow-banded waves, the cross-shore wave energy flux at the surfzone boundary is

$$F_{\mathrm{wave}} = \frac{1}{16}\rho g H_{\mathrm{s}}^2 c_g \cos(\theta), \tag{1.4}$$

where g is gravity, c_g is the group velocity at the peak frequency, and θ is the peak direction. Surfzone cross-shore advective heat flux F_{adv}, due to processes in the surfzone (such as undertow and rip currents) or shelf (internal waves), were not estimated here, and are discussed in Section 1.6. Furthermore, the export of mechanical energy from the surfzone to inner-shelf is shown to be small (Section 1.6).

The resulting net surfzone heat flux, F_{net}, considered in this heat budget is,

$$F_{\mathrm{net}} = (Q_{\mathrm{sw}} + Q_{\mathrm{lw}} + Q_{\mathrm{lat}} + Q_{\mathrm{sen}})L_{\mathrm{sz}} + F_{\mathrm{wave}}, \tag{1.5}$$

which, as in (1.2), is balanced against $\mathrm{d}H/\mathrm{d}t$, i.e.,

$$\mathrm{d}H/\mathrm{d}t = F_{\mathrm{net}}. \tag{1.6}$$

This heat budget (1.6) assumes that the gradient of cross-shore integrated alongshore (y) advective heat flux (i.e., terms related to $V\mathrm{d}T/\mathrm{d}y$, where V is the alongshore current) is negligible. On beaches with alongshore uniform bathymetry and incident wave field, time-averaged (hourly)

alongshore mass, momentum, and turbulent TKE flux gradients are weak e.g., [Feddersen et al., 1998, Feddersen and Guza, 2003, Feddersen, 2012a]. Thus, alongshore heat flux gradients are expected to be weak as well.

The surfzone heat content H (1.1) was estimated with data from four surfzone thermistors and cross-shore integrating using the trapezoidal rule. Due to strong breaking-wave induced turbulence e.g., [Feddersen, 2012b], the surfzone is assumed to have vertically uniform temperature (i.e., well mixed), consistent with vertically-uniform surfzone dye [Hally-Rosendahl et al., 2014] and turbulent kinetic energy [Ruessink, 2010] observations. The outer limit of the surfzone was fixed at $L_{\mathrm{sz}} = 132$ m (between B and C, vertical dashed line in Figure 2.1) which contained the surfzone at all times. However, at high tides and with small waves, wave-breaking occurred farther onshore of $L_{\mathrm{sz}} = 132$ m. The constant vertical integral upper limit ($z = 0$ m) fixes the mass of the surfzone. Thus heat-content changes (and associated fluxes) due to tidal-induced surfzone mass changes are not included here. The change in surfzone heat content, $\mathrm{d}H/\mathrm{d}t$, was estimated with centered differences.

Short-wave radiation above the water surface (Q_{sw}^{+}) was measured with a pier-end radiometer 10 m above the water surface. Water entering short-wave radiation Q_{sw} is estimated as $Q_{\mathrm{sw}} = Q_{\mathrm{sw}}^{+}(1-\alpha)$, where α is a solar-zenith angle dependent open-ocean albedo ($\approx 6\%$) parameterization [Payne, 1972]. As the surfzone is generally turbid with large optical attenuation, all water-entering Q_{sw} is assumed absorbed in the water column. Since the albedo of wet sand is small ($\approx 6\%$) [Zhang et al., 2014], any Q_{sw} reaching the bed will be absorbed by a thin sand layer, which will rapidly equilibrate with the turbulent water of the surfzone. Total (outgoing and incoming) long-wave radiation Q_{lw} is estimated with a standard bulk parameterization method using cloud cover, vapor pressure, and air and water temperature [Josey et al., 1997]. Vapor pressure was calculated from sea surface temperature using the Antoine equation [Thomson, 1946]. Air-sea sensible (Q_{sen}) and latent (Q_{lat}) heat fluxes are estimated via the COARE 2.5 bulk parameterization [Fairall et al., 1996] using wind speed, air and water temperature and

humidity. All heat budget terms were low-pass filtered with a 2 hr cutoff. Through controlled thermistor tests, the 2-hr low-pass filtered $\mathrm{d}H/\mathrm{d}t$ instrument noise level is estimated using (1.1) to be $\approx 300\ \mathrm{W\,m^{-1}}$.

1.5 Results

Over the 47 day deployment, observed ocean temperature T spanned 14.5 °C to 23.4 °C (Figure 1.2a), with coherent variability at subtidal ($>$ 33 hrs) time-scales. Diurnal variability was stronger closer to shore (A & D) than 1.2 km offshore at E. Air temperature was typically colder than the ocean, fluctuating subtidally and diurnally. Significant cross-shore T variation was also observed. The temperature difference between surfzone location A and inner-shelf location D, ΔT_{AD} (separated by $\Delta x = 157$ m), varied significantly between -3 °C and 2 °C, generally at diurnal and shorter time-scales (not shown). The deployment spanned several spring-tide (amplitude 1.3 m) and neap-tide (amplitude 0.3 m) cycles (Figure 1.2b, black), with the majority contribution from M2 and K1. The mean significant wave height, H_s, was 0.7 m (Figure 1.2b, red) but fluctuated on subtidal time-scales with maximum and minimum of 1.6 m and 0.3 m, respectively.

The water-entering short wave radiative heat flux ($Q_\mathrm{sw}L_\mathrm{sz}$) warms the surfzone, varies diurnally from zero at night-time to peak daytime values $\approx 5\times10^4\ \mathrm{W\,m^{-1}}$, and is the largest surfzone heat budget term (blue curve in Figure 1.2c and Table 1.1). The net long-wave radiation ($Q_\mathrm{lw}L_\mathrm{sz}$) cools the surfzone and is largely steady at roughly half the time-averaged $Q_\mathrm{sw}L_\mathrm{sz}$ (magenta curve in Figure 1.2c and Table 1.1). The latent heat flux ($Q_\mathrm{lat}L_\mathrm{sz}$) and wave energy flux ($F_\mathrm{wave}$) have similar magnitude and variability (black and red curves, respectively in Figure 1.2c and Table 1.1), but cool and warm the surfzone, respectively. The wave energy flux term F_wave, is on average 1/4 of the short-wave radiative heating $Q_\mathrm{sw}L_\mathrm{sz}$, and is the 2nd most variable term (Table 1.1), indicating it is an import factor in the surfzone heat budget. Estimated sensible heat

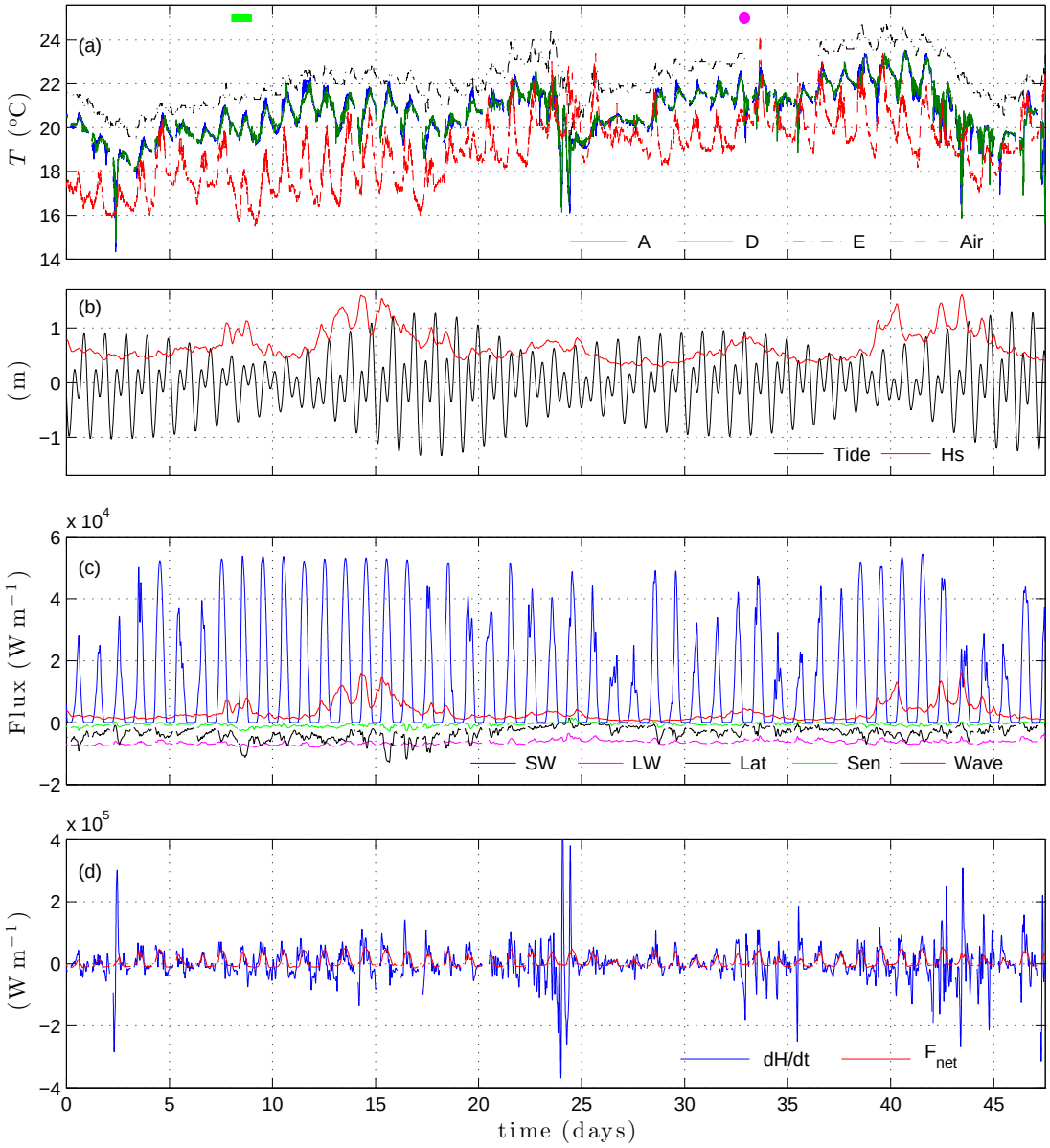

Figure 1.2: Time series of: (a) water temperature at locations A ($x = 49$ m), D ($x = 216$ m) and E (CDIP buoy, $x = 1200$ m), and air temperature at SIO Pier (see legend). Note temperature at E is offset by 1.5 °C for visibility. (b) Pier tidal elevation (black) and significant wave height H_s in 10 m depth (red). (c) Surfzone energy flux terms including water-entering short-wave ($Q_{sw}L_{sz}$) net long-wave ($Q_{lw}L_{sz}$) radiative fluxes, sensible ($Q_{sen}L_{sz}$) and latent $Q_{lat}L_{sz}$) air-sea fluxes, and wave energy flux F_{wave}. (d) Cross-shore integrated surfzone heat budget terms dH/dt and F_{net}. The magenta dot at day 32 in plot (a) indicates the time of a strong internal wave event observed at locations C, B and A highlighted in Figure 1.4. The green bar over days 8 and 9 in plot (a) corresponds to the time highlighted in Figure 1.5.

Table 1.1: Mean and standard deviation (std) of cross-shore integrated surfzone heat flux terms (1.6) and (1.5): short-wave ($Q_{sw}L_{sz}$), long-wave ($Q_{lw}L_{sz}$), latent ($Q_{lat}L_{sz}$), sensible ($Q_{sen}L_{sz}$) heat fluxes, wave energy flux (F_{wave}), net surfzone heat flux F_{net}, and surfzone heat content time-derivative dH/dt. Note that $L_{sz} = 132$ m.

($\times 10^4$ W m^{-1})	$Q_{sw}L_{sz}$	$Q_{lw}L_{sz}$	$Q_{lat}L_{sz}$	$Q_{sen}L_{sz}$	F_{wave}	F_{net}	dH/dt	F_{res}
Mean	1.40	-0.63	-0.33	-0.06	0.33	0.70	0.18	-0.52
Std	1.69	0.07	0.20	0.05	0.29	1.73	5.52	5.10

flux ($Q_{sen}L_{sz}$) is small compared to other heat budget terms.

The net surfzone heat flux F_{net} (1.5) and surfzone heat content time-derivative dH/dt are reasonably coherent at diurnal and longer time-scales (Figure 1.2d), but dH/dt has more variability than F_{net} (Table 1.1) at semi-diurnal and shorter time-scales. This results in an unbinned heat balance (1.6) with low best-fit skill (squared correlation $r^2 = 0.16$) and high heat-budget residual $F_{res} = dH/dt - F_{net}$ (Table 1.1). A binned-mean heat balance, representative of diurnal and longer time-scales, has a strong linear relationship between F_{net} and dH/dt with high best-fit skill ($r^2 = 0.89$), near-one slope ($\pm$ standard deviation) of $1.20(\pm 0.06)$, and an intercept of -6×10^3 W m^{-1} (Figure 1.3). The slope and intercept of the binned-mean and unbinned heat balance are similar. The binned-mean heat balance high skill and the near-one slope indicates that, at diurnal and longer time-scales, the heat budget closes to first order.

The wave energy flux F_{wave}, the 2nd most variable F_{net} term, plays a significant role in the surfzone heat budget. If F_{wave} is excluded from F_{net} (1.5), the binned-mean best-fit slope is farther from unity (1.33 ± 0.07) than if F_{wave} is included (1.20 ± 0.06). Thus, the wave energy flux helps balance the observed dH/dt variability, demonstrating its importance to the surfzone heat budget.

Over the 47-day experiment, the surfzone had net warming (positive $\langle dH/dt \rangle$ in Table 1.1 where $\langle\rangle$ represent a time-average), but warmed slower (by ≈ 5200 W m^{-1}) than expected from $\langle F_{net} \rangle$, consistent with the heat budget's negative intercept (Figure 1.3). The surfzone net heat-flux F_{net} variability is dominated (79% of variance) at diurnal (18-33 hr) and subtidal ($>$ 33 hr) time-scales. The heat budget residual F_{res} variability far exceeds the 300 W m^{-1} expected noise level

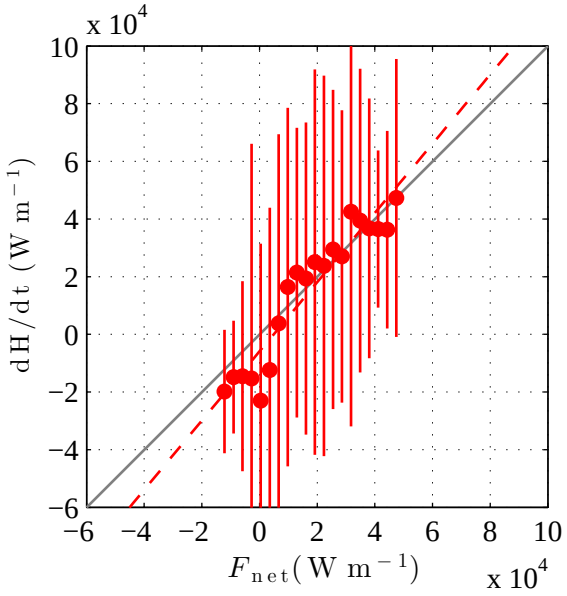

Figure 1.3: Surfzone heat budget (1.6): Binned-mean dH/dt versus $F_{\rm net}$ (solid red circles) and standard deviations (vertical red bars). The best-fit line (red dashed) has a slope of 1.20 and an intercept of -6×10^3 W m^{-1}, with best-fit skill of $r^2=0.89$.

(Table 1.1) and is dominated (80% of variance) at semi-diurnal (11-14.5 hr) and higher-frequency ($<$ 11 hr) time-scales. Thus, processes (such as cross-shore heat advection) driving heat-content net cooling and variability on semi-diurnal and shorter time-scales are missing from the estimated $F_{\rm net}$. This is discussed further in Section 1.6.

1.6 Discussion

At the La Jolla, CA experiment site, the ratio of time-averaged (over the deployment) wave energy flux $\langle F_{\rm wave}\rangle$ to time-averaged short wave radiation $\langle Q_{\rm sw}\rangle L_{\rm sz}$ was $\approx 1/4$, and the daily-averaged ratio $\langle F_{\rm wave}\rangle/(\langle Q_{\rm sw}\rangle L_{\rm sz})$ varied between 0.05 and 1.1. This indicates that wave energy flux is important to the surfzone heat budget. The summer (June–July) deployment with long days and high solar zenith angle resulted in large daily-averaged short wave radiation $\langle Q_{\rm sw}\rangle = 106$ W m^{-2}. At this site, summer waves are generally small compared to winter. During different seasons or at other locations (such as the Oregon coast where there are strong waves and

cloudy skies) the wave energy flux F_{wave} may be even more important in the surfzone heat budget. Assuming a planar beach slope β and normally incident shallow-water waves ($c_g = \sqrt{gh}$) that break in depth h_b having constant $\gamma_b = H_s/h_b$ e.g., [Thornton and Guza, 1983], $L_{\text{sz}} = h_b/\beta$ and the ratio $F_{\text{wave}}/(Q_{\text{sw}}L_{\text{sz}})$, using (1.4), becomes

$$\frac{F_{\text{wave}}}{Q_{\text{sw}}L_{\text{sz}}} = \frac{\rho\beta\gamma_b^2(gh_b)^{\frac{3}{2}}}{16Q_{\text{sw}}}. \tag{1.7}$$

The ratio (1.7) gives the importance of wave energy flux relative to short-wave radiative solar heating, and is proportional to beach slope β, γ_b^2, and $h_b^{3/2}$ (a function of H_s). For constant daily-averaged Q_{sw}, at steep beaches (where β is large and small surfzone width) or locations with large waves (where h_b is deeper), the importance of F_{wave} relative to $Q_{\text{sw}}L_{\text{sz}}$ in (1.3) increases. A Pacific Northwest winter case example with slope $\beta = 0.02$, $\gamma_b = 0.5$, and measured coastal Nov-Mar averaged short-wave radiation $\langle Q_{\text{sw}} \rangle = 52\ \text{W m}^{-2}$, and large waves typical of this location ($H_{\text{s}} = 3$ m and $h_b = 6$ m) gives a average ratio (1.7) of 2.7. Thus, wave heating can be more important than daily-averaged short-wave radiative heating.

The incident F_{wave} may not be fully converted to heat in the surfzone, resulting in surfzone export of mechanical energy. One pathway is by shoreline wave reflection on non-dissipative steep beaches. However, on dissipative beaches (such as this one), reflected wave energy flux was < 0.03 of the incident F_{net} e.g., [Elgar et al., 1994]. Rip currents or undertow could also export mechanical energy, which can be simply quantified as

$$h_b u^* \left(\frac{1}{2} \rho u^{*2} \right) \tag{1.8}$$

(units W m^{-1}) where u^* is an effective surfzone to inner-shelf exchange velocity that includes all potential exchange mechanisms. For a nearby beach with larger waves than typically observed here, $u^* \approx 10^{-2}\ \text{m s}^{-1}$ [Hally-Rosendahl et al., 2014]. With $h_b \approx 2$ m (Figure 2.1), the surfzone export of kinetic energy (1.8) is approximately $10^{-3}\ \text{W m}^{-1}$, 6 orders of magnitude less than the

mean F_{net} of 3300 W m^{-1} (see Table 1.1). If instead $u^* = 10^{-1}$ m s^{-1} (a very large value), the surfzone export of kinetic energy becomes ≈ 1 W m^{-1}, still $< 0.1\%$ of the mean incident wave energy flux. Thus, the great majority of F_{net} must be dissipated within the surfzone.

The heat budget residual (Figures 1.2d, 1.3, and Table 1.1) has large semi-diurnal and higher-frequency variability and a negative mean (residual cooling), analogous to the summertime shallow (12-m depth) shelf mean heat export by cross-shore advective processes [Fewings and Lentz, 2011]. Rip currents (e.g., seaward directed flow out of the surfzone, [Dalrymple et al., 2011]) can export heat from the surfzone [Hally-Rosendahl et al., 2014], as likely can the undertow. The rip current or undertow induced F_{adv} can have contributions at a range of time-scales from the mean, subtidal, tidal, and higher frequency. Internal waves can drive strong semi-diurnal and higher-frequency nearshore temperature variability e.g., [Winant, 1974, Pineda, 1991]. This suggests that cross-shore advective heat flux F_{adv} due to these processes is important to the surfzone heat budget. Although F_{adv} was not measured here, the contribution from internal waves and surfzone processes (rip currents or undertow) to the surfzone heat content variability is examined qualitatively with two case examples.

During the deployment, strong cold events were observed to propagate from the inner-shelf (5 m depth) into the surfzone. A four-hour highly nonlinear internal wave (or bore) event demonstrates the internal wave contribution to high-frequency surfzone heat content variations (Figure 1.4). Internal waves have been observed seaward of the surfzone in ≥ 6 m water depth e.g., [Winant, 1974, Pineda, 1991, Pineda, 1994, Omand et al., 2011], and video observations of internal wave surface signatures just seaward of the surfzone suggest cross-shore propagation [Suanda et al., 2014]. However, this is the first in situ observation of cross-shore internal bore propagation from ≈ 4 m depth through the surfzone.

During this event, $H_{\text{s}} \approx 0.82$ m and the ebbing spring tide varied ≈ 1 m. At $t = 1$ hr, T_C ($x = 160$ m) dropped 4 °C (from 21 °C) in 0.6 hr, subsequently rebounding to its initial level 0.5 hr later (red curve in Figure 1.4a). The cold event arrived at B (55 m farther onshore) 0.3 hr

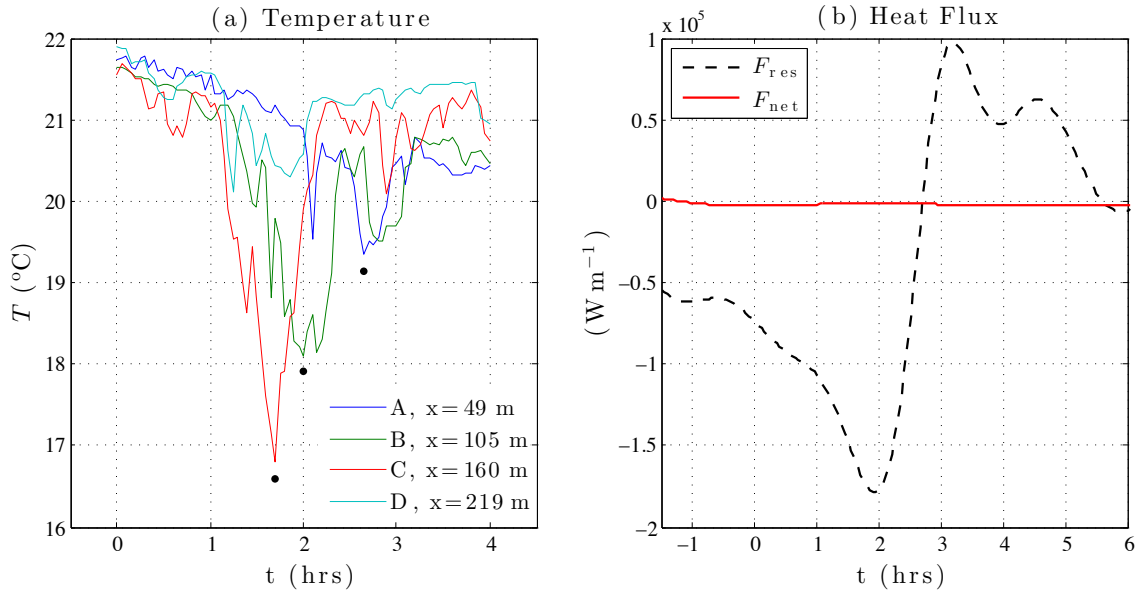

Figure 1.4: A 4-hour cold event on July 8th (indicated by a magenta dot on day 32 in Figure 1.2a): (a) SIO water temperature T at locations A, B, C, and D versus time t ($t = 0$ hr corresponds to 20:30 PDT). Black dots at (A,B,C) indicate the time of minimum temperature. (b) Net surfzone heat flux F_{net} (red) and the residual $F_{\text{res}} = dH/dt - F_{\text{net}}$ (black dashed) versus time t.

later, with an amplitude reduction to 3 °C (green curve in Figure 1.4a). The cold event minimum arrived at A 0.6 hr later with a reduced amplitude of ≈ 2 °C (blue curve in Figure 1.4a). Within the surfzone (B and A), the cold event duration is longer than at the deeper C, and temperature does not recover to its pre-event level, indicating net cooling from this event. At location D (59 m offshore of C), no significant cold event is observed (cyan curve in Figure 1.4), indicating that the cold internal wave event only surfaced farther onshore. The inferred cold event propagation speeds ($C = \Delta x/\Delta t$) $C_{BC} = 0.05$ m s^{-1} and $C_{AB} = 0.03$ m s^{-1} are approximately consistent with a reduced-gravity shallow water phase speed appropriate for a gravity current.

During this cold event, the surfzone net heat flux F_{net} is very small (red curve in Figure 1.4b), yet the residual $dH/dt - F_{\text{net}}$ (black dashed curve in Figure 1.4b) is large with maximum magnitude of 1.7×10^5 W m^{-1}. This indicates that the internal-wave driven advective heat flux into or out of the surfzone is at times large, in part explaining the large high frequency variability in dH/dt (Figure 1.2d). The area under the residual is negative (net cooling, black dashed curve

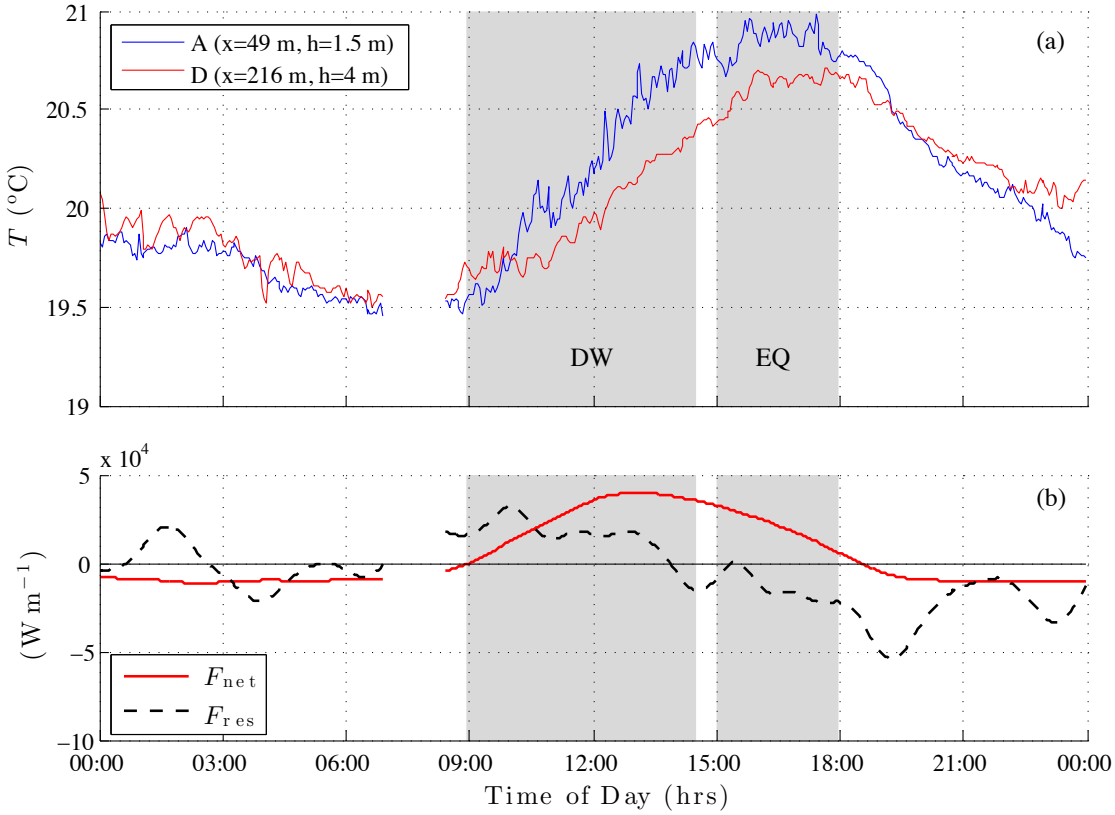

Figure 1.5: (a) Temperature at shallow surfzone location A (blue, $x = 49$ m, and $h = 1.5$ m) and the offshore, deeper location D (red, $x = 216$ m, $h = 4$ m) and (b) net surfzone heat flux F_{net} and the residual $F_{\text{res}} = \mathrm{d}H/\mathrm{d}t - F_{\text{net}}$ versus time of day. Temperature and solar radiation are ensemble averaged across 14 & 15 June (neap tide, days 8-9 highlighted by a green bar in Figure 1.2a). Periods of differential warming (DW, 9:00 - 14:30) and equilibration (EQ, 15:00 - 18:00) are highlighted.

Figure 1.4b) indicating that significant internal wave or surfzone driven mixing occurred.

Surfzone to inner-shelf heat exchange driven by surfzone processes is highlighted from a two-day (June 14-15, days 9-10) ensemble-averaged neap-tide case. Between 09:00-14:30, the surfzone (A) and inner-shelf (D) warmed (Figure 1.5a) consistent with strong positive F_{net} (Figure 1.5b) dominated by solar heating. However, the surfzone (A) warmed more rapidly than the inner-shelf D (denoted differential warming, DW in Figure 1.5a), likely due to shallower surfzone depths, resulting in $\Delta T_{AD} \approx 0.4$ °C after about 4 hours. Subsequently, surfzone temperature equilibrated, while nearshore temperature continued to rise (14:30-18:00, EQ in Figure 1.5a).

Both regions cool after 18:00. The surfzone temperature equilibration occurs even though the net heat flux F_{net} is positive (red curve in Figure 1.5b). Throughout EQ (14:30-18:00), the heat budget residual is negative (black dashed curve in Figure 1.5b), implying net surfzone cooling. The residual cooling time-scale is much longer than that of the onshore propagating cold event (Figure 1.4). Furthermore, no large rapid temperature fluctuations (as in Figure 1.4) nor any sense of propagation were observed at the thermistors. It is unlikely that a cold bore event was present below the surfzone thermistors (0.5–1.4 m above the bed, Figure 2.1), but not detected. Thus, the residual surfzone cooling during EQ is not due to internal waves. During EQ, the net residual cooling ($\approx 2.5 \times 10^4$ W m^{-1}) is also similar to the 2×10^4 W m^{-1} transient rip-current induced surfzone- to inner-shelf heat flux inferred by [Hally-Rosendahl et al., 2014]. Thus, this example of residual surfzone cooling is likely also due to surfzone to inner-shelf exchange induced by surfzone processes (undertow or rip currents). Larger waves drive larger rip currents e.g., [Dalrymple et al., 2011]. Thus, feedback between wave-energy flux and advective rip currents may also exist, such that as larger waves provide heat to the surfzone, some of that heat is advected offshore in more intense rip currents.

In addition to the large semi-diurnal and high-frequency time-scale heat budget residual, the binned-mean $\mathrm{d}H/\mathrm{d}t$ variability is 20% larger than the binned-mean F_{net} variability (best-fit slope is 1.2). Many factors may contribute to this, including estimating heat content (1.1) with only four thermistors, neglecting bathymetric $h(x)$ evolution, or assuming no stratification. In addition, the tidal sea-surface variation, inducing surfzone mass and thereby heat-content variations, is neglected. The vertical motion of the tides would lift and lower any surfzone stratification past the thermistors aliasing the $\mathrm{d}H/\mathrm{d}t$ estimate. At the seaward of the surfzone location C (Figure 2.1), a second thermistor was deployed for the first 20 days 1.6 m below the upper thermistor. During this time, the root-mean square stratification was 0.06 °C m^{-1}. Using the observed tidal amplitudes, this results in a tidally-induced apparent heat content variation of 2×10^3 W m^{-1}, small relative to F_{res} (Table 1.1). However, within the surfzone, strong breaking-wave induced mixing is

expected to result in weaker stratification as with other tracers e.g., [Hally-Rosendahl et al., 2014, Ruessink, 2010]. The near closure of the binned-mean heat budget justifies the neglect of the alongshore heat-flux gradients. Wind-generated spray in the open ocean has been shown to strongly affect latent (Q_{lat}) and sensible (Q_{sen}) heat fluxes [Andreas et al., 2008]. The COARE 2.5 parameterization for Q_{lat} and Q_{sen} used here do not include depth-limited breaking spray effects. Surfzone depth-limited wave breaking generates spray at least an order of magnitude larger than just offshore [van Eijk et al., 2011a]. Thus, surfzone latent and sensible heat fluxes may be under-represented, which could result in the best-fit slope above one and net cooling. The heat flux between sediment and the surfzone as on tidal flats e.g., [Rinehimer and Thomson, 2014, Kim et al., 2010] is neglected in (1.3) as here the beach slope and tidal amplitudes are $25\times$ larger and $3\times$ smaller, respectively, than on these tidal flats.

1.7 Summary

An experiment was conducted at the Scripps Institution of Oceanography (SIO) pier from June 6–July 23, 2013 to determine the importance of the onshore wave energy flux F_{wave} to the surfzone heat budget, which up to now had not been considered. Pier deployed thermistors measured surfzone and inner-shelf water temperature, with concurrent pier-based meteorological measurements and model wave energy flux estimates. The surfzone heat budget balances the time variation of vertical and cross-shore (over the surfzone width L_{sz}) integrated heat content $\mathrm{d}H/\mathrm{d}t$ with surfzone water-entering short-wave and net long-wave radiation, latent and sensible heat fluxes ($Q_{\mathrm{sw}}L_{\mathrm{sz}}$, $Q_{\mathrm{lw}}L_{\mathrm{sz}}$, $Q_{\mathrm{lat}}L_{\mathrm{sz}}$ and $Q_{\mathrm{sen}}L_{\mathrm{sz}}$ respectively) and the cross-shore wave energy flux F_{wave}. Short-wave radiation was the largest term in the surfzone heat budget. Time-averaged long-wave radiation, latent and sensible heat flux cooled the surfzone. The wave energy flux F_{wave} heated the surfzone, was on average $\approx 1/4$ of the daily averaged short-wave radiative heating, and was the second most variable term in the heat budget. The binned-mean heat budget,

representative of diurnal and longer time-scales, had high skill ($r^2 = 0.89$) and a slope near one, indicating the surfzone heat budget closed to first order.

The heat balance had unexplained residual variability at semi-diurnal and high frequency time-scales, and residual net cooling (≈ 5200 W m^{-1}). Cross-shore (surfzone to inner-shelf) advective heat fluxes due to nonlinear internal waves (causing 3°C surfzone temperature variation in 0.6 hours) and surfzone processes such as rip currents and undertow, (at times exporting $\approx 2.5 \times 10^4$ W m^{-1}) contributed to the high-frequency and net heat budget residual.

Excluding the wave energy flux F_{wave} from the binned-mean heat budget results in a best-fit slope farther from one, further demonstrating the importance of breaking-wave induced heating to the surfzone heat budget. A scaling for the ratio of F_{wave} to short-wave surfzone heat flux ($Q_{\text{sw}}L_{\text{sz}}$) shows that at locations where there are large waves, a large beach slope, or less solar insolation, the ratio may be > 1.

1.8 Acknowledgments

Support was provided by the National Science Foundation (NSF) and the Scripps GK12 program. Field data was collected with help from Kent Smith, Rob Grenzeback, Brian Woodward, Dennis Darnell and Kai Hally-Rosendahl. Dan Cayan of the SIO Climate Research Division and Doug Alden and Spencer of the SIO Hydraulics Laboratory provided the short wave radiative data which is available at

`http://meteora.ucsd.edu/weather/observations/sio_other/sites/stn_21.html`

Pier end meteorological data was provided by the SIO Climate Research Division. The SIO Coastal Data Information Program (CDIP) provided wave measurements, and William O'Reilly and Corey Olfe provided wave model information for the SIO pier. Comments from two anonymous reviewers significantly improved this manuscript. Thank you.

Chapter 1, in full, is a reprint of material as it appears in Sinnett, G., and F. Feddersen

(2014), “The surf zone heat budget: The eect of wave heating”, Geophys. Res. Lett., 41, 72177226. The dissertation author was the primary investigator and author of this paper.

Chapter 2

Observations and parameterizations of surfzone albedo

2.1 Abstract

Incident shortwave solar radiation entering the ocean depends on albedo α and plays an important role in the temperature variability and pathogen mortality of the nearshore region. As foam has an elevated albedo, open-ocean albedo parameterizations include whitecapping effects through a wind-based foam fraction. However, surfzone depth-limited wave breaking does not require wind. Surfzone albedo observations are very rare, the variability of surfzone albedo is not known, and parameterizations are not available. New, year-long upwelling and downwelling shortwave radiation observations were made from the Scripps Institution of Oceanography pier spanning the surfzone and inner-shelf. Surfzone albedo was elevated due to foam with mean observed albedo of $\alpha = 0.15$ and one-minute average albedo as high as $\alpha = 0.45$, far exceeding expected albedo (0.06) from standard parameterizations. Using a pier-mounted GoPro camera, an image-based albedo parameterization is developed that estimates the fractional foam area to derive albedo. This parameterization has high skill ($r^2 = 0.90$) on time scales as short as a wave period (9 s). A second wave-model based parameterization for (hourly) averaged albedo is developed relating the non-dimensional roller energy dissipation to the mean foam fraction and thus albedo. The parameterization has good skill ($r^2 = 0.68$) and resolves cross-shore albedo variations. These new parameterizations can be used where imagery is available or wave models are applicable, and can be used to constrain local heat budgets and pathogen mortality.

2.2 Introduction

The nearshore region (≤ 7 m water depth) is critical both economically and ecologically. The region is a center for tourism, recreation, and commercial use, and is also home to a wide variety of fish, birds, plants and invertebrates. Water temperature is an important ecological aspect, affecting growth rates, recruitment rates, egg-mass production, pathogen ecology and many other factors e.g., [Phillips, 2005, Fischer and Thatje, 2008, Broitman et al., 2005, Goodwin

et al., 2012, Halliday, 2012]. In this sensitive region, incident shortwave solar radiation entering the ocean (Q_{sw}) plays an important role in both the temperature variability [Sinnett and Feddersen, 2014] and pathogen mortality through UV-B photobiological damage e.g., [Sinton et al., 1994, Sinton et al., 2002].

Shortwave solar radiation entering the ocean is defined as

$$Q_{\mathrm{sw}} = Q_{\mathrm{d}} - Q_{\mathrm{u}}, \tag{2.1}$$

where Q_{d} is the total downwelling (downward) component of solar shortwave radiation, and Q_{u} is the upwelling (upward) component of shortwave radiation reflected from the ocean surface. The albedo α (surface reflection coefficient) is defined as

$$\alpha = \frac{Q_{\mathrm{u}}}{Q_{\mathrm{d}}}, \tag{2.2}$$

making

$$Q_{\mathrm{sw}} = (1-\alpha)Q_{\mathrm{d}}. \tag{2.3}$$

Under direct sun, open ocean albedo α depends on the solar zenith angle θ_{s} (the angle of sun declination from vertical) and has a daily average of $\alpha \approx 0.06$ [Payne, 1972, Briegleb et al., 1986, Taylor et al., 1996]. Under cloudy (diffusely lit) skies, open ocean albedo is near 0.06 and is independent of θ_{s} [Payne, 1972]. However, wind generates ocean whitecaps (foam) e.g., [Monahan, 1971, Monahan and Muircheartaigh, 1980] associated with elevated albedo. Wind also enhances the sea-surface slope variability e.g., [Ross and Dion, 2007], which affects albedo at large solar zenith angles e.g., [Saunders, 1967]. Laboratory measurements indicate that pure foam has albedo $\alpha = 0.55$ [Whitlock et al., 1982]. For a fractional surface coverage of foam ζ, the combined effects of foam and open water on albedo are often e.g., [Koepke, 1984, Frouin

et al., 1996, Jin et al., 2011] represented as

$$\alpha = \zeta\alpha_f + (1-\zeta)\alpha_\theta, \tag{2.4}$$

where α_f is the foam albedo, and α_θ is the parameterized solar zenith angle dependent open ocean albedo e.g., [Taylor et al., 1996]. The foam fraction ζ from open ocean whitecapping has been parameterized using a surface wind speed $|u_w|$ dependence e.g., [Hansen et al., 1983, Jin et al., 2004, Jin et al., 2011], but has a negligible effect on albedo (less than 0.002) for winds $|u_w| < 12\ \mathrm{m\,s^{-1}}$ [Payne, 1972, Moore et al., 2000, Frouin et al., 2001].

In the surfzone, foam is generated by depth-limited wave breaking regardless of wind, potentially elevating surfzone α and reducing Q_{sw}. Nearshore temperature evolution e.g., [Sinnett and Feddersen, 2014, Hally-Rosendahl et al., 2014] depends strongly on Q_{sw} in the surfzone and inner-shelf, the region just seaward of the surfzone. Elevated surfzone albedo may also help explain reduced surfzone pathogen mortality relative to the inner-shelf e.g., [Rippy et al., 013a, Rippy et al., 013b] making the surfzone albedo an important factor controlling the ecology of the region. Limited (21 min) surfzone albedo observations at 440–650 nm wavelengths reported elevated albedo up to 0.4–0.6, compared to 0.06 observed in the inner-shelf [Frouin et al., 1996], potentially influencing the surfzone heat budget [Sinnett and Feddersen, 2014]. However, no other surfzone albedo observations have been published (to our knowledge) and depth-limited wave-breaking albedo parameterizations do not exist. Thus, the magnitude and variability of surfzone albedo is not known, nor are its impacts on nearshore temperature and pathogen mortality. Making surfzone albedo observations is difficult, thus surfzone albedo parameterizations are needed.

Results from a year-long experiment at the Scripps Institution of Oceanography (SIO) pier measuring nearshore albedo under a wide variety of conditions are presented here, together with tests of two surfzone albedo parameterizations. As surfzone foam is visible in both time-elapsed

e.g., [Lippmann and Holman, 1990, Holland et al., 1997, Almar et al., 2010] and snapshot e.g., [Stockdon and Holman, 2000, Chickadel et al., 2003] optical images, the first parameterization uses optical images to estimate foam fraction and albedo. The second parameterization uses a wave and roller transformation model to estimate foam fraction and albedo. The experiment methods and observations are described in section 2.3. Results and the two parameterizations are presented in section 4.4, discussed in section 4.5, and summarized in section 2.6.

2.3 Methods and Observations

2.3.1 Experiment Description

Shortwave solar radiation, wave statistics, winds, and water depth were measured between October 25th, 2014 and October 25th, 2015 at the SIO pier (Figure 2.1a), La Jolla, California (lat 32.867, lon -117.257). Cross-shore (x) bathymetry profiles were made at 0.5 to 1 month intervals (see dots in Figure 2.3a) between $x = 0$ m (the cross-shore location of the shoreline extent at mean tide at the start of the experiment) and the pier end at $x = -270$ m. NOAA tide gauge station 9410230 at the SIO pier end (in ≈ 7 m water depth) measured the water level at 6 minute intervals. A representative cross-sectional view (Figure 2.1b) shows the mean bathymetric profile, the Mean Tide Level (MTL) reference height ($h = 0$), and tidal standard deviation (≈ 0.5 m).

Downwelling, Q_d and upwelling, Q_u shortwave solar radiation was measured by a Campbell Scientific NR01 research grade four-way radiometer (Figure 2.2b) having two shortwave radiation sensors (wavelengths from 305 nm to 2,800 nm) with 2.9 s response time and cosine angle spatial response over a 180° field of view. The sensor noise level is $< 1.5\%$ of the signal, instrument drift is expected to be $< 1\%$ per year, and instrument tilt errors are expected to be $< 2\%$. Both radiometer sensors were calibrated within one year of their deployment according to ISO 9847.

The NR01 radiometer was attached to the end of a custom designed boom arm (Figure

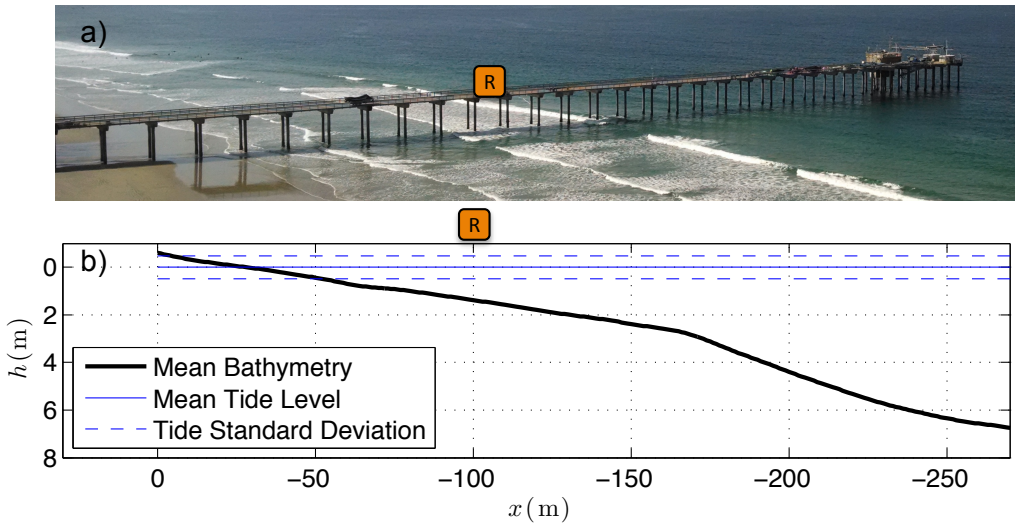

Figure 2.1: (a) Photo of the Scripps Institution of Oceanography (SIO) pier (La Jolla, California) and nearshore region at low tide. (b) Mean cross-shore bathymetric profile with mean tide level and approximate tidal extents. The radiometer is located at $x_\mathrm{R} = -100$ m (indicated with an orange marker), a location frequently within the surfzone.

2.2b) and fitted to the south side of the SIO pier at $x_\mathrm{R} = -100$ m. The cross-shore deployment location was chosen so that the radiometer would observe the surfzone roughly two-thirds of the time depending on the tidal depth and wave height. The radiometer was mounted 6.5 m above MTL to avoid significant spray from breaking waves, while assuring that more than 90% of the upwelling signal was confined to a 14 m radius watch circle beneath the instrument. The mounting boom was hinged at the pier end and mid-boom arm (Figure 2.2c arrows) allowing it to swing parallel and pivot up to the pier deck for cleaning at roughly 5 day intervals.

Generally, the radiometer sampled Q_d and Q_u continuously at 1Hz, storing the 1 min mean and standard deviation. On 9 days, a GoPro camera with a 72° vertical and 94° horizontal field of view was mounted on the pier deck approximately 2.5 m above the radiometer looking down at the water at $\approx 45°$ from horizontal. The camera captured images of the surfzone conditions at two second intervals with a 1/4000 second shutter speed, f/2.8 aperture value and ISO 100 speed rating. During this time the radiometer stored 1 Hz samples directly, allowing image and albedo comparison.

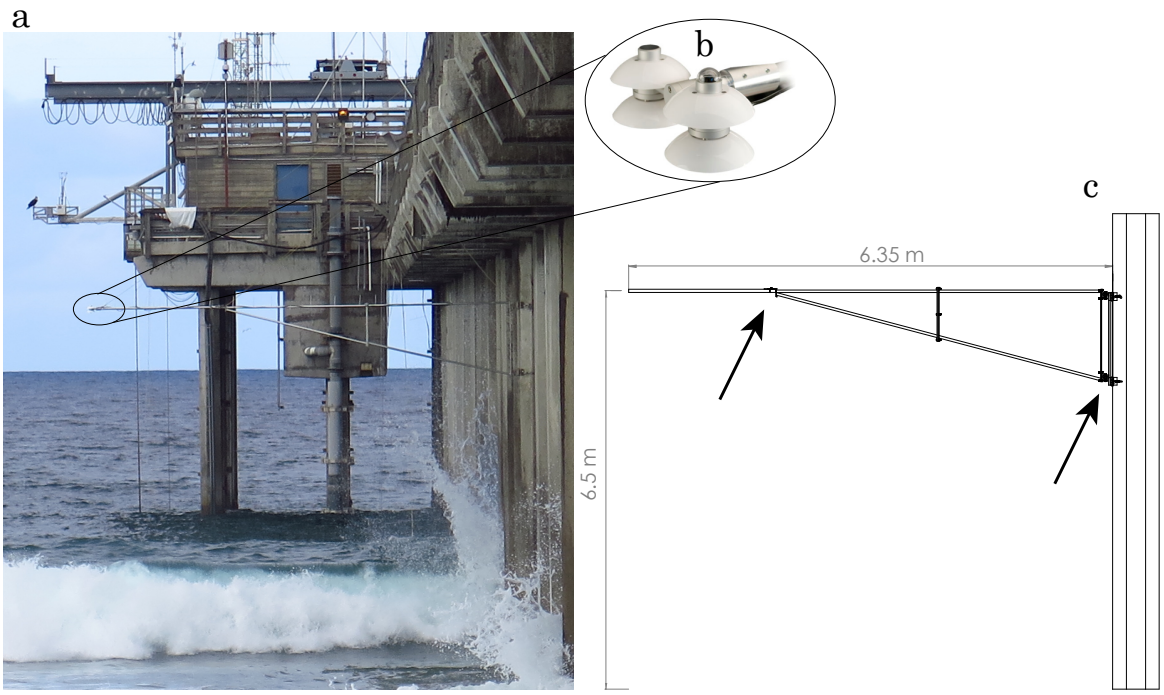

Figure 2.2: (a) Photo of the Campbell Scientific NR01 radiometer deployed over the surfzone, mounted on the south side of the SIO pier. (b) A close-up of the NR01 radiometer, consisting of upwelling and downwelling shortwave radiation sensors. (c) A schematic of the boom mount allowing radiometer deployment 6.5 m above MTL at a distance 6.35 m from the pier pilings. Hinges (arrows) allow the boom to pivot laterally and swing vertically for regular radiometer cleaning.

At pier-end, hourly significant wave height $H_s^{(p)}$ and peak period T_p were estimated by the Coastal Data Information Program wave gauge. During times when the wave gauge was offline (July 29 to August 20, 2015) a realtime spectral refraction wave model initialized from offshore buoys [O'Reilly and Guza, 1991, O'Reilly, W.C. and Guza, R.T., 1998] with very high skill was used. Winds were observed by the NOAA station at the pier end 18 m above MTL and reported as six-minute averaged values. The experiment site latitude and local time was used to calculate solar zenith angle θ_s based on [Reda and Andreas, 2008].

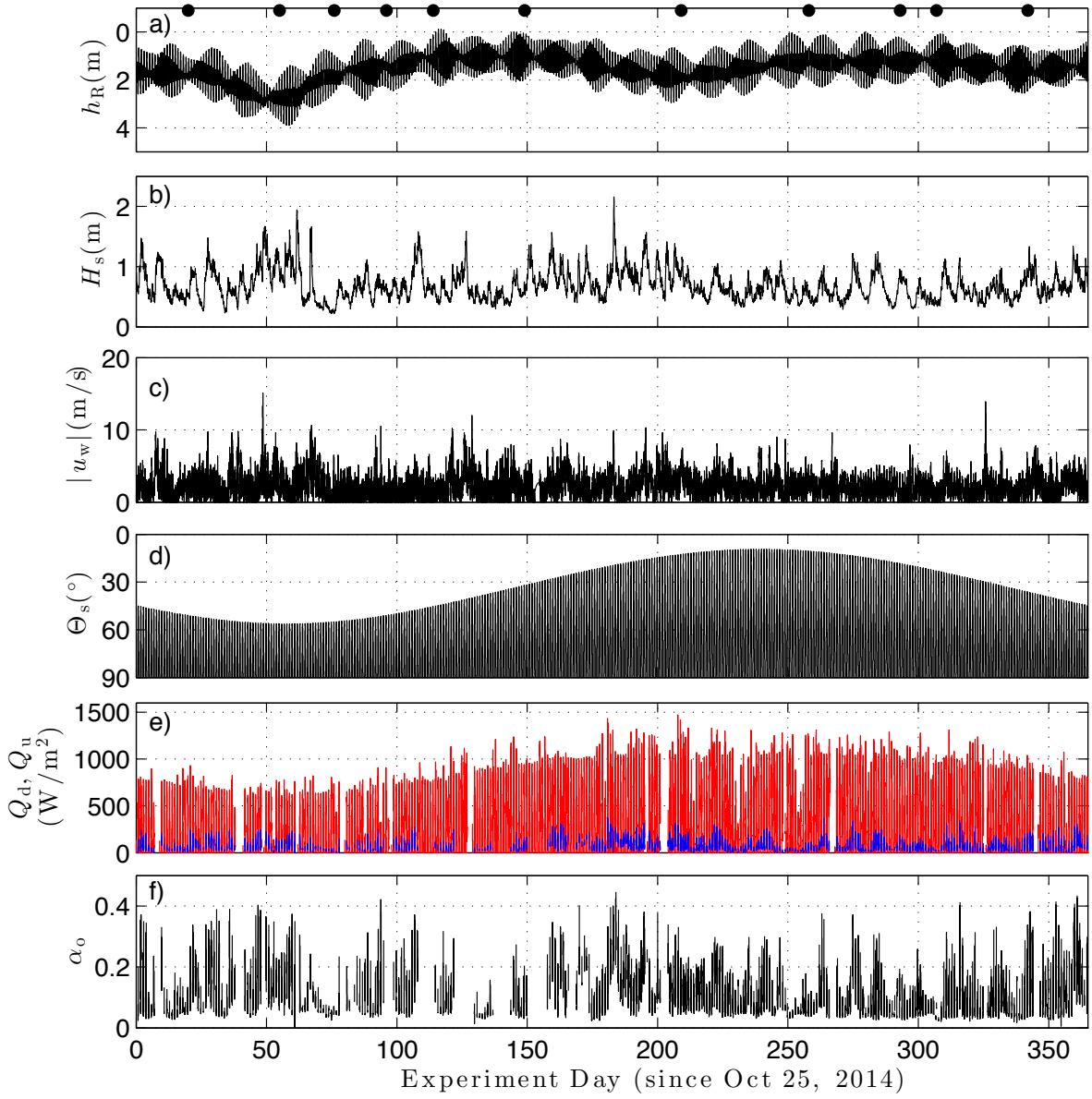

Figure 2.3: Hourly time-series over the year-long experimental period of (a) water depth h_R at the radiometer cross-shore location ($x_R = -100$ m), (b) pier-end significant wave height H_s, (c) wind speed $|u_w|$, (d) solar zenith angle θ_s, (e) observed downwelling Q_d (red) and upwelling Q_u (blue) short-wave solar radiation, and (f) observed albedo $\alpha_o = Q_u/Q_d$. Times when Q_d or Q_u were corrupted are removed in (e) and (f).

2.3.2 Observations

At x_R, the water depth h_R varied due to tidal changes in sea surface elevation and on longer time scales due to bathymetry changes (Figure 2.3a). Beach profile evolution followed a wintertime (defined here as day 26 on November 20, 2014 to day 126 on February 28, 2015) erosion and summertime (day 212 on May 25, 2015 to day 312 on September 2, 2015) accretion pattern, characteristic of southern California beaches e.g., [Ludka et al., 2015].

Pier-end significant wave height $H_s^{(p)}$ varied between 0.22 m and 2.16 m and peak period T_p between 3 s and 18 s (not shown) with increased wave activity occurring every few days, modulated seasonally with typically stronger wintertime and weaker summertime wave events (Figure 2.3b). Winds were typically calm, with average wind speed $|u_w|$ of 2.25 $\mathrm{m\,s^{-1}}$ having diurnal variability and occasional peaks above 10 $\mathrm{m\,s^{-1}}$, particularly in winter (Figure 2.3c). Solar zenith angle fluctuated diurnally with daily minimum θ_s varying on an annual time-scale between between 56.31° and 9.43° near the winter and summer solstice respectively (Figure 2.3d).

Foam-free albedo depends on θ_s in direct light (clear sky) but not in diffuse light (cloudy skies) [Payne, 1972]. Lighting conditions are characterized with the atmospheric transmittance T_r defined as the ratio of the observed downwelling radiation Q_d to the theoretical maximum Q_d,

$$T_r = \frac{Q_d}{S\cos(\theta_s)\gamma^{-2}}, \tag{2.5}$$

where S is the solar constant and γ is the ratio of the actual to mean earth-sun separation distance. Direct light conditions are defined when $T_r > 0.6$, and diffuse light conditions are defined when $T_r < 0.3$. The observations were made in 58% clear sky, 16% cloudy sky and 26% mixed sky ($0.3 < T_r < 0.6$) conditions.

Both Q_d and Q_u observations were removed during rain or heavy fog events when the radiometer was affected by moisture. In addition, Q_d and Q_u observations were removed when

$\theta_s > 60^\circ$ to avoid nighttime and times when the sun was behind a coastal bluff or very near the horizon. The radiometer was too close to the cross-shore location of exposed sand when, at x_R, the depth $h_R < 1.3$ m (approximately 38% of the time). These observations were also removed. The boom arm extended 6.35 m to the south of the pier to avoid pier shadow under clear skies, when the vast majority of light arrives from the southern sky. However, when the solar azimuth angle $\phi < 109^\circ$ ($< 0.1\%$ of the time), pier shadows were cast under the radiometer and these observations were removed. In total, $\approx$ 50% of daytime data was retained. For pure diffuse light conditions, the true Q_u is slightly underestimated primarily due to pier deck shadow reducing the available downwelling light and also due to pier pilings directly blocking a fraction of the upwelling light from the north. This effect is corrected following [Payne, 1972] so that the upwelling shortwave radiation is

$$Q_u = Q_{mu}[1 + 0.15(1 - T_r)], \tag{2.6}$$

where Q_{mu} is the measured upwelling shortwave radiation, T_r is the atmospheric transmittance, and pier geometry sets the coefficient (0.15). This correction has no effect on the results.

Downwelling shortwave radiation Q_d had a predominantly diurnal pattern with seasonal long-term variability and short (< 6 h) time-scale variability due to clouds (red in Figure 2.3e). Clear-sky daily maximum Q_d varied between 610 $\mathrm{W\,m^{-2}}$ in wintertime to 1064 $\mathrm{W\,m^{-2}}$ in the summer. Clouds typically reduced Q_d, but also increased Q_d for short periods (seconds to minutes) due to magnification caused by the "edge-of-cloud" effect e.g., [Davies, 1978, Coakley and Davies, 1986]. Reflected shortwave upwelling radiation Q_u (blue in Figure 2.3e) also varied on diurnal time scales, but contained variability on shorter time scales as well. A time series of over 70,000 one-minute averaged observed albedo observations α_o was generated from the the retained Q_d and Q_u with (2.2). Observed albedo α_o varied from 0.04 to 0.45 on a range of timescales from minutes to many days (Figure 2.3f).

2.4 Results

2.4.1 Albedo dependence on θ_s and waves

Here, the one-minute averaged observed albedo α_o is directly compared to solar zenith angle (θ_s) dependent parameterizations that assume no foam e.g., [Taylor et al., 1996]. Observed one-minute averaged albedo α_o are significantly elevated from a solar zenith angle dependent parameterization α_θ (compare dots to red dashed in Figure 2.4) for both clear and diffuse light conditions. For $\cos|\theta_s| > 0.5$, α_o varied from near 0.04, typical of α_θ, to 0.45, far exceeding α_θ (Figure 2.4). Over all conditions spanning both the surfzone and inner-shelf, the mean albedo was 0.11, nearly twice previous estimates of open-ocean daily averaged albedo e.g., [Payne, 1972]. Although the minimum α_o values are consistent with α_θ under both light conditions, the binned mean α_o is roughly one α_o standard deviation higher than α_θ for all θ_s in both clear and diffuse light conditions (compare red diamonds and vertical bars to red dashed curve, Figure 2.4).

Depth-limited wave breaking is often well determined by the ratio of local wave height to water depth H_s/h e.g., [Thornton and Guza, 1983]. To investigate whether the elevated α_o is due to breaking-wave generated foam or rather due to surface wind speed (as in open ocean parameterizations), the relationship between $\langle\alpha_o\rangle$ (where $\langle\rangle$ denotes an hourly average) and $H_s^{(p)}/h_R$ is examined, where $H_s^{(p)}$ is the pier-end ($x = -270$ m) significant wave height and h_R is the water depth at the radiometer ($x_R = -100$ m). Hourly-averaged $\langle\alpha_o\rangle$ varies between 0.04–0.33 and is strongly related to $H_s^{(p)}/h_R$ (Figure 2.5a) with $r^2 = 0.64$. Wind speeds at this location were typically weak; mean winds were ≈ 2 m s^{-1}, and sustained winds over 4 m s^{-1} were observed less than 12% of the time. As expected, winds were not correlated with $\langle\alpha_o\rangle$ (Figure 2.5b) since total ocean reflectance when winds are less than 8 m s^{-1} is negligible [Koepke, 1984] and whitecapping due to winds below 15 m s^{-1} has not been observed to enhance albedo [Payne, 1972, Frouin et al., 2001]. The relationship between $\langle\alpha_o\rangle$ and $H_s^{(p)}/h_R$ demonstrates that for larger incident waves $H_s^{(p)}$ or smaller local water depth h_R, $\langle\alpha_o\rangle$ is elevated in a consistent

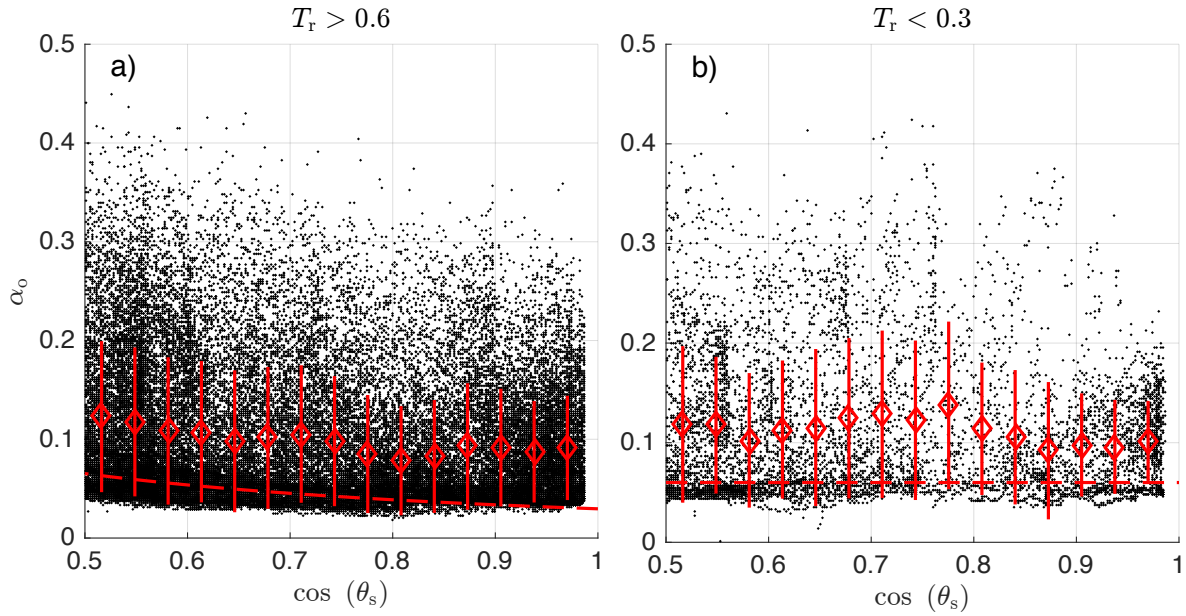

Figure 2.4: One-minute averaged observed albedo α_o versus $\cos(\theta_s)$ under (a) clear sky conditions ($T_r > 0.6$) and (b) diffuse light conditions ($T_r < 0.3$). Binned means (red diamonds) and $\pm$ one standard deviation (red vertical lines) of α_o are mostly elevated over the θ_s-only based [Taylor et al., 1996] parameterization α_{θ_s} (red dashed).

manner and confirms that the breaking-wave foam strongly contributes to the observed albedo, motivating the following two parameterization approaches.

2.4.2 Image-Based Parameterization

Following open-ocean whitecapping parameterizations e.g., [Hansen et al., 1983, Jin et al., 2004, Jin et al., 2011], surfzone albedo is expected to depend on θ_s and the breaking-wave generated foam fraction ζ_w. Time-averaged and snapshot images of the surfzone have successfully been used to identify areas with elevated foam e.g., [Lippmann and Holman, 1990, Stockdon and Holman, 2000]. Here, images from the pier-mounted GoPro camera are used to estimate ζ_w and compared to 1-Hz sampled α_o to derive an image-based albedo parameterization.

For a broken wave with extensive foam (Figure 2.6a), the 1-Hz sampled $\alpha_o = 0.33$, elevated above $\alpha_\theta = 0.06$. In contrast, for foam-free conditions (Figure 2.6b), $\alpha_o = 0.05$, con-

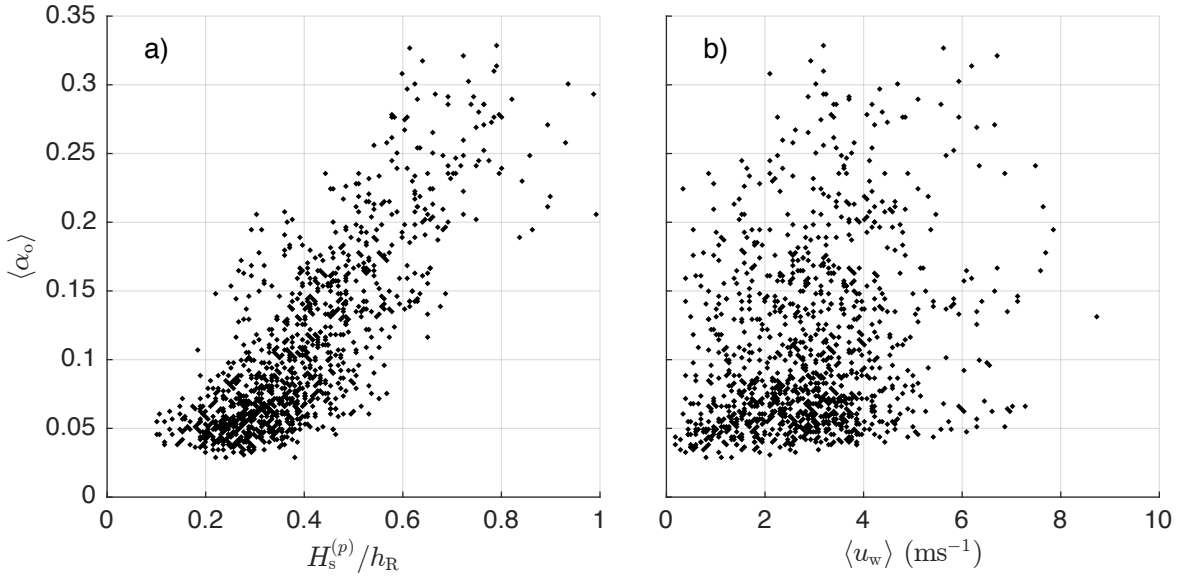

Figure 2.5: Hourly averaged observed albedo $\langle \alpha_o \rangle$ versus a) hourly-observed $H_s^{(p)}/h_R$ where $H_s^{(p)}$ is the significant wave height measured at the pier-end ($x = -270$ m) and h_R is the water depth at the radiometer, and b) hourly averaged wind speed. Correlation between albedo and wind speed at this site ($r^2 = 0.06$) is not significant from zero at the 95% confidence interval, however albedo is correlated with $H_s^{(p)}/h_R$ ($r^2 = 0.64$).

sistent with expected α_θ. The images were cropped and converted to 0–255 count grayscale G (Figures 2.6c and d) representing the ocean surface light intensity. The grayscale value $G = 0.2989r + 0.5870g + 0.1140b$, where r, b and g are the red, blue and green components respectively, retain luminance while removing hue and saturation. Elevated G can result from foam (white areas in Figure 2.6c) or sun glint (specular reflection, upper left Figure 2.6d). Typically, sun glint is brighter than foam, which is brighter than foam-free areas, allowing for differentiation between regions using grayscale values.

For the breaking case, the probability density function (PDF) of grayscale pixel values $p(G)$ contains three peaks near 100, 190 and 255 (Figure 2.6e), corresponding to areas of open water, foam and sun glint in Figure 2.6a. For the non-breaking case, $p(G)$ only has two peaks near 100 and 255 (Figure 2.6d) corresponding to open water and sun glint. The peak near 190 associated with foam (Figure 2.6c) is not present. To quantify image area containing open water,

foam and sun glint, all grayscale PDFs are first averaged together forming a mean $\overline{p}(G)$ (not shown). Similar to [Carini et al., 2015], PDF curvature $\overline{p}''(G)$ maxima define cutoff values between open water, whitewater and sun glint (lines on Figure 2.6e,f), here found to be $G = 170$ and $G = 230$. As foam is not a specular reflector [Monahan et al., 1986], sun glint must be from foam free regions and is thus classified as open water. The pixel fraction (as a proxy for surface area) of foam ζ_w is then calculated. For the breaking case (Figure 2.6e), the pixel fraction attributed to foam was $\zeta_w = 0.55$, and for the non-breaking case (Figure 2.6f) $\zeta_w = 0.03$. This approach is applied to all images, creating a time series of foam fraction $\zeta_w(t)$ at x_R.

Similar to open ocean whitecapping albedo formulations (2.4), the image-derived albedo α_I is

$$\alpha_I = \zeta_w \alpha_f + (1 - \zeta_w)\alpha_\theta, \tag{2.7}$$

where α_θ is the θ_s dependent parameterization for foam-free water, ζ_w is derived from the images, and the foam albedo α_f is considered a free parameter. The 1-Hz α_o varied over 0.02–0.45, spanning a broad range of solar zenith angle ($13.7^\circ < \theta_s < 56^\circ$), depth ($1.3 < h < 2.6$ m) and wave height ($0.45 < H_s < 1.21$ m) conditions. Minimizing the rms error between α_I and α_o results in a best fit $\alpha_f = 0.465$ and a surfzone albedo parameterization with high skill ($r^2 = 0.90$ with binned-mean $r^2 = 0.97$, Figure 2.7).

The high skill of the parameterized α_I is highlighted with a ten-minute example including several breaking wave events from larger wave-groups at 1-2 minute intervals (Figure 2.8). Breaking waves caused observed albedo α_o (black line, Figure 2.8) to increase sharply (in a few seconds), well above α_θ (black dotted). Individual α_o peaks during a large wave-group event (around 200 s) were spaced near $T_p = 9$ s. The highest α_o values, near 0.35, occurred after two or more successive breaking waves almost completely covered the radiometer's field of view. Smaller α_o peaks occurred when breaking events partially filled the field of view or did not break as vigorously. After the initial step-like increase lasting a few seconds, the albedo decayed toward α_θ with time scales ≈ 20 s as the bubbly foam outgassed e.g., [Ma et al., 2011]. The asymmetry

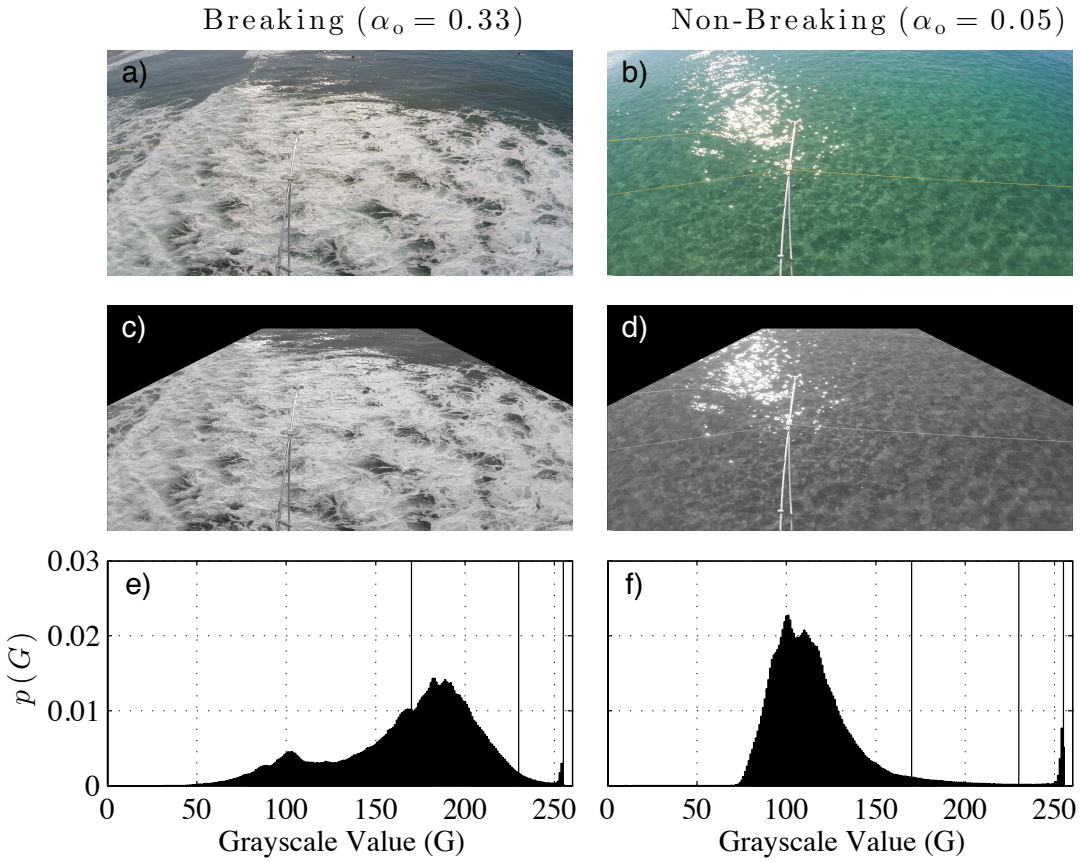

Figure 2.6: Images of water below the radiometer (a) during a breaking event when $\alpha_o = 0.33$ and (b) under calm non-breaking conditions when $\alpha_o = 0.05$. Cropped and grayscale converted images of (c) a breaking wave and (d) non-breaking. PDFs of the grayscale values for (e) breaking conditions and (f) non-breaking conditions are delineated (vertical black lines) to show grayscale pixel values classed as "open water" ($G < 170$), "foam" ($170 < G < 230$) and "sun glint" ($G > 230$). The fraction of pixels identified as "foam" (ζ_w) is 0.55 under breaking conditions (left), but only 0.03 for non-breaking conditions (right).

of the observed albedo α_o rapid increases and slower outgassing decay are well represented by α_I (red curve, Figure 2.8), and α_I tracks α_o at both wave group and individual-wave timescales. At α_o peaks (particularly > 0.2), after a rapid increase, parameterized α_I tends to have a high bias (Figure 2.8). This elevated α_I bias for $\alpha_o > 0.2$ is also seen in the scatterplot (Figure 2.7) and is discussed further in section 4.5. Overall this image-based parameterization predicts the foam-induced elevated α_o unexplained by α_θ (Figure 2.4), and the good α_I and α_o time-series

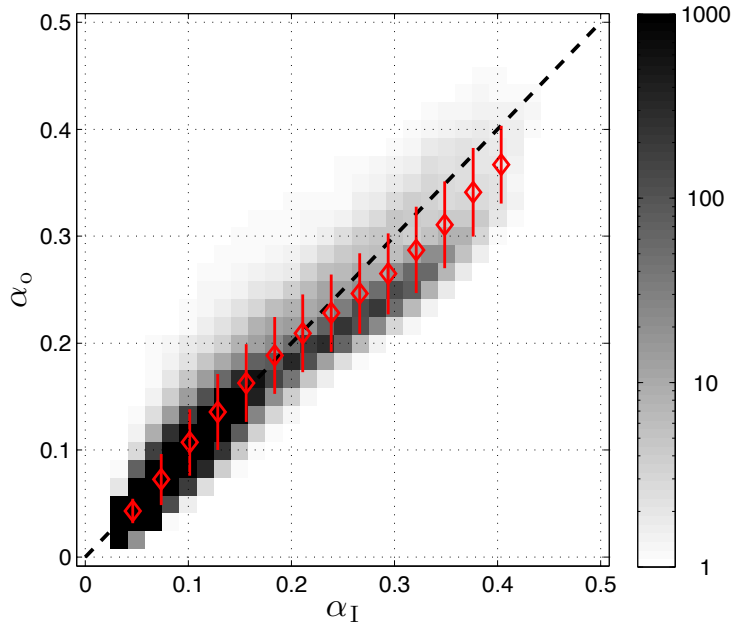

Figure 2.7: Gridded logarithmic density (gray scale) of image-derived albedo α_I versus observed albedo α_o sampled at 1 Hz for nine days ($N = 137,547$). The observations were made when θ_s varied between 13.7° and 56°, depth h varied between 1.3 m and 2.6 m, and pier-end H_s varied between 0.45 m and 1.21 m. The best fit $\alpha_f = 0.465$ has fit skill $r^2 = 0.90$ with binned mean (red diamonds) fit skill $r^2 = 0.97$. Binned-mean standard deviations are represented by red lines. Bins contained at least 100 observations.

agreement (Figure 2.8) is also seen at other times and over a wide variety of surfzone conditions.

2.4.3 Wave Model Based Albedo Parameterization

Although the image-based parameterization has very high skill, a camera is required, which often is not available. However, given knowledge of one dimensional $h(x)$, wave transformation models have high skill in predicting the cross-shore evolution of wave height e.g., [Ruessink et al., 2001, Ruessink et al., 2003]. This motivates a second albedo parameterization that utilizes a wave model to relate roller dissipation to foam fraction and albedo through (2.4).

Assuming normally-incident narrow-banded waves on alongshore uniform beaches, one-dimensional wave and roller transformation models e.g., [Thornton and Guza, 1983, Battjes and

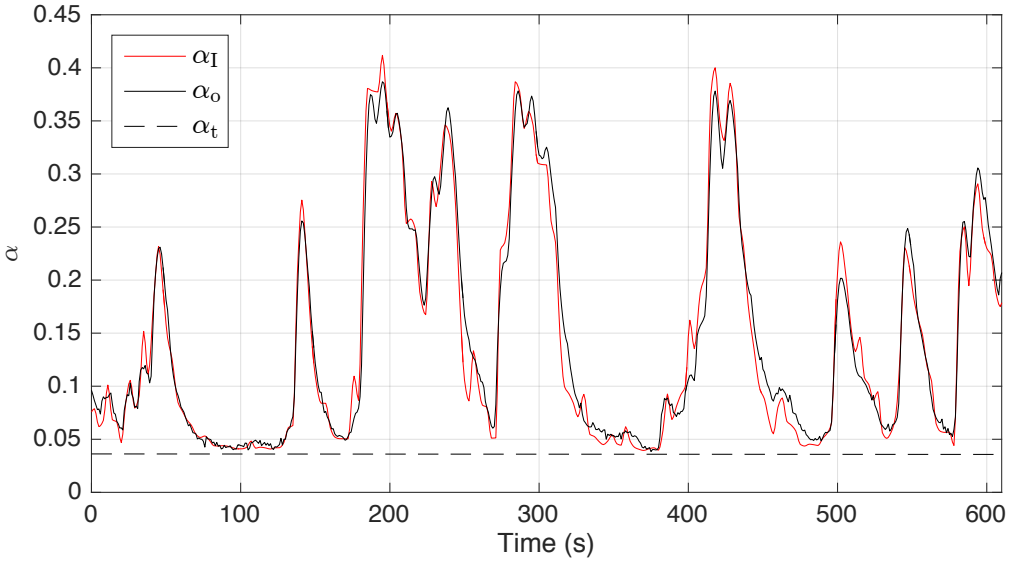

Figure 2.8: Ten-minute time series of image-derived albedo α_I (red), observed albedo α_o (black) and parameterized open ocean albedo α_θ (dashed) beginning near noon on September 11, 2015. Water depth $h(x_R) = 1.5$ m with moderate waves ($H_s = 0.6$ m and $T_p = 9$ s at the pier-end) and light winds ($|u_w| = 3.7\ \mathrm{m\,s^{-1}}$) with $\theta_s = 31°$.

Stive, 1985, Ruessink et al., 2001] relate wave energy flux gradient to wave-energy dissipation,

$$\frac{d}{dx}(EC_g) = -\langle \varepsilon_b \rangle, \tag{2.8}$$

where E is the wave energy density, C_g is the group velocity given by linear theory, and $\langle \varepsilon_b \rangle$ is the bulk breaking wave dissipation. The wave energy density is $E = 1/16 \rho g H_s^2$ where ρ is water density, g is gravity and H_s is the local significant wave height. The breaking wave dissipation $\langle \varepsilon_b \rangle$ is given by [Church and Thornton, 1993] with standard breaking parameters ($B = 0.9$ and $\gamma = 0.57$). The roller energy equation is e.g., [Ruessink et al., 2001]

$$\frac{d}{dx}(2E_r c) = -\langle \varepsilon_r \rangle + \langle \varepsilon_b \rangle, \tag{2.9}$$

where E_r is the roller energy density and c is the linear theory phase speed. Roller dissipation is

defined as [Deigaard, 1993]

$$\langle \varepsilon_r \rangle = \frac{2gE_{\mathrm{r}} \sin \beta}{c} \tag{2.10}$$

with slope $\beta = 0.1$ e.g., [Walstra et al., 1996]. The coupled equations (2.8 and 2.9) are solved with the specified $h(x)$ and offshore (pier-end) boundary conditions of observed H_{s} and T_{p}, with $E_{\mathrm{r}} = 0$.

Example output from the wave and roller model characterizes the cross-shore evolution of H_{s} (Figure 2.9a) due to the bathymetric profile (Figure 2.9e). As waves shoal onshore, wave height increases to $H_{\mathrm{s}} = 1.5$ m at $x = -170$ m where breaking occurs, roller dissipation becomes non-zero (Figure 2.9b) and wave height decreases. The terraced, non-monotonic bathymetry create undulating regions of elevated $\langle \varepsilon_r \rangle$ (e.g., near $x = 140$ m, $x = 90$ m, Figure 2.9b) and weaker $\langle \varepsilon_r \rangle$ (e.g., near $x = 125$ m and $x = 65$ m).

To develop a wave-model based albedo parameterization α_{w}, the average foam fraction $\langle \zeta_{\mathrm{w}} \rangle$ is hypothesized to depend linearly on non-dimensional ($\widehat{\ }$) wave roller dissipation $\langle \widehat{\varepsilon_r} \rangle$ as

$$\langle \zeta_{\mathrm{w}} \rangle = m \langle \widehat{\varepsilon_r} \rangle, \tag{2.11}$$

where $\langle \widehat{\varepsilon_r} \rangle$ is non-dimensionalized by wave-dissipation scaling e.g., [Battjes, 1975, Feddersen and Trowbridge, 2005, Feddersen, 2012b, Feddersen, 2012a] as

$$\langle \widehat{\varepsilon_r} \rangle = \frac{\langle \varepsilon_r \rangle}{\rho (gh)^{3/2}}, \tag{2.12}$$

and m is a fit parameter found by minimizing rms error between α_{o} and α_{w}. The hourly averaged wave-model based albedo is found from (2.4) using $\langle \zeta_{\mathrm{w}} \rangle$ and $\alpha_{\mathrm{f}} = 0.465$ as in section 2.4.2. The radiometer observed α_{o} is a cosine angle weighted area-average with ≈ 14 m radius. To compare the observed albedo with the parameterized albedo, $\langle \zeta_{\mathrm{w}} \rangle$ is also area-averaged with an identical cosine weighted response centered at x_{R}. The resulting foam fraction $\overline{\langle \zeta_{\mathrm{w}} \rangle}$ is both time

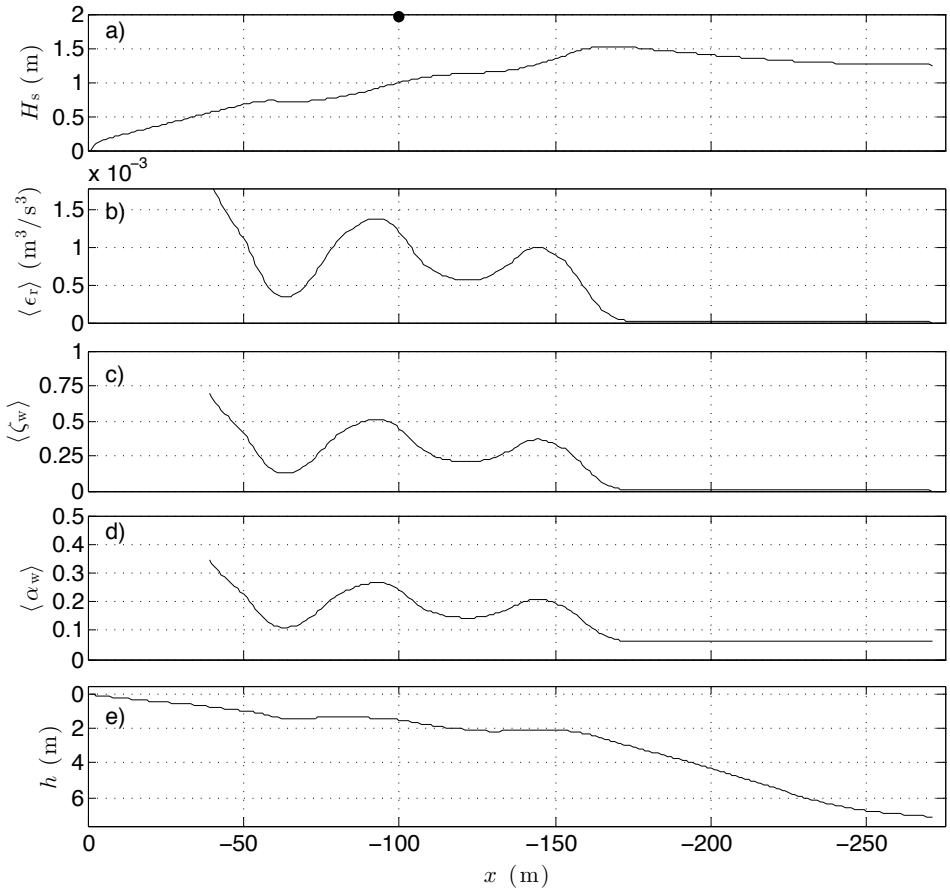

Figure 2.9: (a) Modeled significant wave height H_s, (b) modeled wave-roller dissipation $\langle \varepsilon_r \rangle$, (c) inferred mean foam fraction $\langle \zeta_w \rangle$, (d) wave-model parameterized albedo $\langle \alpha_w \rangle$, and (e) bathymetry profile $h(x)$ versus cross-shore coordinate x for noon on February 8, 2015. The black dot indicates the radiometer cross-shore location (x_R), which measured $\langle \alpha_o \rangle = 0.27$ under clear skies ($T > 0.6$) while $\theta_s \approx 48^\circ$ at this time. The wave model was initialized with one-hour averaged $H_s = 1.3$ m and $T_p = 13.4$ s measured at the pier-end (assuming incident waves). Modeled quantities are not shown for $h < 0.5$ m.

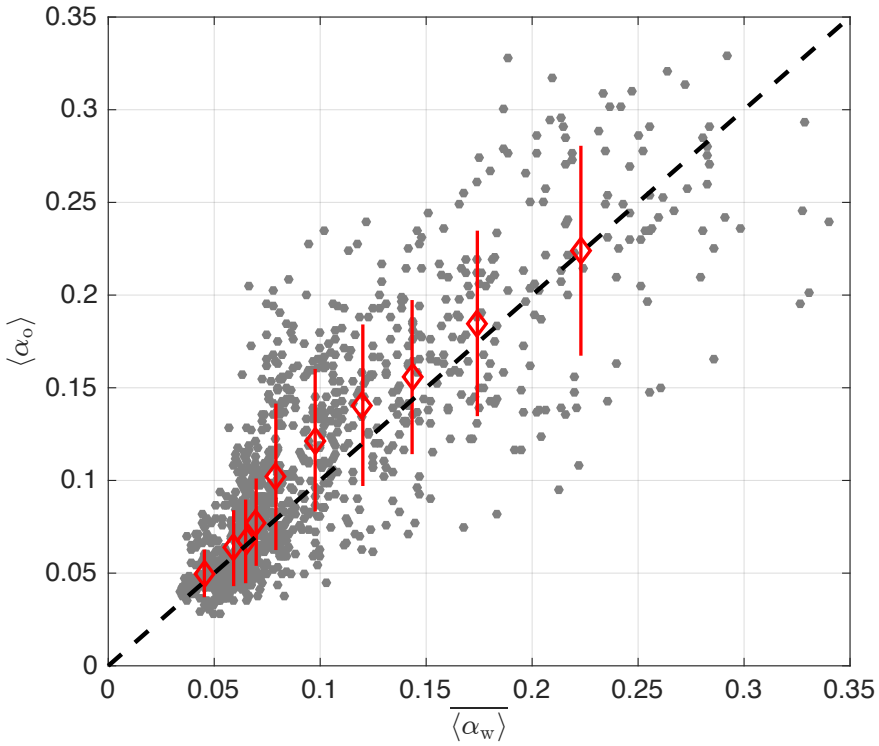

Figure 2.10: Hourly-averaged observed albedo $\langle \alpha_o \rangle$ versus the wave-model albedo parameterization $\overline{\langle \alpha_w \rangle}$ ($N = 1169$). The 1:1 line (dotted) is shown with binned means (red diamonds) and $\pm$ standard deviation (red lines). The best fit slope $m = 398$ and skill $r^2 = 0.68$ (binned-mean $r^2 = 0.94$).

and area averaged (where $\overline{\quad}$ denotes an area average) and the resulting time and area averaged wave-model based albedo $\overline{\langle \alpha_w \rangle}$ is found from (2.4).

When the radiometer sampled the surfzone (at x_R, $H_s/h \geq 0.57$), the mean observed surfzone albedo α_o was 0.15, over twice the daily average open ocean albedo parameterization of 0.06. The observed hourly averaged albedo $\langle \alpha_o \rangle$ varied between 0.04 and 0.33, greater than the open ocean albedo parameterization more than 80% of the time. The parameterized $\overline{\langle \alpha_w \rangle}$ was a good predictor of $\langle \alpha_o \rangle$ with significant skill ($r^2 = 0.68$) when best fit parameter $m = 398$ (dots in Figure 2.10). The parameterized binned mean $\overline{\langle \alpha_w \rangle}$ (red diamonds in Figure 2.10) has high skill ($r^2 = 0.94$) over these widely ranging and elevated albedo conditions. Factors contributing to variance in the binned quantities is discussed in section 4.5.

Although $\overline{\langle \alpha_w \rangle}$ is generated from hourly-averaged wave statistics, $\overline{\langle \alpha_w \rangle}$ is able to track albedo changes on time scales related to θ_s, h and H_s (Figure 2.11). For example, over six days, the combined effects of θ_s and wave energy at x_R cause the daily average of both $\langle \alpha_o \rangle$ and $\overline{\langle \alpha_w \rangle}$ to vary between 0.06 and 0.18. Albedo also varied by 0.16 in only 4 hours on day 2 associated with changes in H_s/h, yet there is still good agreement between $\overline{\langle \alpha_w \rangle}$ and $\langle \alpha_o \rangle$. Albedo estimation at specific cross-shore locations is also possible. The parameterized cross-shore foam fraction $\langle \zeta_w \rangle$ varies from zero offshore to local maxima of $\langle \zeta_w \rangle = 0.3$ and $\langle \zeta_w \rangle = 0.5$ at $x = -140$ m and $x = -90$ m, respectively (Figure 2.9c), consistent with the range of image inferred ζ_w. The resulting $\langle \alpha_w \rangle(x)$ (Figure 2.9d) is frequently above the θ_s dependent parameterization at this time ($\alpha_\theta = 0.06$) which is only valid in locations where there is no breaking. Surfzone albedo can also be parameterized with non-dimensionalized roller-energy instead of roller dissipation, with similar skill.

2.5 Discussion

Elevated surfzone albedo can impact heat budgets [Sinnett and Feddersen, 2014] and pathogen mortality e.g., [Sinton et al., 2002]. Water-entering short-wave solar radiation Q_{sw} is the largest surfzone heat budget term [Sinnett and Feddersen, 2014]. An average surfzone albedo increase from $\alpha = 0.06$ to (as observed) $\alpha = 0.15$ would reduce Q_{sw} so that cross-shore advection or wave heating are relatively more important. For example, the [Sinnett and Feddersen, 2014] heat budget found a residual surfzone heat export of 5.2×10^3 W m^{-1}. Revising the heat budget using $\alpha = 0.15$, reduces the residual heat export by 30%. Dye tracer can linger in the surfzone for $>$ 12 h [Hally-Rosendahl et al., 2014], indicating the time-scales pathogens can remain in bathing waters. Increasing albedo from 0.06 to 0.15 roughly doubles fecal coliform bacterial survival rates [Sinton et al., 2002], increasing potential human health risk if not appropriately accounted for.

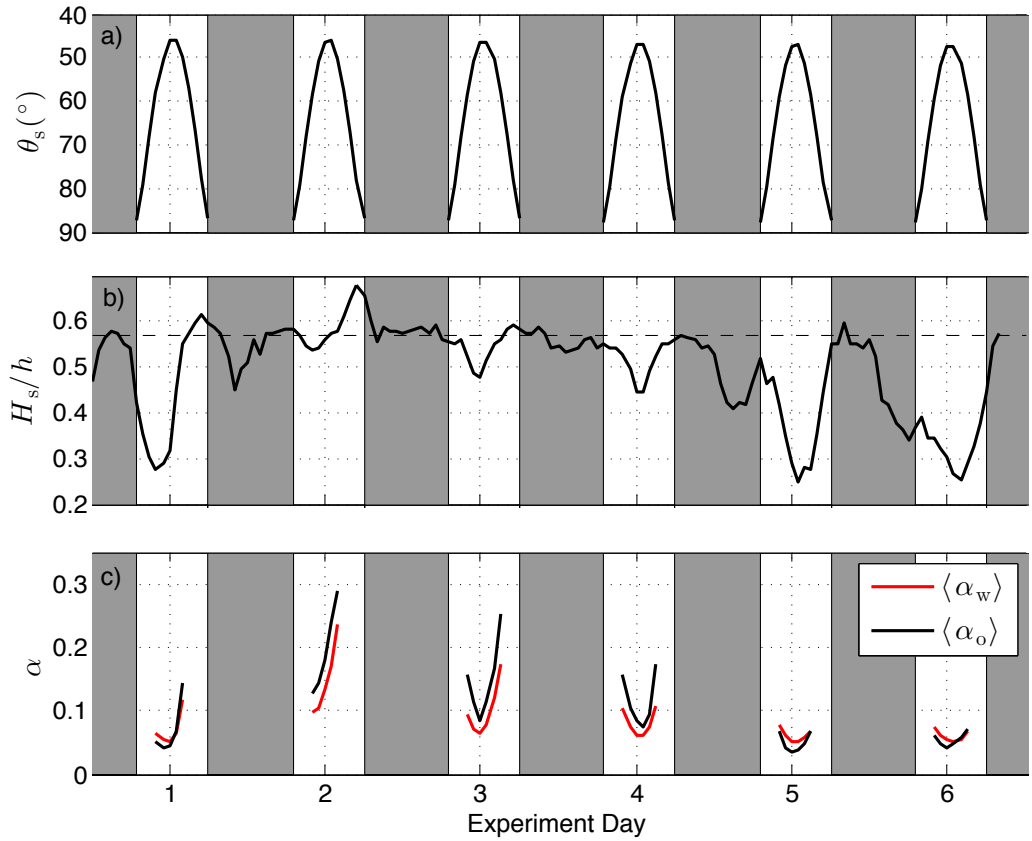

Figure 2.11: Six day time series (October 25-30, 2014) of (a) solar zenith angle θ_s, (b) depth normalized significant wave height H_s/h at x_R with expected threshold of significant wave breaking (dotted) (c) observed albedo $\langle \alpha_o \rangle$ (black) and wave parameterized albedo $\langle \alpha_w \rangle$ (red). Nighttime ($\theta_s > 90$) is shaded.

The observed albedo α_o is a space and time-average over the radiometer's 14-m radius cosine response and 2.9 s time constant. With propagating breaking waves which continuously outgas bubbles, the radiometer will never instantaneously sample pure foam over its entire field of view. This may explain why the best-fit foam albedo $\alpha_f = 0.465$ is less than the laboratory observed maximum value of 0.55 [Whitlock et al., 1982]. Although the image-based α_I predicts α_o with high skill (Figure 2.7), for $\alpha_o > 0.2$, α_I is biased high particularly when a breaking wave front passes and $d\alpha/dt$ is large (Figure 2.8). The 2.9 s radiometer response time, relative to the near-instantaneous camera response time, may explain this bias at times of step function-like changes in albedo.

The specific grayscale PDF cutoff limits for open water, foam, and sun glint, derived from $\overline{p}''(G)$ extrema, are the result of the lighting and fixed camera settings at this location. To apply this parameterization with another camera or at another location, one must first establish the relevant $\overline{p}''(G)$ based cutoff limits. This method can also be applied to time-averaged images. Good agreement between α_I and α_o was found with a constant foam albedo α_f applied to grayscale values within the foam cutoff limits. The fit may be improved if α_f is a function of G. Furthermore, images were not georectified. The images were cropped to limit the field of view to a relatively small area beneath the radiometer, and the 45° camera angle caused the imaged pixel area to have a similar spatial response as the radiometer. For example, the pixels near the top of the image cover roughly 35% more area than the pixels near the bottom, and the radiometer cosine response reduces the signal by roughly 40% near the top of the image. As the camera and radiometer were sampling with similar spatial weights, image rectification was not needed. However, image rectification may be required if this parameterization technique is applied to images covering a wider area (*e.g.*, ARGUS), or to images taken at shallower angles.

When breaking occurs, $\langle\alpha_o\rangle$ is elevated above α_θ (Figures 2.3,2.4), and the wave-model based parameterization has good skill ($r^2 = 0.68$) in predicting α_o (Figure 2.10), although significant unexplained variance remains. Waves were assumed to be normally-incident (as expected for long-period waves in $h < 6$ m), and standard wave and roller model coefficients were used. The bathymetry near piers is often scoured [Elgar et al., 2001], which may result in pier-based bathymetry measurement errors. Depth h errors and wave model errors would induce roller energy dissipation $\langle\varepsilon_r\rangle$ errors, and eventually $\langle\alpha_w\rangle$ errors, potentially contributing to the unexplained variance in Figure 2.10.

2.6 Summary

Breaking-wave induced foam elevates albedo α relative to foam-free ocean. Open-ocean albedo parameterizations account for foam through a wind speed dependent whitecapping foam fraction ζ_w. However, surfzone depth-limited wave breaking does not depend on wind, and wind-based foam fraction parameterizations are inaccurate in the surfzone. Measuring albedo in the energetic surfzone environment is difficult, and observations of surfzone albedo are very rare. The variability of surfzone albedo is not known, and parameterizations have not been available. Ocean-entering shortwave solar radiation Q_{sw} depends on albedo and affects both temperature variability and pathogen mortality. This motivates new observations of surfzone albedo and the development of two surfzone albedo parameterizations based on camera images and a wave model.

A year-long experiment at the Scripps Institution of Oceanography pier observed upwelling Q_u and downwelling Q_d shortwave radiation spanning the surfzone and inner-shelf over a range of wave and depth conditions. A two-way radiometer was mounted 6.5 m above the mean ocean surface and 6.35 m away from the pier, limiting pier shadow effects. Additional wave, wind, tidal and bathymetric observations were collected. On nine days, a downward-looking GoPro camera fixed above the radiometer location continuously captured water surface images. For solar zenith angle $\theta_s < 60°$, one-minute averaged observed albedo (as large as $\alpha_o = 0.45$) far exceeded the open ocean solar zenith angle parameterized albedo of 0.06. The elevated observed albedo was related to breaking wave conditions under the radiometer and observed albedo was not related to the wind speed.

A surfzone albedo parameterization is developed using images to estimate foam fraction ζ_w, identified by the distribution of grayscale pixels values. This image-based parameterization has high skill ($r^2 = 0.90$), with a best-fit parameter for foam albedo of $\alpha_f = 0.465$, slightly less than laboratory maximum of 0.55 likely due to radiometer finite time and spatial response. This

parameterization captures albedo variability on the time-scales of individual waves (9 s) and wave groups (minutes).

A wave-model based parameterization relates non-dimensionalized wave roller energy dissipation to the hourly-averaged foam fraction $\langle \zeta_w \rangle$ and, thus, to albedo. The wave model is initiated with bathymetry and incident wave conditions. This parameterization predicts hourly averaged observations from the radiometer, has good skill ($r^2 = 0.68$), and can resolve cross-shore albedo variations. Bathymetry or wave model errors may contribute to unexplained variance. These new parameterizations are applicable where imagery (*e.g.*, ARGUS) or nearshore wave models are available, and can be used to constrain local heat budgets and pathogen mortality estimation.

2.7 Acknowledgments

This work was supported in part by ONR and NSF. Gregory Sinnett was supported by a NSF GK12 fellowship and the SIO graduate department. Radiometer boom arm was developed and deployed by B. Woodward, B. Boyd, K. Smith, and R. Grenzeback. Deployment and recovery above difficult surfzone conditions was aided by C. McDonald, R. Walsh, S. Mumma, G. Boyd, L. Parry and the San Diego lifeguards. G. Castelao helped maintain the radiometer during deployment. Wave data was provided by the Coastal Data Information Program (CDIP) with special assistance from W. O'Reilly and C. Olfe. Wind and tidal data was gathered from NOAA station 9410230. Two anonymous reviewers significantly improved this manuscript. We would like to sincerely thank these people and organizations.

Chapter 2, in full, is a reprint of material as it appears in Sinnett, G., and F. Feddersen (2016), "Observations and parameterizations of surf- zone albedo", Methods Oceanogr., 17, 319334. The dissertation author was the primary investigator and author of this paper.

Chapter 3

Observations of Nonlinear Internal Wave Runup to the Surfzone

3.1 Abstract

The cross-shore evolution of nonlinear internal waves (NLIWs) from 8 m depth to shore was observed by a dense thermistor array and ADCP. Isotherm oscillations spanned much of the water column at a variety of periods. At times, NLIWs propagated into the surfzone, decreasing temperature by ≈ 1 °C in five minutes. When stratification was strong, temperature variability was strong and coherent from 18 m to 6 m depth at semi-diurnal and harmonic periods. When stratification weakened, temperature variability decreased and was incoherent between 18 m and 6 m depth at all frequencies. In 8 m depth, onshore coherently propagating NLIW events had associated rapid temperature drops (ΔT) up to 1.7°C, front velocity between 1.4 $\mathrm{cm\,s^{-1}}$ and 7.4 $\mathrm{cm\,s^{-1}}$ and incidence angles between -5° and 23°. Front position, ΔT, and two-layer equivalent height (z_{IW}) of four events were tracked upslope until propagation terminated. Front position was quadratic in time, and normalized ΔT and z_{IW} both decreased, collapsing as a linearly decaying function of normalized cross-shore distance. Front speed and deceleration are consistent with two-layer upslope gravity current scalings. During NLIW rundown, near-surface cooling and near-bottom warming in 8 m depth Coincide with a critical gradient Richardson number, indicating shear-driven mixing.

3.2 Introduction

Internal waves (internal isopycnal oscillations) are ubiquitous in the coastal ocean. In coastal regions, nonlinear internal waves (NLIW) transport and vertically mix sediment, larvae and nutrients e.g., [Leichter et al., 1996, Pineda, 1999, Quaresma et al., 2007, Omand et al., 2011]. As an aggregation mechanism, internal waves can generate patches and fronts of swimming plankters e.g., [Lennert-Cody and Franks, 1999, Jaffe et al., 2017]. In the nearshore (defined here as depths $h < 20$ m) NLIWs can drive temperature fluctuations of up to 6°C at tidal and higher frequencies e.g., [Winant, 1974, Pineda, 1991, Walter et al., 2014]. The nearshore semi-diurnal

internal tide can transport nutrients onshore [Lucas et al., 2011b, Lucas et al., 2011a], which can cause phytoplankton blooms [Omand et al., 2012]. Nearshore NLIWs were also correlated with the presence of phosphate and fecal indicator bacteria near the surfzone [Wong et al., 2012]. Although important to nearshore ecosystems, the cross-shore transformation of NLIWs in very shallow water, particularly to the surfzone, is poorly understood.

NLIWs that propagate into the nearshore may be either remotely or locally (on the shelf) generated [Nash et al., 2012]. On the shelf, NLIW generation and propagation depends on the bathymetric slope e.g., [Garrett and Kunze, 2007], background stratification e.g., [Zhang et al., 2015], and barotropic tides e.g., [Shroyer et al., 2011] and can be modified by upwelling and regional-scale circulation [Walter et al., 2016]. In analogy to a surface gravity wave surfzone, as internal waves propagate into shallow water on subcritical slopes, they steepen, become highly nonlinear, and dissipate e.g., [Moum et al., 2003, MacKinnon and Gregg, 2005], creating an "internal surfzone" e.g., [Thorpe, 1999, Bourgault et al., 2008]. NLIWs can have both wave and bore-like properties when propagating upslope on the shelf from 120 m to 50 m depth [Moum et al., 2007]. NLIWs sometimes form highly nonlinear solitons trailing the leading edge of the dissipating internal tidal bore e.g., [Stanton and Ostrovsky, 1998, Holloway et al., 1999]. Farther onshore, internal wave runup occurs as an internal bore - sometimes termed a "bolus" e.g., [Bourgault et al., 2008] - in the "internal swashzone", analogous to surface bores with wave runup in the swashzone of a beach [Fiedler et al., 2015].

In the nearshore, NLIWs have been observed often as internal bores associated with the internal tide. In Monterey Bay (at $h = 15$ m), sharp temperature drops in the bottom 10 m associated with the M2 (12 hour period) internal tide steepen into a bore front and precede gradual cooling over several hours before temperature quickly recovers amid intensified mixing [Walter et al., 2012]. The 12-h evolution of a semi-diurnal non-linear internal bore near Del Mar California was tracked between 60 m and 15 m depth [Pineda, 1994]. In $h \approx 12$ m depth, internal tidal bores have been related to nutrient and larvae transport [Pineda, 1999]. Bottom trapped

(cold) bores were observed near Huntington Beach in the Southern California Bight in depths between 20 m and 8 m, attributed to breaking semi-diurnal internal waves [Nam and Send, 2011]. An onshore propagating nonlinear internal wavetrain was observed between 30 m and 10 m depth in a strongly stratified estuary that disintegrated into irregularly spaced, short duration bottom trapped bores [Bourgault et al., 2007], which generated turbulence as they dissipated [Richards et al., 2013]. Nearshore NLIWs can have significant temporal variation e.g., [Suanda and Barth, 2015] associated with multiple angles of incidence, and can strongly interact with one another [Davis et al., 2017]. High-frequency (periods of minutes) NLIW have also been observed to reflect off of steep internal beaches [Bourgault et al., 2011].

The internal surfzone and swashzone have been delineated in laboratory e.g., [Wallace and Wilkinson, 1988, Helfrich, 1992, Sutherland et al., 2013a] and numerical studies e.g., [Arthur and Fringer, 2014]. Laboratory studies of internal bores typically use a layered lock exchange e.g., [Shin et al., 2004, Marino et al., 2005] or motor driven paddle to create an internal disturbance e.g., [Wallace and Wilkinson, 1988, Helfrich, 1992], then quantify the speed and shape of the upslope surge of dense water based on layer density differences and total water depth. Analogous to surface wave breaking, conditions affecting the internal wave breaking regime and subsequent upslope evolution as a bore were found to be a function of an internal Iribarren number Ir (ratio of internal wave steepness to bathymetric slope) or offshore wave frequency and amplitude [Sutherland et al., 2013a, Moore et al., 2016]. The Ir also affected the total upslope bore dissipation and eventual transport of tracers [Arthur and Fringer, 2016]. However, the relationship between NLIW runup in the ocean and either idealized laboratory or numerical simulations is not clear.

Scripps beach, the Scripps Institution of Oceanography (SIO) Pier (La Jolla, CA), and surrounding canyons provide a natural laboratory to study NLIWs in shallow environments. Canyon currents have been linked to internal waves in this (and other) canyon systems [Shepard et al., 1974, Inman et al., 1976]. Recent observations in La Jolla canyon show an active internal

wave field at the semidiurnal frequency. Energy flux is up canyon as internal oscillations transition to higher harmonics (M4 and above), indicating onshore propagation of a highly nonlinear and evolving internal wave field [Alberty et al., 2017]. In 7 m water depth at the end of the SIO pier (this study location), bottom temperature can drop rapidly, 5 °C over minutes [Winant, 1974, Pineda, 1991]. With a 4-element cross-shore array on the Scripps pier, cold pulses were observed propagating onshore into the surfzone [Sinnett and Feddersen, 2014]. However, details of internal runup to the shoreline, variability and potential impacts to the nearshore are not well observed.

Here, observations are presented from a dense and rapidly sampling instrument array spanning the nearshore from 18 m depth all the way to the shoreline. Analysis is focused on describing the details of internal runup across the entire internal swashzone and relating these observations to idealized laboratory and numerical simulations. Experimental details are described in section 4.3.1, with some of the first time series and spectral observations of NLIW runup in water depths as shallow as $h = 2$ m in section 3.4. Observations of individual runup events are described in section 3.5 and related to laboratory and numerical studies. Discussion of these results are in section 3.6 and concluding remarks are in section 3.7.

3.3 Experimental Details

3.3.1 Location and Overview

Temperature and current observations at the SIO pier (La Jolla California, 32.867N, 117.257W) were made during fall (29 September to 29 October) 2014 when stratification in the Southern California bight is strong [Winant and Bratkovich, 1981]. The SIO pier is 322 m long and extends west-north-west (288°) into water roughly 7.6 m deep. It is $\approx$ 500 m southeast of Scripps Canyon, the northern arm of the La Jolla canyon system (Figure 3.1a). The shoreline is roughly alongshore uniform from 200 m north to 500 m south of the pier, with mean cross-shore

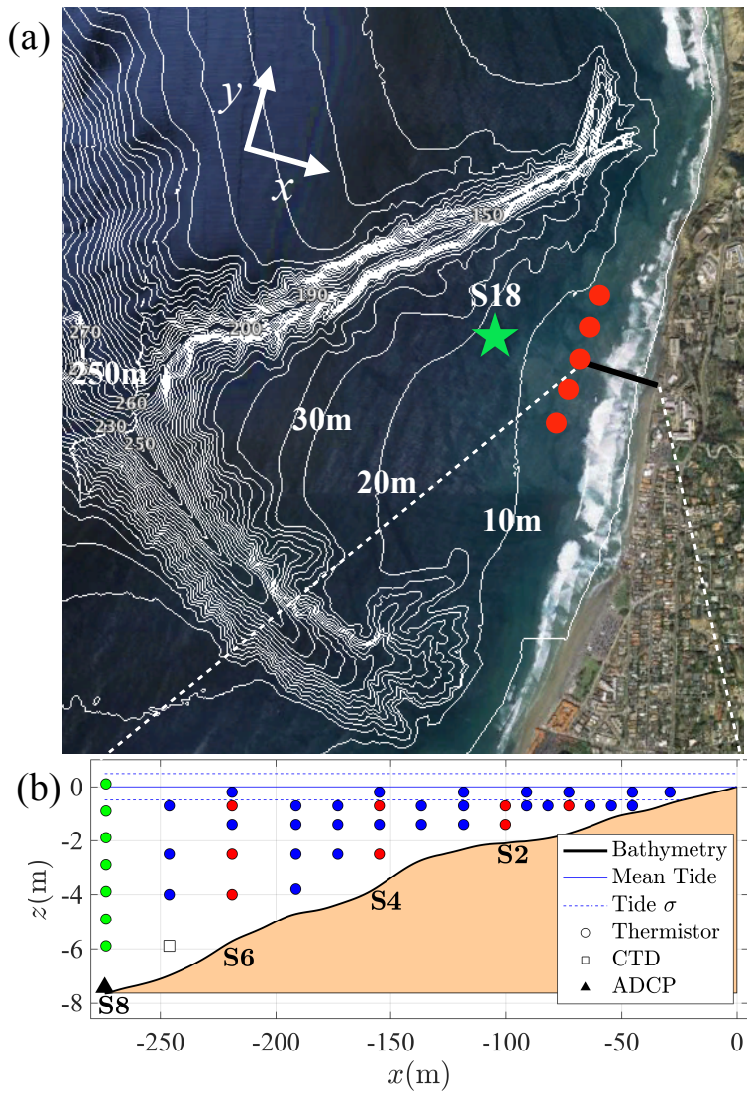

Figure 3.1: (a) Google Earth image of the experiment site (La Jolla California) and surrounding nearshore waters. The bathymetry (10 m contour interval, white lines) highlights the La Jolla (southern) and Scripps (northern) Canyon system. The site of a moored temperature chain near the 18 m isobath (green star, S18), bottom mounted thermistors (red dots) and the SIO pier (black line) are shown. The x coordinate is chosen to be along the pier (cross-shore). (b) Detail showing the cross-shore (x) instrument deployment locations along the SIO pier (symbols) with reference to the mean tide level $z = 0$ m (blue line), tidal standard deviation (blue dotted) and mean bathymetry (solid black). Three different types of thermistors were deployed, Onset TidBits (blue), SBE56 (red) and the CORDC temperature chain (green). Instrument sites near the 8 m, 6 m, 4 m and 2 m isobaths are indicated (S8, S6, S4, and S2).

slope $s \approx 0.027$ from the shoreline to $h = 18$ m depth before a steep canyon break. The reference depth ($z = 0$) is at the mean tide level (MTL), and the cross-shore origin ($x = 0$) is defined as the shoreline at MTL. The x coordinate axis is aligned with the length of the pier (positive onshore) making the y axis oriented alongshore (positive toward the north, Figure 3.1a). The alongshore origin ($y = 0$) is defined at the northern edge of the pier.

3.3.2 Instrumentation

For the 30–day experimental period, a vertical temperature chain was deployed at $h = 18$ m (denoted S18) directly offshore of the pier at $x = -657$ m, $y = 0$ m (green star, Figure 3.1a) with 14 Seabird SBE56 thermistors sampling at 2 Hz spaced 1 m apart extending from 1 m above the bed to 3 m below MTL. An additional SBE56 was tethered to a surface float which continually sampled near surface temperature at a fixed level relative to the tide. Concurrently, 36 Onset Hobo TidBits and 8 Seabird SBE56 thermistors were deployed on the SIO pier pilings ($y = 0$ m) at various cross-shore sites (-273 m $< x < -29$ m) and vertical locations (-5.9 m $< z < 0.1$ m) (blue and red circles, Figure 3.1b). These TidBits and SBE56s sampled water temperature at 3 min and 15 s intervals respectively, and were calibrated in the SIO Hydraulics Laboratory temperature bath, yielding accuracies of 0.01°C (TidBits) and 0.003°C (SBE56). The TidBits have a 5-minute response time and are capable of resolving oscillations at periods longer than 10 minutes.

A pier-mounted Seabird SBE 16plus SeaCAT maintained by the Southern California Coastal Ocean Observing System (SCCOOS) measured salinity and temperature at $x = -246$ m and $z = -5.8$ m (roughly 1.2 m above the bed), sampling every 6 min (square, Figure 3.1b). Salinity was linearly related to temperature over the experiment duration at this site, with salinity of 33.57 $\pm$0.05 90% of the time. A pier-end Precision Measurement Engineering (PME) vertical temperature chain with 1 m vertical resolution maintained by the SIO Coastal Observing Research and Development Center (CORDC) provided temperature measurements at 1 Hz sampling rate

with 0.01°C accuracy (green circles, Figure 3.1b). This temperature chain (installed to examine long-term trends) was offline from 2 October to 6 October, and again from 16 October to 18 October. Four additional SBE56 thermistors were mounted 0.3 m above the bed in depth $h \approx 7.6$ m at $x = -273$ m and alongshore locations spaced 100 m apart ($y = -200, -100, 100$ and 200 m, red dots, Figure 3.1a). These instruments were active 9-30 October and sampled temperature at 1 Hz to capture alongshore variation and incident event angle relative to the slope. Temperature data from near-surface pier-mounted thermistors was removed at times when they were exposed to air (low tide or large waves) following [Sinnett and Feddersen, 2014]. For convenience, the pier-mounted instrument site locations near the 8 m, 6 m, 4 m and 2 m isobaths ($x = -273$ m, -219 m, -155 m, and -100 m) are referred to as S8, S6, S4 and S2 (see Figure 3.1b) throughout the rest of the manuscript.

Water column velocity was observed by an upward looking Nortek Aquadopp current profiler deployed in 7.6 m depth at S8 (black triangle, Figure 3.1b). It sampled with 1 min averages and 0.5 m vertical bin size. The ADCP was placed 5 m north of the pier ($y = 5$) to reduce pier-piling flow disturbance, while remaining consistent with pier-mounted thermistors. Velocity data was rotated into the x and y coordinate system based on compass headings taken at deployment. Data above the surface wave trough or in regions with low acoustic return amplitude were removed (≈ 1.5 m below the tidal sea surface).

Meteorological and tide measurements were made by NOAA station 9410230 at S8. Air temperature and wind speed (two-minute average) were sampled at $z \approx 18$ m at six-minute intervals. Surface (tidal) elevation η is calculated from an average of 181 one-second samples reported every six minutes. Hourly significant wave height (H_s) and peak period (T_p) were observed by the Coastal Data Information Program (CDIP) station 073 (pressure sensor) mounted to a pier piling at S8. When observations were not available, (29 September to 21 October) a realtime spectral refraction wave model with very high skill initialized from offshore buoys was used [O'Reilly and Guza, 1991, O'Reilly, W.C. and Guza, R.T., 1998]. Cross-shore bathymetry

was measured from the pier deck using lead-line soundings every 10 m on 26 September, 10 October, and 24 October. The bathymetry was then interpolated in x and the time dependent bathymetry was used when appropriate. The average slope between S8 and S4 was $s = 0.033$ with bathymetry variation less than 0.3 m at any location (slope changes $< 4\%$) during the experiment. The outer extent of surface wave breaking (surfzone location x_{sz}) was estimated by shoaling surface wave conditions observed at S8 over the measured bathymetry with the observed tides following [Sinnett and Feddersen, 2016].

3.3.3 Background Conditions

The experiment site has a mixed barotropic tide with amplitudes over the 30 day experiment period varying between 0.17 m and 1.05 m on a spring-neap cycle, dominated by the lunar semi-diurnal (M2) and lunar diurnal (K1) tidal constituents (Figure 3.2a). Wind conditions were generally calm, with a light afternoon sea breeze rarely peaking above 5 $\mathrm{m\,s^{-1}}$ (Figure 3.2b). Pier-end (S8) significant wave height H_s varied from 0.3 to 1.5 m over the entire experimental period. Surface wave events near days 2, 19, 22 and 27 caused significant wave height to peak well above the mean $H_s \approx 0.7$ m. Air temperature followed a strong diurnal heating and cooling cycle in the first 10 days of the record, with diurnal variations $\approx 7^{\circ}$C (Figure 3.2d, black). The diurnal air temperature variation decreased to $\approx 4^{\circ}$C after day 10, with a subtle cooling trend seen throughout the record. Surface water temperature (from the S18 surface thermistor) varied weakly, but contained a diurnal heating and cooling signature (Figure 3.2d, red). Diurnal air and near-surface ($z > -3.5$ m) water temperature variability was coherent with a ≈ 4 h lag. Diurnal air and water temperature variability below $z = -3.5$ m was incoherent.

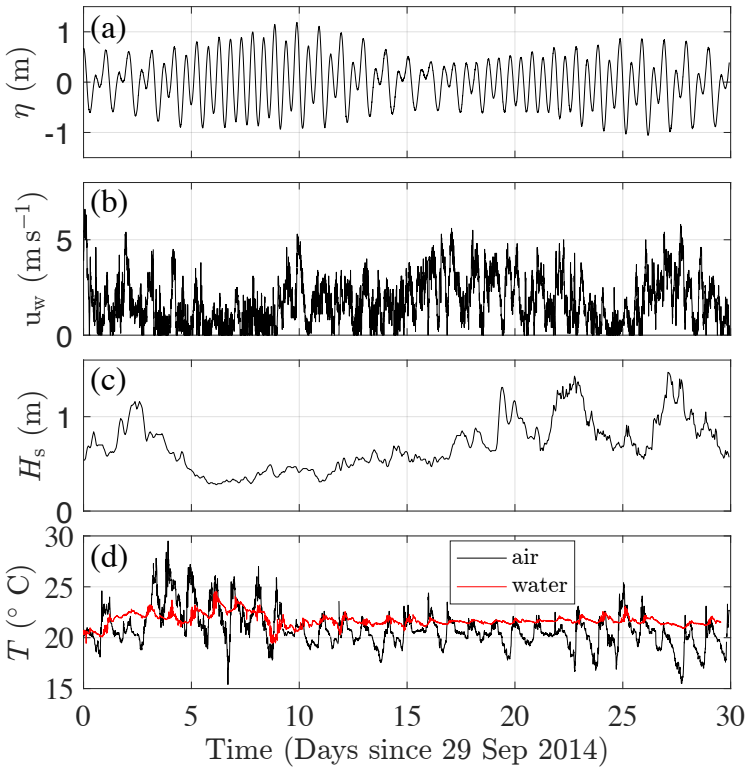

Figure 3.2: Observed (a) SIO pier tidal elevation η, (b) wind speed u_w, (c) significant wave height H_s at the SIO pier-end (S8) and (d) air (black) and surface ocean in 18-m depth (red) temperature versus time. Wave observations were made by the Coastal Data Information Program (CDIP) station 073. Tidal observations, wind speed and air temperature were observed by NOAA station 9410230 located at the pier-end.

3.4 Month-long Nonlinear Internal Wave observations from 18 m depth to shore

Temperature observations from 18 m depth to near the shoreline at five cross-shore locations (Figure 3.3a-e) highlight the rich and diverse NLIW field present during the 30 day observational period. The first 10 days were strongly stratified at S18 ($x = -657$ m, $h = 18$ m) with a large barotropic tide (Figure 3.3e). During this time, winds were typically calm, with a few events where $u_w > 4$ m s^{-1}. Significant wave height averaged 0.8 m during the first four days, then decreased to less than 0.5 m and remained small until day 19. An energetic NLIW field is present at S18 during the first 10 days, with large vertical isotherm excursions (20°C

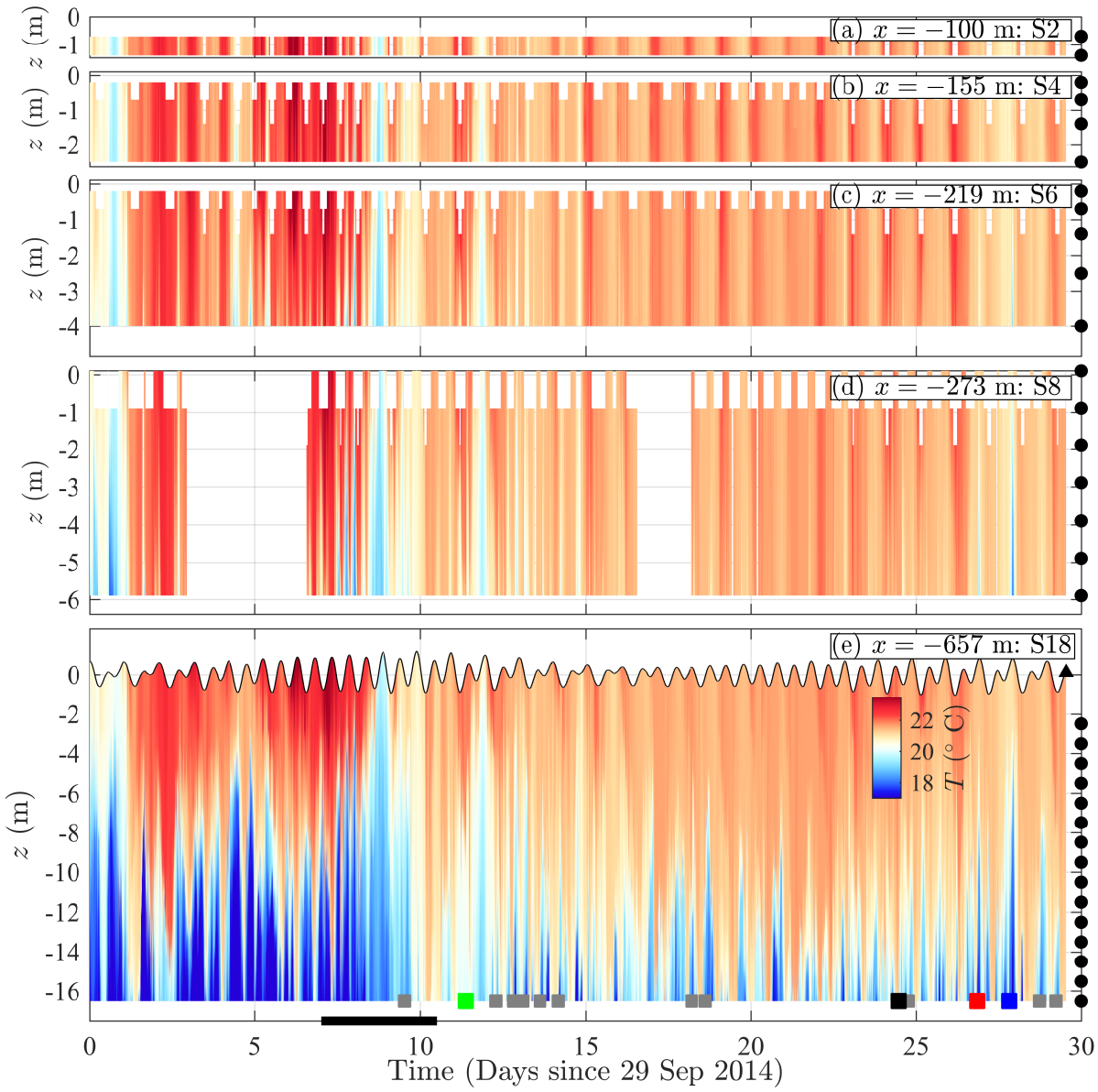

Figure 3.3: Temperature versus vertical location below the mean tide level (MTL) z and time at cross-shore locations (a) $x = -100$ m, $h \approx 2$ m, denoted S2 (b) $x = -155$ m, $h \approx 4$ m, denoted S4 (c) $x = -219$ m, $h \approx 6$ m, denoted S6 (d) $x = -273$ m, $h \approx 8$ m, denoted S8 (e) $x = -657$ m $h \approx 18$ m, denoted S18. The vertical axes have been scaled to approximate the depth at each cross-shore location (the vertical scale of plot (e) is compressed to fit on the page). Data in plots (a-d) have been removed (white) when sensors were inoperative or above the water line. Black dots (right side, all panels) indicate the fixed (relative to MTL) thermistor locations. The black triangle in (e) indicates the surface following sensor (surface level η shown as black line). Gray squares at the bottom of (e) indicate the arrival time of isolated events highlighted in section 3.5, and colored squares indicate the arrival time of events A-D (left to right) which are highlighted in detail in section 3.5. The black bar on the abscissa indicates the time span highlighted in Figure 3.4.

isotherm displacement is $\pm$6 m, Figure 3.3e). At this time, cross-shore coherent cooling events at semi-diurnal and faster time scales are regularly observed in the otherwise warm shallow water and can reduce the S4 temperature by 2.25°C in only 10 min. Clear examples of NLIW cross-shore excursions occur near days 1 and 8 (Figure 3.3). The 10 day period containing strong internal wave activity typical of early fall conditions at this site is denoted "period I".

The early to late fall transition between period I and the less active remaining 20 days (termed "period II") is characterized by cooling surface water ($z > -7$ m) and warming at depth (Figure 3.3e). The transition occurs just after day 10, when warm water extended all the way to the bottom at S18 with very weak stratification. At this time, surface gravity waves were weak ($H_s < 0.5$ m), sustained winds were moderate ($u_w < 5$ m s^{-1}) with spring barotropic tides (Figure 3.2). At S18, vertical excursions of the 20°C isotherm were smaller during period II, usually less than $\pm$3 m. Near surface diurnal temperature oscillations due to solar heating were $\pm$0.2°C at S18, increasing to $\pm$0.5°C at S2, and were coherently observed at all cross-shore locations. Though the water was less stratified and isotherm excursions were smaller at S18, NLIW events were still observed during period II (notable in Figure 3.3 near days 12 and 27). Cross-shore coherent NLIW events are described in greater detail by zooming in to a time of energetic NLIW activity (identified by the black bar, Figure 3.3e) during period I.

The 3.5-day energetic NLIW period (Figure 3.4) had strong stratification and barotropic tides but weak winds and surface waves. Temperature variability at all cross-shore locations is strong, containing oscillations at periods near M2, the M4 harmonic (6.2 hour period) and higher frequencies. At S18, the $T = 20$ °C isotherm excursions are over 10 m and NLIW events are coherently observed all the way to S2. Mid-water column temperature fluctuations are as high as 4.8 °C in 10 min at S18, but decrease onshore with a maximum temperature fluctuation of 2.0 °C at S2. The first 1.5 days (days 7 - 8.5) are strongly stratified with very warm surface water and a sharp thermocline. Near-bottom M4 temperature variability is present at all cross-shore locations. Stratification is weaker during days 8.5 to 10.5 (Figure 3.4), yet temperature variability

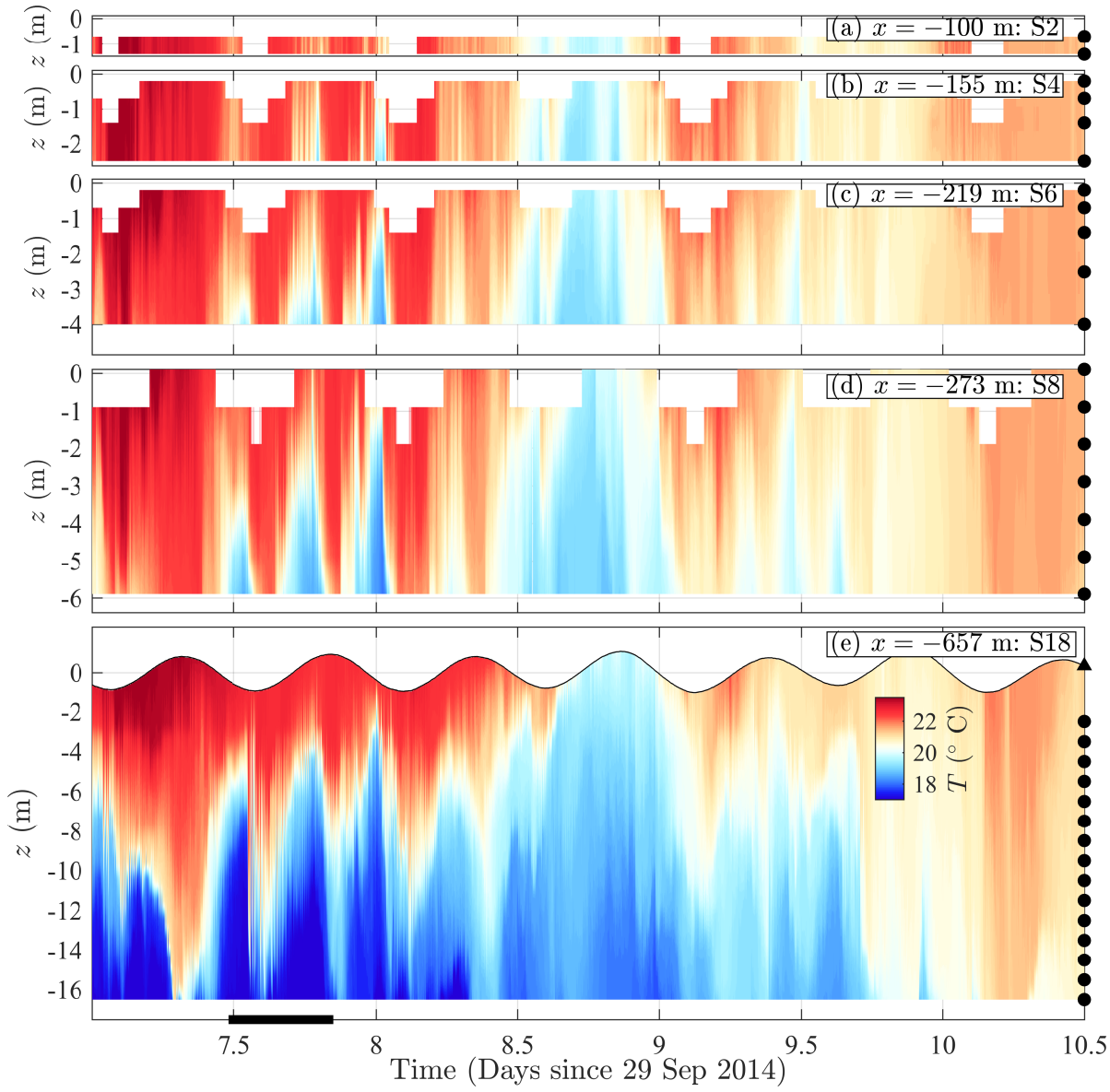

Figure 3.4: Similar to Figure 3.3, but with the time axes of all plots zoomed to highlight 3.5 days of internal wave activity. The black bar on the abscissa indicates the timespan included in Figure 3.5.

at all locations is still observed primarily at M2 periods, although M4 variability is also present particularly at S8 (Figure 3.4d).

High frequency temperature variability (periods shorter than 3 hours) is superimposed on top of the M2 and M4 variability. The cross shore evolution of high frequency variability is visible in a 9 hour zoom (Figure 3.5) of the time period indicated by the black bar in Figure 3.4e. At S18, the $T = 20$ °C isotherm gradually rises during the first hour with little high frequency temperature variability. Then, at hour 1.5, the 20°C isotherm plunges roughly 10 m, beginning a series of oscillations at $\approx$ 10 min period that persist over the next six hours (Figure 3.5e). The first two 10 m oscillations of the 20 °C isotherm near hour 2 are qualitatively similar to a soliton. These superimposed high frequency oscillations at S8 are present at S6, but decay in shallower water, though some aspects of the high frequency NLIW field are coherent upslope. For example, near hour 7 at S18 (the peak of the M4 period event) a pulse of cold water elevates S8 isotherms (lasting roughly 10 min). The cold pulse arrives at progressively later times upslope, until it is finally observed at S2 just before hour 8 (Figure 3.5a-d). The pulse propagated onshore at an unknown angle and affected temperature in water depths as shallow as 2 m, causing temperature there to drop 0.7 °C in five minutes.

Although occasional pulses of cold water can be tracked coherently upslope, very little high frequency energy is coherent between S18 and S8. A further zoom of 1.5 hours shows temperature with the 18.1°C, 19.6°C and 21.1 °C isotherms highlighted to emphasize the lack of cross-shore coherence at high frequency (Figure 3.6). At S18, isotherms are displaced $\pm$0.8 m at $\approx$ 10 min period (Figure 3.6e). At S8, isotherm displacements are $\pm$0.4, reduced from S18 (Figure 3.6d). However, isotherm displacements are not coherent between S18 and S8 with near zero correlation for all lags during this active 90 minute period. A transition to temperature variability on longer time scales and an upslope isotherm tilt is also evident in Figure 3.6, as the 90 min average 21.1 °C isotherm depth is approximately 2 m higher at S4 than at S18. At S8, both the 19.6°C and 21.1°C isotherms contain variability at $\approx$ 10 min periods, particularly in the

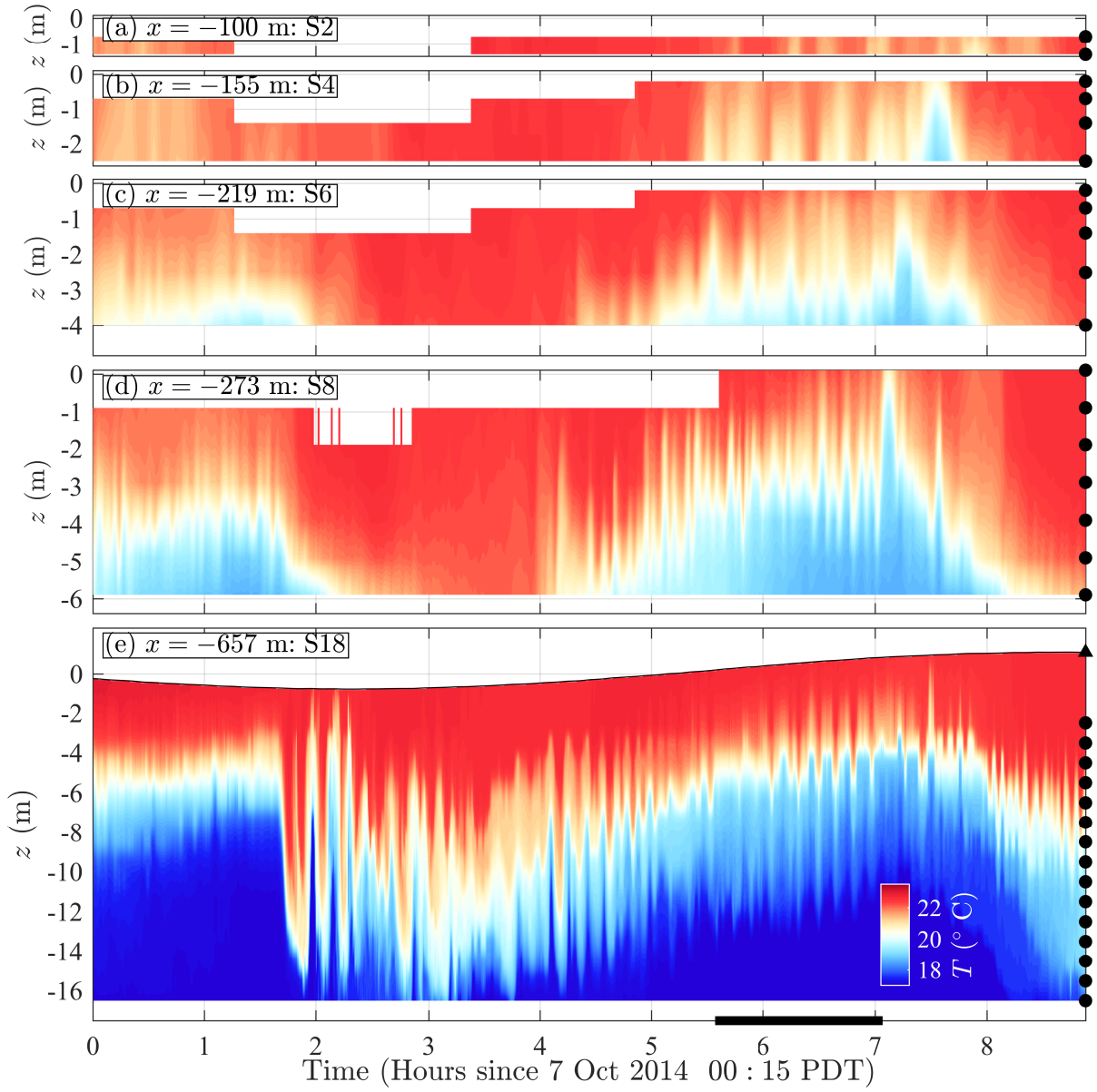

Figure 3.5: Similar to Figure 3.4, but with the time axes of all plots zoomed to highlight 9 hours beginning on 7 October 2014 00:15 PDT. The black bar on the abscissa indicates the timespan included in Figure 3.6

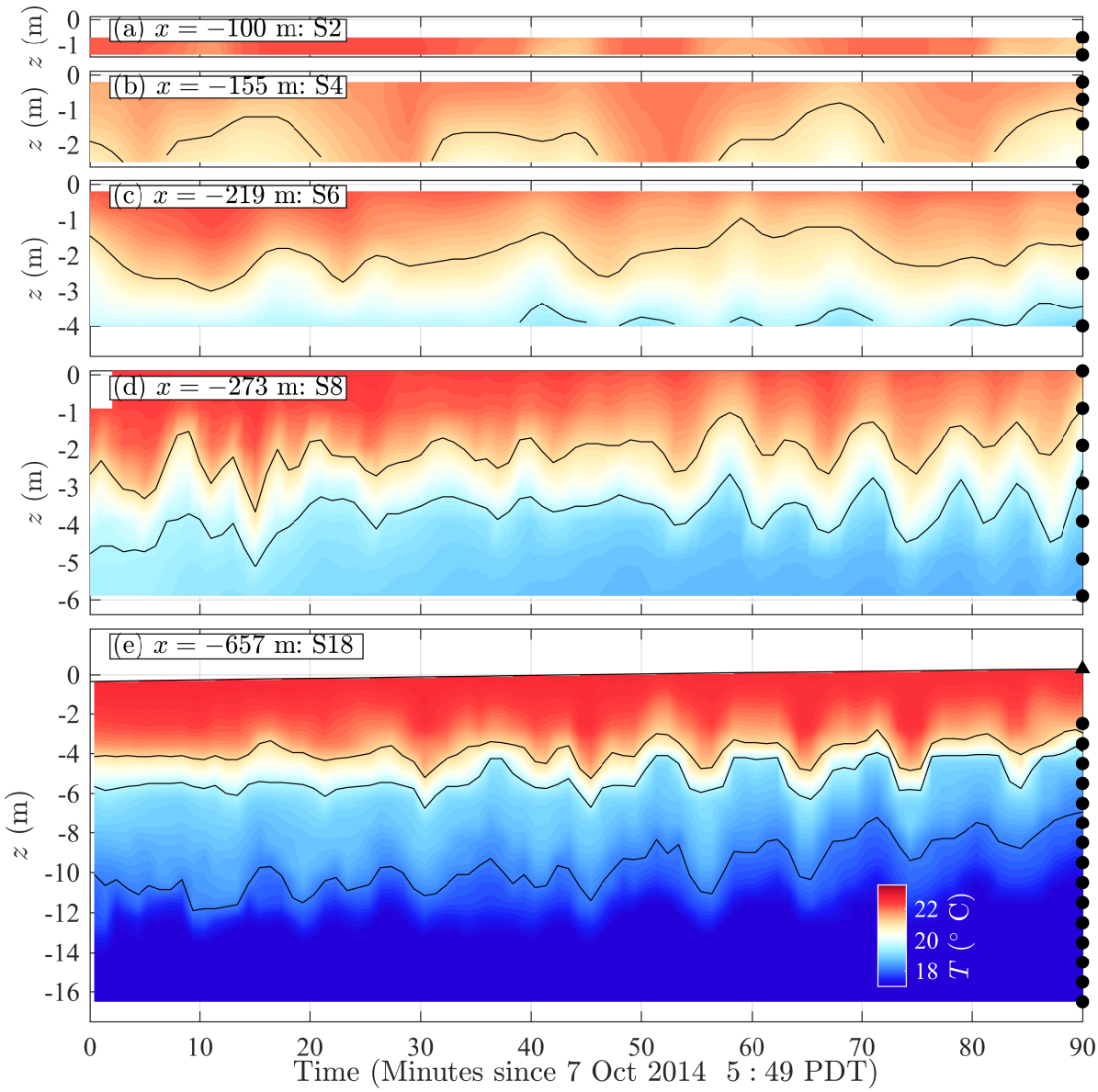

Figure 3.6: Similar to Figure 3.5, but with the time axes of all plots zoomed to highlight 1.5 hours beginning on 7 October 2014 at 5:49 PDT. The 18.1°C, 19.6°C and 21.1°C isotherms are highlighted with a black curve in all panels.

last 40 min (Figure 3.6d). Upslope at S6, variability at ≈ 10 min period is evident near the bottom (19.6°C isotherm), but mid-water depths ($z \approx -2$ m) contain variability at longer time scales (Figure 3.6c). The resulting variability of the 21.1 °C isotherm at S4 is predominantly at 20 min periods, with less high frequency variability than in deeper waters (compare Figures 3.6b and d).

The temperature observations (Figures 3.3–3.6) with large amplitude isotherm displacements relative to water depth, rapid temperature changes, and M4 harmonics demonstrate the presence of a rich NLIW field. Spectral properties of the NLIW field are explored focusing on the mid-water column temperature time-series from fast sampling SBE56 thermistors at $z = -9$ m at S18, and $z = -4$ m at S6 (Figure 3.7a,b). During the active period I (first 10 days), large (4–5 °C) temperature oscillations are present at both locations. The less active period II (days 10–30) still has NLIW activity, although the magnitude (1–2 °C) is much reduced. To contrast these two periods and locations, a seven day time-period is selected to represent period I (red and blue, Figure 3.7a,b) and period II (purple and green, Figure 3.7a,b). Temperature spectra of these four time series were calculated with the multi-taper method [Thomson, 1982] using the JLab toolbox [Lilly, 2016]. The 95% confidence interval (gray shading) is found from the χ^2_k distribution with the 14 degrees of freedom given by the orthogonal Slepian tapers.

Period I temperature spectra at S18 (red, Figure 3.7c) has peaks at M2 and M4 frequencies, and decays with frequency up to a broad secondary peak at 6–10 cph (7–10 min period), corresponding to high frequency variability at S18 in Figure 3.5. Farther upslope, the S6 temperature spectra does not have a clearly defined M2 peak and the S6 M2-band variance is 21% that of S18 (blue, Figure 3.7c). However, at S6 a clear and significant M4 peak is present that has essentially the same variance as at S18. The M4 peak indicates either M2 to M4 nonlinear energy transfers between S18 and S6 or M4 generation in deeper water, likely in the offshore canyons [Alberty et al., 2017]. An additional small S6 spectral peak is evident near M8 (harmonic of M4, 0.33 cph, 3-hour period) with nearly twice as much variance as at S18, suggesting nonlinear energy transfers from M4 to M8 between S18 and S6. The S6 spectra falls off similarly to S18,

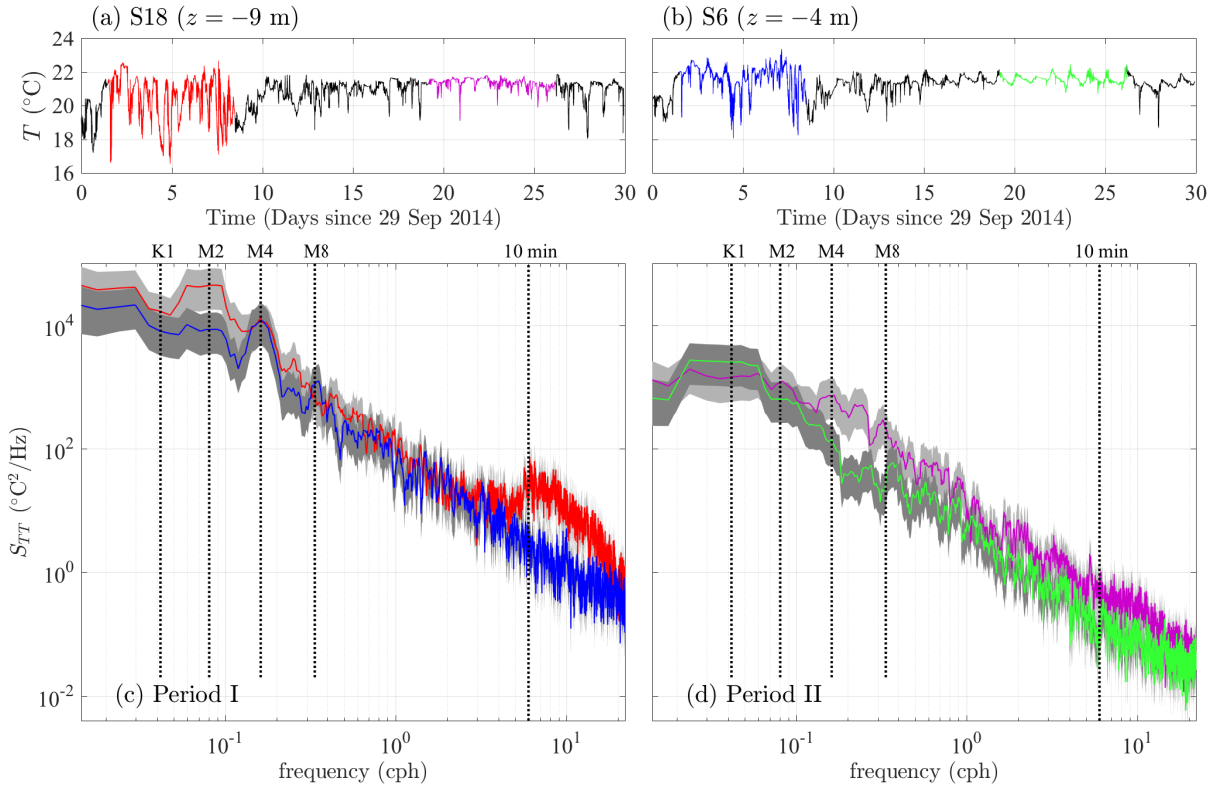

Figure 3.7: **Top panels:** Mid-water column temperature at (a) S18 (green star in Figure 3.1) at $z = -9$ m and (b) S6 at $z = -4$ m, versus time. Two 7-day periods containing contrasting internal wave conditions are highlighted at each location. Temperature during days 1.5 - 8.5 in the active period I is colored red (S18) and blue (S6); and temperature during days 19.2-26.2 in the less active period II is colored purple (S18) and green (S6). **Bottom panels:** Temperature spectra vs frequency at both S18 and S6 for (c) period I and (d) period II. Colors correspond to the highlighted periods in (a) and (b), and frequencies corresponding to the 24-hour (K1), 12-hour (M2), 6-hour (M4), 3-hour (M8) and 10 min periods are highlighted (vertical dotted). The 95% confidence interval for spectra at S18 and S6 are shaded light gray and dark gray, respectively.

but does not have the broad high-frequency spectral peak, consistent with the reduced onshore high frequency variability observed in Figure 3.5. Between S18 and S6, the M2 variability was coherent (≈ 0.78, above the 99% confidence level of 0.39) with 20 min phase lag, suggesting propagation albeit at an unknown angle. Between S18 and S6, M4 variability also was coherent (0.8), as was the M6 and M8 variability (at 0.6 and 0.5), albeit more weakly than M2 and M4. However, variability above 1 cph was not coherent between S18 and S6, similar to the zero lagged correlation of the 19.6 °C isotherm elevation between S18 and S8 in Figure 3.6.

The period II temperature spectra (Figure 3.7d) were reduced at all frequencies relative to period I. Spectral peaks at M2, M4 and higher harmonics are still present at S18 in period II (purple, Figure 3.7d), but spectral levels are reduced by a factor of 10 at these frequencies. Furthermore, the period I S18 elevated variability at > 1 cph is absent during period II. The period II diurnal temperature variability at S6 (green, Figure 3.7d) is slightly elevated relative to S18, consistent with increased solar heating and longwave cooling at the shallower S6 depth, and is coherent between S6 and S18. At M2 and higher frequencies, the S6 period II spectra has no significant peaks, was incoherent with S18, and had a total variance half that of S18.

3.5 Coherent Upslope Evolution of Individual Nonlinear Internal Wave Events

The NLIW field observed from S18 (18 m water depth) to near-shoreline S2 (Figures 3.3–3.6) contains cold pulses that propagate coherently upslope (e.g., Figure 3.5). The runup characteristics of these cold pulses ultimately determine the NLIW cross-shore extent and impact to the nearshore region, through for example, larval transport e.g., [Pineda, 1999]. Here, the coherent upslope evolution of individual NLIW events is explored in analogy to laboratory studies e.g., [Wallace and Wilkinson, 1988, Sutherland et al., 2013a]. Events are a significant and rapid reduction and recovery of temperature near the pier-end over a few hours, and are

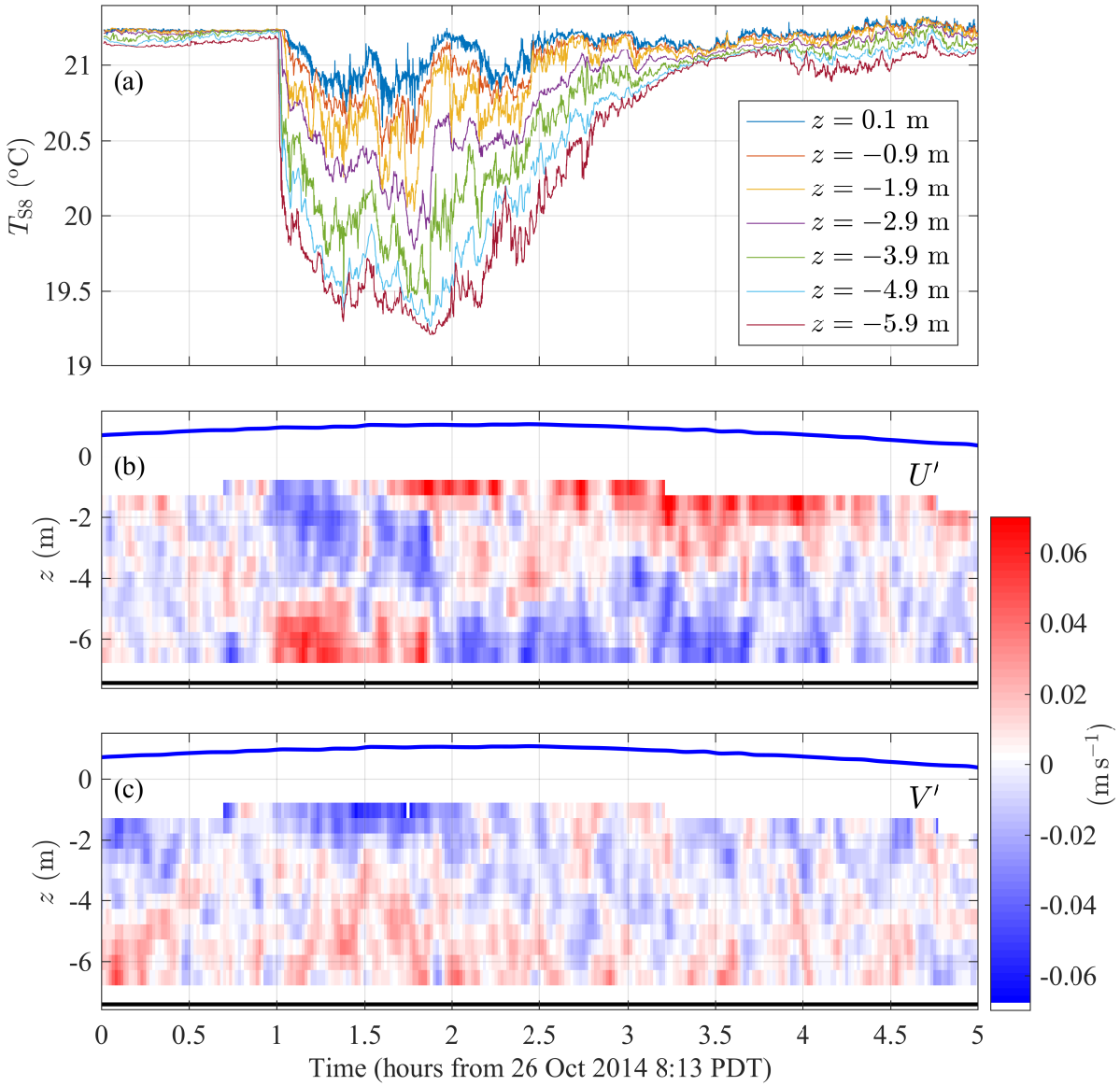

Figure 3.8: Five-hour time series of a NLIW runup event at S8 beginning at 8:13 am PDT on 26 October 2014: (a) S8 1 Hz temperature from near surface to near bed, (b) Cross-shore baroclinic current U' and (c) alongshore baroclinic current V' versus depth and time. In (b) and (c), the bed and mean tidal surface are indicated by the black and blue curves respectively.

defined quantitatively later. Detailed analysis is restricted to between S8 and just seaward of the surfzone at S2 where high thermistor density (Figure 3.1b) allowed for coherent upslope tracking of NLIW events. The time period is narrowed to 9–28 October (experiment days 11 to 30) when the S8 (pier-end) alongshore array (red dots, Figure 3.1a) was concurrently deployed. A single NLIW event is examined first to introduce important event parameters (e.g., event front speed c_f). Analysis is then broadened to multiple events at S8 and farther onshore, leading to scaling the upslope NLIW event evolution.

3.5.1 Example NLIW Event Characteristics

An example 5-h long NLIW event occurred on 26 October (red square, experiment day 28 bottom of Figure 3.3e) with large surface wave ($H_s \approx 1.2$ m) and moderate wind ($u_w \approx 3.5\ m\,s^{-1}$) conditions (Figure 3.2). This event is selected to highlight NLIW runup properties. Prior to the event front arrival at hour 1, S8 temperature was essentially constant near 21.2 °C and weakly stratified, $dT/dz < 0.01°C\,m^{-1}$ (Figure 3.8a). After the event front arrival, S8 near-bottom temperature fell rapidly ($\approx 1°C$ in 1 min) and the water column stratified ($dT/dz > 0.25°C\,m^{-1}$). Temperature fluctuations of $O(0.2\ °C)$ at 1–30 min time scales are observed throughout the water column. Near-bottom temperature began to increase after hour 2 ($\approx 0.025°C\,min^{-1}$), while temperature in the upper 3 m cooled slightly. The event concluded between hour 2.75 and 4 as the near-bed warmed and the near-surface cooled until the water column was again weakly stratified near hour 4. During this event, the coldest (bottom) S8 temperature was near 19.4°C (Figure 3.8a), but the coldest (bottom) S18 temperature before the event was near 20.7 °C (not shown). Thus, the coldest water at S8 during the event originated from a location deeper than 18 m and traveled horizontally upslope more than 384 m to reach S8.

Velocity associated with the upslope NLIW example event was observed by the ADCP at S8. Cross-shore (U) and alongshore (V) velocities are decomposed into (e.g., for U) depth-

averaged (barotropic) velocity $\overline{U}$ and is the depth-varying (baroclinic) velocity U', so that

$$U(z,t) = \overline{U}(t) + U'(z,t), \tag{3.1}$$

and the vertical average of U' is zero. The barotropic component is assumed to be irrotational in the experiment domain and slowly varying in time. This decomposition is partially aliased by the removal of velocity bins near the tidal sea-surface. Prior to the event onset, barotropic velocity magnitude was weak (< 0.05 m s^{-1}) as was baroclinic velocity magnitude (almost always $U' < 0.02$ m s^{-1}). However, after the abrupt temperature drop at hour 1 signaling the event arrival (Figure 3.8a), baroclinic velocity U' increased, with onshore velocity at depth exceeding 0.06 m s^{-1} and offshore velocity near the surface (Figure 3.8b). The baroclinic current was predominantly in the cross-shore (U') direction, with a weak alongshore (V') component (Figure 3.8c). Near hour 2, the direction of U' reverses, and thereafter the near-bed flow is offshore and the near-surface flow is onshore, coincident with the bottom temperature recovery (Figure 3.8a and b). During the recovery (2.75 h to 4 h), the transition depth between near-surface cooling and near-bed warming is $z \approx -3$ m (Figure 3.8a), which is also near the U' zero crossing depth.

The near-bottom upslope event temperature evolution (Figure 3.9) is key to determining event parameters. Prior to the event start at hour 1, the region from S8 to the shoreline was essentially homogeneous in T (Figure 3.9a). The pier-end near-bottom T was also largely uniform in the alongshore (Figure 3.9b). At each cross-shore and alongshore location, the event arrival is clearly visible as a steep drop in T (the event front) that propagates coherently in the alongshore and cross-shore. This T drop then slowly reaches a minimum before beginning to recover near hour 2. At S8, the overall temperature drop of about 2 °C was fairly uniform spanning 400 m in the alongshore (Figure 3.9b). In the cross-shore, the temperature drop is coherent and reduced onshore to $x = -137$ m (black curve in Figure 3.9a). Onshore of $x = -137$ m, neither a sharp nor

coherent temperature drop is observed (dashed curves in Figure 3.9a). By hour 4 the event is over and temperature has largely recovered to the pre-event value, albeit with occasional remnants of colder water upslope (e.g., yellow, magenta, and blue curves at hour 4.2 in Figure 3.9a).

The example event's upslope near-bottom temperature evolution (Figure 3.9) highlights key quantifiable event-front characteristics. The sharp temperature drop indicates the event front arrival time t_{f1}, defined as when the 3 minute averaged temperature change $\mathrm{d}T/\mathrm{d}t < -0.033\ ^{\circ}\mathrm{C\,min}^{-1}$ (gray dots Figure 3.9). Onshore ($+x$) NLIW event front propagation is evident from the progression of t_{f1} at different cross-shore locations (Figure 3.9a). Similarly, the alongshore event front arrivals (Figure 3.9b) indicate a south to north ($+y$) propagation component, consistent with the observed baroclinic velocities (positive near-bottom U' and weakly positive V' at event start, Figure 3.8b and c). At a particular cross-shore location, the event front passes at a time t_{f2} defined as where the 3-minute averaged $\mathrm{d}T/\mathrm{d}t > -0.0067\ ^{\circ}\mathrm{C\,min}^{-1}$ (open circles in Figure 3.9b). Time t_{f2} does not necessarily correspond to the coldest observed event temperature, but rather to when the sharp event front (rapid T drop) has passed the sensor. The temperature drop ΔT associated with the event front is then defined as

$$\Delta T = T(t_{\mathrm{f1}}) - T(t_{\mathrm{f2}}). \tag{3.2}$$

At S8, an event is defined to occur when $\Delta T > 0.3\ ^{\circ}\mathrm{C}$ over 9 minutes, and is defined to propagate farther upslope (onshore) as long as coherent $\Delta T > 0.15\ ^{\circ}\mathrm{C}$. For this example event, S8 $\Delta T = 1.26\ ^{\circ}\mathrm{C}$, but as the event propagated onshore the magnitude of the coherent event-front decreased to $\Delta T = 0.34\ ^{\circ}\mathrm{C}$ at $x = -137$ m (black curve in Figure 3.9a). As onshore-coherent $\Delta T > 0.15\ ^{\circ}\mathrm{C}$ was not observed onshore of $x = -137$ m (dotted lines, Figure 3.9a), the NLIW event runup cross-shore extent is defined as $x_{\mathrm{R}} = -137$ m.

Event front speed c_{f} and angle θ are calculated using the cross-shore and alongshore event arrival time and the observed barotropic velocity. The change in event front alongshore

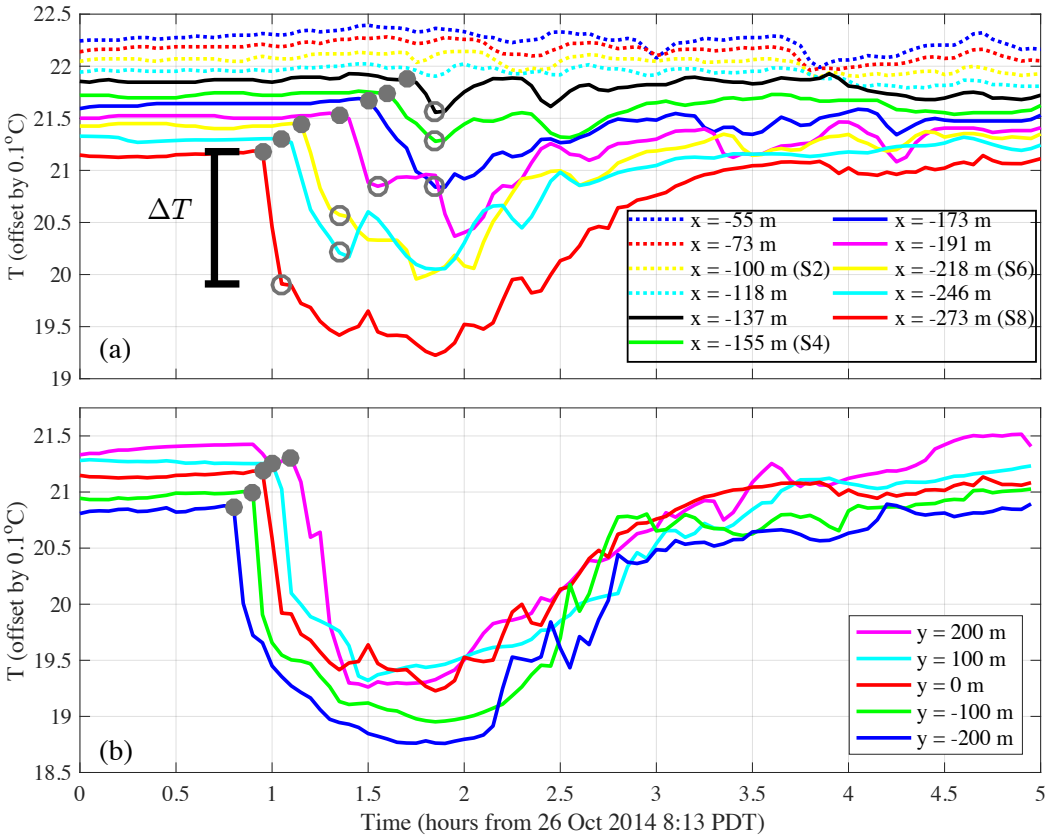

Figure 3.9: NLIW event example bottom temperature versus time beginning at 8:13 am PDT on 26 October 2014 for (a) the cross-shore locations and (b) the pier-end (S8) alongshore locations (red dots in Figure 3.1a), offset by 0.1°C in both (a) and (b) for visibility. Gray dots indicate the event arrival time at all locations. Open circles in (a) indicate the temperature change that defines ΔT, with S8 $\Delta T = 1.26$°C highlighted. The NLIW event ΔT was below the 0.15°C cutoff threshold onshore of the runup extent $x_R = -137$ m, indicated by the dotted lines in (a).

arrival position versus time $\mathrm{d}y_\mathrm{f}/\mathrm{d}t$ at S8 is estimated from the slope of the linear fit of alongshore front location y_f versus arrival time when $\Delta T > 0.3$ °C at three or more alongshore locations. Similarly, the S8 cross-shore change in position versus time, $\mathrm{d}x_\mathrm{f}/\mathrm{d}t$, is found from the arrival time difference between bottom sensors at S8 ($x = -273$ m) and $x = -246$ m. At S8, the event propagation angle estimated as

$$\theta = \arctan\left(\frac{\mathrm{d}x_\mathrm{f}/\mathrm{d}t}{\mathrm{d}y_\mathrm{f}/\mathrm{d}t}\right), \tag{3.3}$$

which is independent of the barotropic current. Although barotropic motions do not affect θ, they do affect c_f (in this case by approximately 30%). Accounting for barotropic motions, the event front speed is,

$$c_\mathrm{f} = \mathrm{d}x_\mathrm{f}/\mathrm{d}t\cos\theta - \overline{U}\cos\theta - \overline{V}\sin\theta. \tag{3.4}$$

For this example event, S8 front speed is $c_\mathrm{f} = 0.06\ \mathrm{m\,s^{-1}}$ and incidence angle is $\theta = 11.2°$.

Observations of ΔT and c_f can be related to idealized two-layer laboratory and numerical studies of NLIW runup with defined layer height (h_i) and layer density (ρ) difference $\Delta\rho$ e.g., [Sutherland et al., 2013a, Arthur and Fringer, 2014]. Here, the continuously stratified ocean is related to an idealized equivalent two-layer fluid with layer density difference $\Delta\rho = \alpha\Delta T$ (where α is the coefficient of thermal expansion) and the equivalent two-layer interface height set by equating the change in vertically integrated baroclinic potential energy PE associated with the continuously-stratified event front to the potential energy change of a two-layer system with $\Delta\rho$ and layer depth h_i. The instantaneous vertically integrated baroclinic potential energy is

$$\mathrm{PE}(t) = \int_0^{\tilde{h}} (\rho(z',t) - \rho_0) g z' \,\mathrm{d}z', \tag{3.5}$$

where ρ_0 is a constant reference density, g is gravity, the tidally varying water depth is $\tilde{h} = h + \eta$, and z' is a vertical coordinate referenced to the bed. The change in PE associated with the event

front is

$$\Delta \mathrm{PE} = \mathrm{PE}(t_{\mathrm{f}2}) - \mathrm{PE}(t_{\mathrm{f}1}). \tag{3.6}$$

For a two-layer system, the equivalent vertically integrated change in potential energy from $t_{\mathrm{f}1}$ to $t_{\mathrm{f}2}$ is

$$\Delta \mathrm{PE} = \Delta \rho g \frac{z_{\mathrm{IW}}^2}{2}, \tag{3.7}$$

where z_{IW} approximates h_i and is the equivalent two-layer interface height above the bed for the stratified event. Rearranging (3.7) gives z_{IW} as a function of ΔPE and $\Delta\rho$,

$$z_{\mathrm{IW}} = \left(\frac{2\Delta \mathrm{PE}}{\Delta \rho g} \right)^{\frac{1}{2}}. \tag{3.8}$$

The two-layer equivalent interface height is then found from (3.8) using the change in PE due to the event front in the continuously stratified ocean (3.6) and $\Delta\rho = \alpha \Delta T$. For the example event, the S8 interface height is $z_{\mathrm{IW}} = 2.48$ m, consistent with the large temperature drop in the bottom 2 m and weaker drop at shallower depths. Estimation of z_{IW} depends on adequate vertical temperature resolution, restricting z_{IW} calculation to cross-shore locations with at least four thermistors in the vertical (Figure 3.1b). Having defined key parameters associated with the NLIW event front (ΔT, c_{f}, z_{IW}, and x_{R}), the observed range and upslope (onshore) evolution of individual events are investigated next.

3.5.2 Individual NLIW Event Characteristics

Isolated individual NLIW events are defined when $\Delta T > 0.3$ °C at S8 and when no other cold pulses occur for ± 3 h. This second criterion removes overlapping events (discussed later). With these criteria, a total of 14 individual NLIW events with 0.3 °C $< \Delta T <$ 1.7 °C were isolated at the pier-end (S8) between 9 and 30 October. Two events had $\Delta T > 1.5$ °C, six events had 1.0 °C $< \Delta T <$ 1.5 °C, three events had 0.5 °C $< \Delta T <$ 1.0 °C and three events had

Table 3.1: Summary of example events A–D detailed in section 3.5. Left to right: Event designator, S8 significant wave height H_s, wind speed u_w, observed event front cross-shore propagation speed c_f, ratio of bottom baroclinic current to event propagation speed $|U_b'|/c_f$, propagation angle θ, event front temperature difference ΔT_0, equivalent two-layer height z_{IW0}, best-fit deceleration d_f and standard error, and total runup distance from x_0, Δx_R.

Event	H_s (m)	u_w ($m\,s^{-1}$)	c_f ($cm\,s^{-1}$)	$\lvert U_b'\rvert/c_f$	θ (°)	ΔT_0 (°C)	z_{IW0} (m)	d_f ($\times 10^{-5}\ m\,s^{-2}$)	Δx_R (m)
A	0.32	1.02	3.8	0.8	2.9	1.29	2.32	1.3 ±0.2	128
B	0.69	0.48	3.6	1.2	1.0	0.96	2.10	0.9 ±0.4	100
C	1.20	3.36	6.0	0.7	11.2	1.26	2.48	1.3 ±0.4	137
D	1.03	2.49	7.4	0.4	3.6	1.62	2.12	2.4 ±0.5	128

$0.3\ °C < \Delta T < 0.5\ °C$ (left column, Figure 3.10). All fourteen events were observed coherently propagating upslope with reduced ΔT so that 54 m farther onshore (at S6) only 10 events were observed, all with $\Delta T > 0.3\ °C$ (second column, Figure 3.10). Despite the onshore reduction in ΔT, six events (associated with the largest ΔT at S8) were still observed at S4 (right column, Figure 3.10). Farther upslope ΔT continued to decrease, but at S2 no coherent $\Delta T > 0.15\ °C$ was observed.

At S8, the fourteen events propagated upslope with speeds $1.4\ cm\,s^{-1} < c_f < 7.4\ cm\,s^{-1}$ (radial magnitude, Figure 3.11a). These NLIW events also propagated with a range of incidence angles ($-5° < \theta < 23°$, Figure 3.11a) potentially due to the many internal wave generation locations nearby. The slight positive mean $\theta \approx 5°$, indicates a south to north NLIW propagation tendency, suggesting a possible dominant source near the southern La Jolla canyon (Figure 3.1a) through mechanisms described in [Alberty et al., 2017]. During the example event (Figure 3.8), the inferred large upslope transport of cold water suggests the event is strongly nonlinear. At S8, event nonlinearity is quantified with the ratio of near-bed baroclinic velocity magnitude $|U_b'|$ to front speed c_f, ($|U_b'|/c_f$), where $|U_b'|$ is averaged for 10 minutes between 0.9 m and 1.9 m above the bottom after event onset. For linear internal waves $|U_b'|/c_f \ll 1$. At S8, the example event detailed in section 3.5.1 has $|U_b'|/c_f = 0.7$ indicating strong nonlinearity. The fourteen isolated NLIW events had $|U_b'|/c_f$ between 0.3 and 2.0 with a mean value of 0.7.

For these 14 NLIW events, the observed S8 c_f is compared to two-layer gravity current

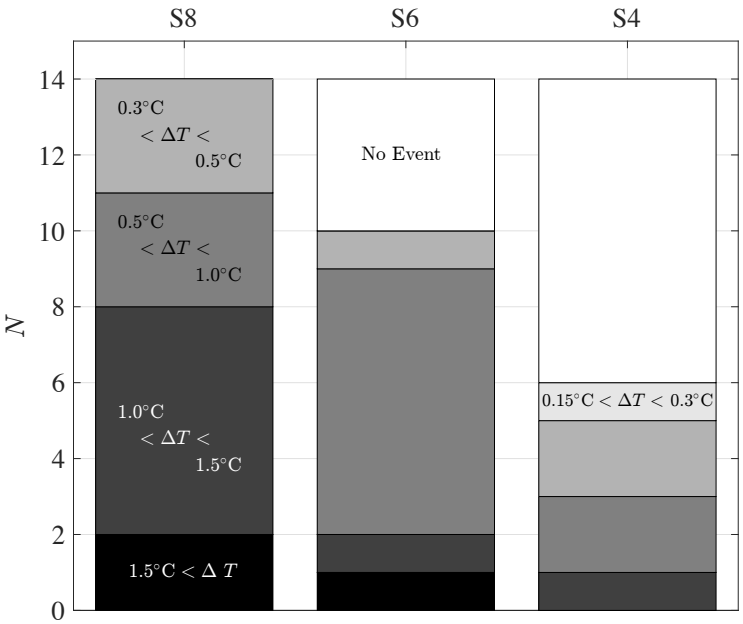

Figure 3.10: Number (N) and ΔT distribution (shading) of NLIW events observed between 9 and 30 October 2014 at cross-shore locations S8, S6 and S4 (highlighted in Figure 3.1b). Of the $N = 14$ events observed at S8, only six were observed at S4, and none with $\Delta T > 1.5$°C.

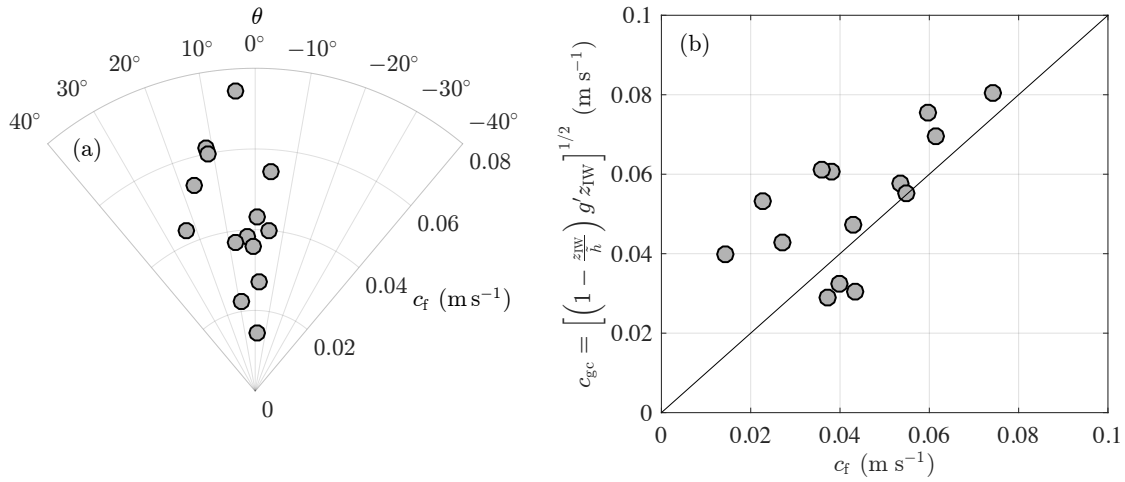

Figure 3.11: (a) NLIW event front speed c_f (radial direction) and incident angle θ at S8 for the 14 observed events between 9 and 30 October 2014. Events are plotted as if a viewer were looking offshore from the end of the SIO pier. (b) NLIW two-layer gravity current front speed c_{gc} (3.10) versus event front speed c_f (3.4) for the 14 NLIW events observed at S8. The root-mean-square error is 0.016 m s^{-1}, squared correlation $R^2 = 0.44$, and the best-fit slope is 1.15.

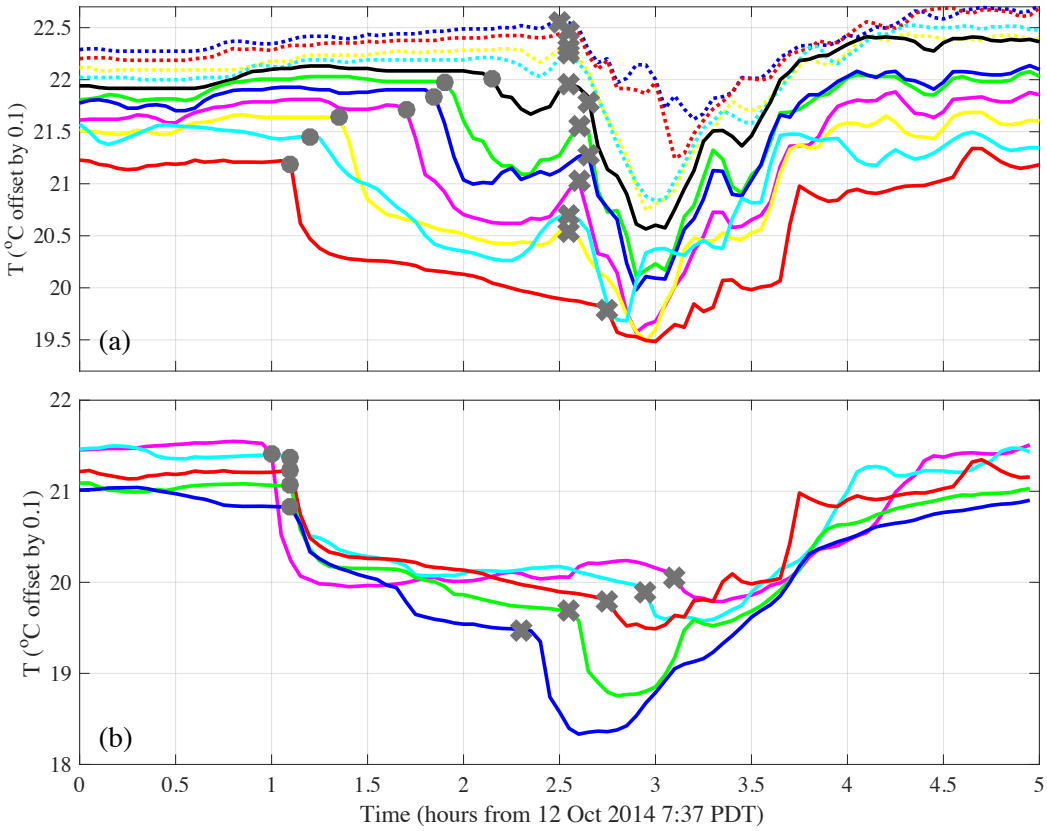

Figure 3.12: Bottom temperature versus time beginning at 7:37 on 12 October 2014 for (a) cross-shore locations and (b) alongshore locations (as in Figure 3.9) offset by 0.1°C for visibility. Gray dots indicate the arrival of a NLIW cold pulse propagating with nearly zero angle onshore to $x_R = -137$ m. Gray crosses indicate a second NLIW pulse superimposed on the first, propagating at high angle from south to north. The first NLIW event ΔT was below the 0.15°C cutoff threshold onshore of the runup extent $x_R = -137$ m, indicated by the dotted lines in (a), though the second pulse caused significant (≈ 0.8°C) temperature reduction in water as shallow as 1 m ($x = -55$ m).

speeds e.g., [Sutherland et al., 2013a, Marleau et al., 2014]. A flat-bottom two-layer fluid with interface height h_i in depth h and upper and lower layer densities ρ_0 and $\rho_0 + \Delta\rho$, respectively has reduced gravity $g' = g(\Delta\rho)/\rho_0$. The corresponding gravity current Froude number is [Shin et al., 2004]

$$F_0 = \sqrt{\delta(1-\delta)}, \tag{3.9}$$

where $\delta = h_i/h$. The speed of the gravity current front is

$$c_{\mathrm{gc}} = F_0(g'h)^{1/2} = \left[(1-\delta)g'h_i\right]^{1/2} \approx \left[\left(1 - \frac{z_{\mathrm{IW}}}{\tilde{h}}\right) g' z_{\mathrm{IW}}\right]^{1/2}, \tag{3.10}$$

where, for a NLIW event, z_{IW} is used for the lower layer height, $\tilde{h}$ is the tidally adjusted water depth, and $\Delta\rho$ is given by $\alpha\Delta T$.

For these 14 NLIW events, the observed S8 upslope event front speed c_{f} is reasonably well predicted by the two-layer gravity current speed c_{gc} (3.10) with root mean squared (rms) error of $0.016\ \mathrm{m\,s^{-1}}$, squared correlation $R^2 = 0.44$ and best-fit slope of 1.15 (Figure 3.11b). Although c_{gc} is biased high relative to c_{f}, this bias could be accounted for by adjusting the F_0 definition (3.9). The reasonably good relationship between c_{f} and c_{gc} indicates that these continuously stratified NLIW events (e.g., Figure 3.8) are reasonably well scaled as a two-layer gravity current e.g., [Shin et al., 2004], even though the events propagate at non-zero incidence angles, the bottom slopes weakly, and the event may be propagating into inhomogeneous (stratified) water.

Not all NLIW occurrences are as simple as the example event (Figures 3.8 and 3.9) with its clearly defined parameters (e.g., t_{f1}, ΔT and z_{IW}). NLIW runup can be complicated, with overlapping cold pulses containing differing c_{f} and θ (Figure 3.12). A near simultaneous initial cold pulse arrival at S8 alongshore locations (gray dots, Figure 3.12b) indicates a NLIW pulse with $\theta = 2.2^\circ$ which propagates onshore (subsequent gray dots, Figure 3.12a). A second cold pulse is observed roughly 1.2 h later at S8 cross-shore and alongshore stations (gray crosses, Figure 3.12a,b) superimposed on the first pulse. The second pulse was observed within the

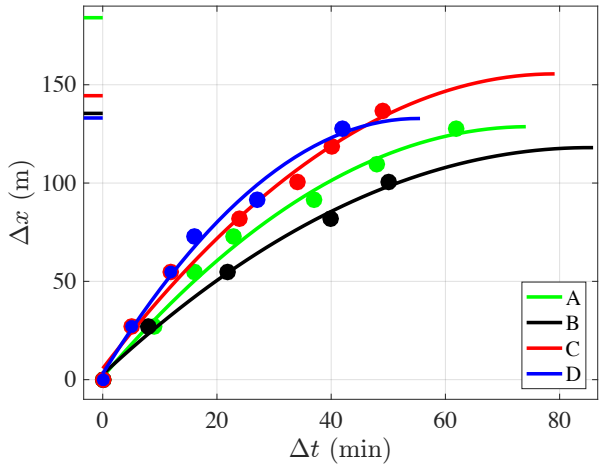

Figure 3.13: NLIW event A-D front propagation distance Δx versus elapsed time Δt (colored dots) and quadratic fit (curves) as in (3.11). There is good agreement (squared correlation > 0.98) between the quadratic fit and observations. For each event, the estimated surfzone boundary location $x_{sz} - x_0$ is indicated as a bar on the ordinate.

surfzone (at this time surfzone wave breaking begins at $h = 2$ m) and propagated south to north at very high angle and with ΔT decreasing in the alongshore ($\Delta T = 1.08$ °C at $y = -200$ m but $\Delta T = 0.17$ °C at $y = 200$ m). Though the onset of the second pulse is cross-shore coherent, the temperature drop was observed nearly simultaneously at $x = -55$ m, $y = 0$ m and $x = -273$ m, $y = -200$ m (gray crosses in Figure 3.12a) before giving a sense of rapid offshore propagation as temperature recovered between hours 3 and 4. Although speculative, this pulse may have swept cold water into the surfzone at $y < 0$ m which was then reflected offshore. The second cold pulse propagated through the previously conditioned stratification and current. The criterion requiring isolated events removes such complicated overlapping cases (Figure 3.12) where event parameters are difficult to isolate.

3.5.3 Upslope NLIW Evolution

At S8, 14 isolated NLIW events have $\Delta T > 0.3$ °C with no overlapping cold pulses. To compare these NLIW events with idealized two-layer laboratory and modeling studies, the event propagation angle is restricted to be nearly shore-normal ($|\theta| < 15°$, eliminating 2 events).

A further restriction requires the wavefront to be roughly alongshore uniform, where ΔT is within 0.5 °C at four or more alongshore locations (eliminating 8 more events). Background barotropic velocity was weak during each event ($|\overline{U}| < 1.3$ cm s^{-1}). These restrictions result in four remaining events (colored markers in Figures 3.3e) denoted events A–D that are near normally incident and propagate into homogeneous conditions. Thus, these representative events are more consistent with a two-layer assumption than the total 14 isolated NLIW events at S8. To relate to laboratory two-layer internal runup and gravity current studies, these four events are further required to propagate into homogeneous T at and onshore of an initial cross-shore location x_0. Events B and C had homogeneous T at and onshore of S8 prior to the event, and thus the initial cross-shore location $x_0 = x_{S8} = -273$ m. Events A and D had some vertical stratification at S8 prior to the event start. However, just 27 m onshore T was vertically and onshore homogeneous, so $x_0 = -246$ m for events A and D to insure pre-event homogeneous conditions. Note, the example event in Figures 3.8 and 3.9 is event C. The upslope (onshore) evolution of events A–D (colored dots, Figures 3.3e) are explored in detail to highlight NLIW runup characteristics.

The onshore propagation distance from x_0 is $\Delta x = x - x_0$ and elapsed time from front arrival at x_0 is $\Delta t = t - t_{f1}(x_0)$. Event A–D fronts propagated onshore and slowed down until reaching their eventual total runup distance $\Delta x_R = x_R - x_0$ (dots, Figure 3.13). The upslope transit time was between 42–64 min with Δx_R varying between 100-137 m. The two-layer gravity current speed (3.10) can be expressed as dx/dt and the differential equation can be solved for change in cross-shore position x assuming a constant Froude number (3.9) and a constantly sloping bottom. The solution is a quadratic relationship between Δx and Δt, consistent with laboratory observations of broken internal solitary wave upslope runup e.g., [Sutherland et al., 2013a]. So, for each event, the front position Δx and elapsed time Δt are fit to a quadratic

$$\Delta x = -\frac{d_f}{2}(\Delta t)^2 + c_{f0}\Delta t, \tag{3.11}$$

with best-fit NLIW front speed at x_0 (c_{f0}) and constant onshore NLIW deceleration d_f. The fits all have high skill (> 0.98, lines Figure 3.13) with standard error in best-fit parameters found from standard methods e.g., [Wunsch, 1996]. The NLIW deceleration d_f varies between $(0.9-2.4)\times 10^{-5}$ m s^{-2} with standard error around 0.37×10^{-5} m s^{-2} (Table 3.1). Event D had the highest c_{f0} (7.84 $\pm$0.6 cm s^{-1}), but also had the largest deceleration, limiting the runup distance from x_0, $\Delta x_R = x_R - x_0$ to 128 m (blue, Figure 3.13). Event A decelerated less than event D, but had a smaller c_{f0} (5.86 $\pm$0.4 cm s^{-1}) resulting in a similar Δx_R. Event C had high c_{f0} (6.31 $\pm$0.6 cm s^{-1}) and also less deceleration than event D, allowing $\Delta x_R = 137$ m (red, Figure 3.13). Event B had the lowest c_{f0} (4.51 $\pm$0.6 cm s^{-1}) and deceleration, with observed $\Delta x_R = 100$ m.

None of these 4 events were observed to propagate coherently into the surfzone (tick marks along ordinate axis in Figure 3.13). During event A, the significant wave height was very small ($H_s = 0.32$ m, Table 3.1) and the surfzone was narrow. The event runup halted 56 m offshore of the estimated surfzone boundary (green tick mark, Figure 3.13). Event B with $H_s = 0.69$ m also halted more than 35 m from the estimated surfzone boundary. Events C and D had $H_s > 1$ m (Table 3.1) and with the wider surfzone, the total runup distance Δx_R was observed to within 10 m of the estimated surfzone boundary. Events C and D both caused thermistors inside the surfzone to cool ≈ 0.1°C in six minutes, though this cooling was insufficient to coherently track further onshore as an event ΔT.

NLIW event front temperature drop ΔT and equivalent two-layer height z_{IW} generally decreases farther upslope (Figure 3.14a,b). For events A–D, ΔT at x_0 (ΔT_0) varied between 0.96°C and 1.62°C (Figure 3.14a), a factor of 1.7. Upslope ΔT decreases differently amongst events, either rapidly (event B, black in Figure 3.14a) or slowly (event A, green). For events B–D, $\Delta T < 0.41$°C at x_R. In contrast, the slowly decaying event A had $\Delta T = 0.96$°C at x_R. Yet, for event A, no significant temperature drop was present 20 m onshore of x_R. The z_{IW} at x_0 (z_{IW_0}) varied between 2.1 m and 2.5 m (Figure 3.14b), a much smaller range than for ΔT_0. Upslope

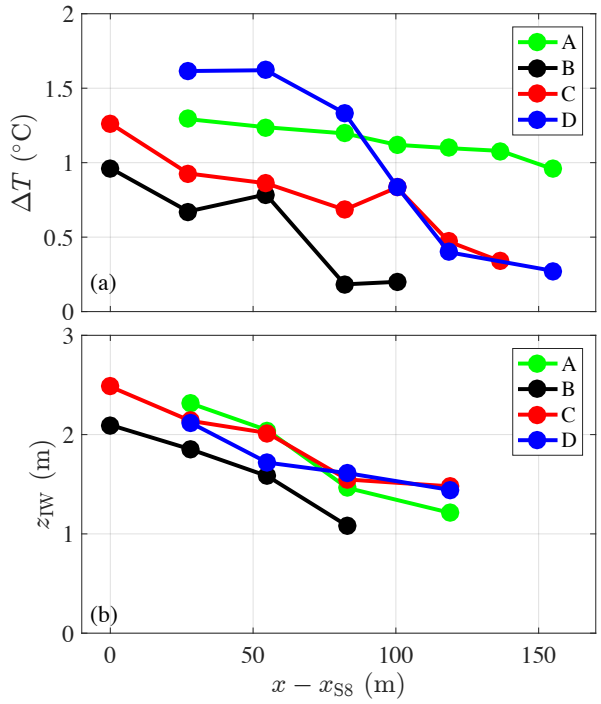

Figure 3.14: NLIW event A-D (colored) (a) ΔT and (b) equivalent two layer interface amplitude z_{IW} vs upslope distance relative to S8 ($x - x_{S8}$). Note, z_{IW} is only estimated at locations with at least four thermistors in the vertical. Events A and D are first estimated at $x - x_{S8} = 27$ m as S8 was pre-stratified.

from x_0, z_{IW} reduced linearly in a relatively similar manner for all events, in contrast to ΔT. At x_R, z_{IW} ranges between 1–1.5 m, still significant compared to z_{IW_0}. For events A–D, the upslope reduction in dimensional c_f, z_{IW}, and ΔT and the constant deceleration are qualitatively consistent with laboratory observations of internal runup of broken internal solitary waves [Wallace and Wilkinson, 1988, Helfrich, 1992, Sutherland et al., 2013a].

3.5.4 Scaling upslope NLIW evolution

The stratified NLIW events A–D have baroclinic velocity structure and temperature structure that are qualitatively consistent with an upslope two-layer gravity current (e.g., Figures 3.8 and 3.9). Events A–D have $|U_b'|/c_f$ that is $O(1)$ (Table 3.1), also consistent with a gravity current. NLIW events A–D have constant deceleration (Figure 3.13) and their density anomaly

(ΔT) and height (z_{IW}) are reduced onshore consistent with upslope two-layer gravity currents [Marleau et al., 2014]. Here, the NLIW event parameters (c_{f0}, d_{f}, Δx_{R}, ΔT and z_{IW}) are scaled and compared to gravity current scalings.

The non-dimensional $\Delta T/\Delta T_0$ and $z_{\mathrm{IW}}/z_{\mathrm{IW}_0}$ dependence upon non-dimensional runup distance $\Delta x/\Delta x_{\mathrm{R}}$ is examined in analogy with laboratory studies of the upslope propagation of broken internal solitary waves e.g., [Wallace and Wilkinson, 1988, Helfrich, 1992]. Upslope event front temperature drop ΔT varied substantially (Figure 3.14a). However, the normalized $\Delta T/\Delta T_0$ largely collapse as a linearly decaying function of $\Delta x/\Delta x_{\mathrm{R}}$ (Figure 3.15a) with best-fit slope -0.61 and squared correlation $R^2 = 0.58$. For events A–D, the dimensional z_{IW} upslope dependence was not as scattered as for ΔT (Figure 3.14b). Similarly, the non-dimensional $z_{\mathrm{IW}}/z_{\mathrm{IW}_0}$ collapse very well as a linearly decaying function of $\Delta x/\Delta x_{\mathrm{R}}$ (Figure 3.15b) with best fit slope of -0.56 and $R^2 = 0.89$, again qualitatively consistent with laboratory studies [Wallace and Wilkinson, 1988, Helfrich, 1992, Marleau et al., 2014]. The collapse of non-dimensional ΔT and z_{IW} suggests the dynamics of the continuously stratified internal runup into homogeneous water is largely self-similar.

Laboratory two-layer upslope gravity current deceleration is constant and depends upon g', constant bed slope s, and the ratio h_i/h where h_i represents gravity current height and h is the total water depth [Marleau et al., 2014]. Adapting this scaling for continuously stratified NLIW event deceleration results in,

$$d_{\mathrm{gc}} = \frac{1}{2} g'_0 s \frac{z_{\mathrm{IW}_0}}{\tilde{h}_0} \left(1 - \frac{z_{\mathrm{IW}_0}}{\tilde{h}_0}\right), \tag{3.12}$$

where g'_0, z_{IW_0}, and $\tilde{h}_0$ are all at evaluated at x_0. Here, the averaged bedslope from S8 to S4 is used ($s = 0.033$). The events A–D best-fit front speed at x_0 (c_{f0}) and the constant deceleration d_{f} (3.11) are compared to the two-layer gravity current scalings for speed c_{gc} (3.10) and upslope deceleration d_{gc} (3.12). The events A–D c_{f0} varies from 0.04–0.08 $\mathrm{m\,s^{-1}}$ and are similar to the

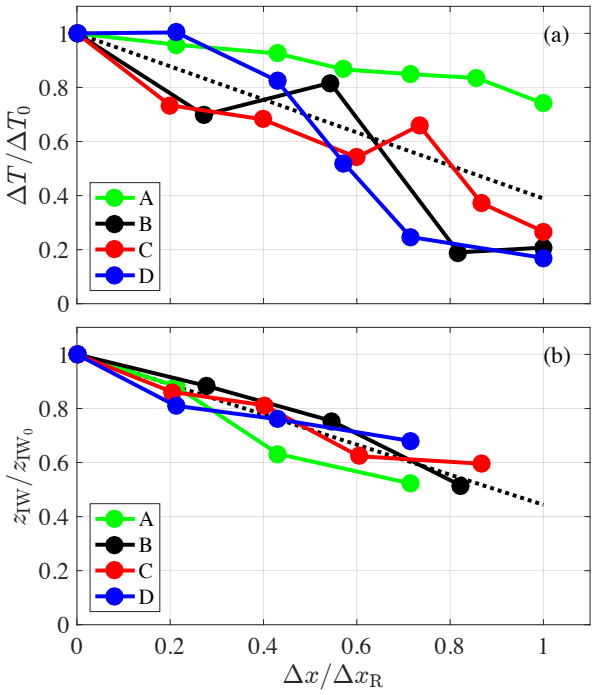

Figure 3.15: NLIW event A-D (colored) (a) normalized temperature anomaly $\Delta T/\Delta T_0$ and (b) normalized z_{IW}/z_{IW_0} versus normalized upslope propagation distance $\Delta x/\Delta x_R$. The linear fit (dotted black) to events A-D in (a) has squared correlation $R^2 = 0.58$. The linear fit to all events in (b) has slope -0.56 (dotted black) and $R^2 = 0.89$. Note, z_{IW} is only estimated at locations with four thermistors in the vertical.

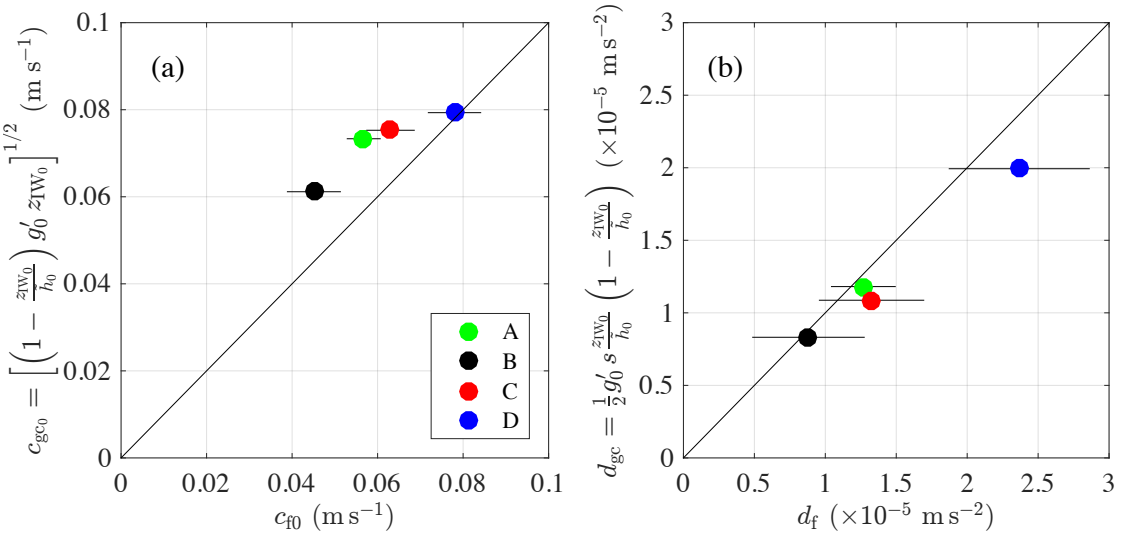

Figure 3.16: (a) The best-fit gravity current speed c_{gc0} (3.10) versus NLIW front speed c_{f0} (3.11) at x_0 with rms error of 0.013 m s^{-1} and best-fit slope 1.17. (b) Best-fit upslope gravity current deceleration d_{gc} (3.12) versus NLIW front deceleration d_f (3.11) with rms error of 0.2×10^{-5} m s^{-2} and best-fit slope of 0.84 Both (a) and (b) are for events A-D. Horizontal black bars are the standard error in the best-fit values.

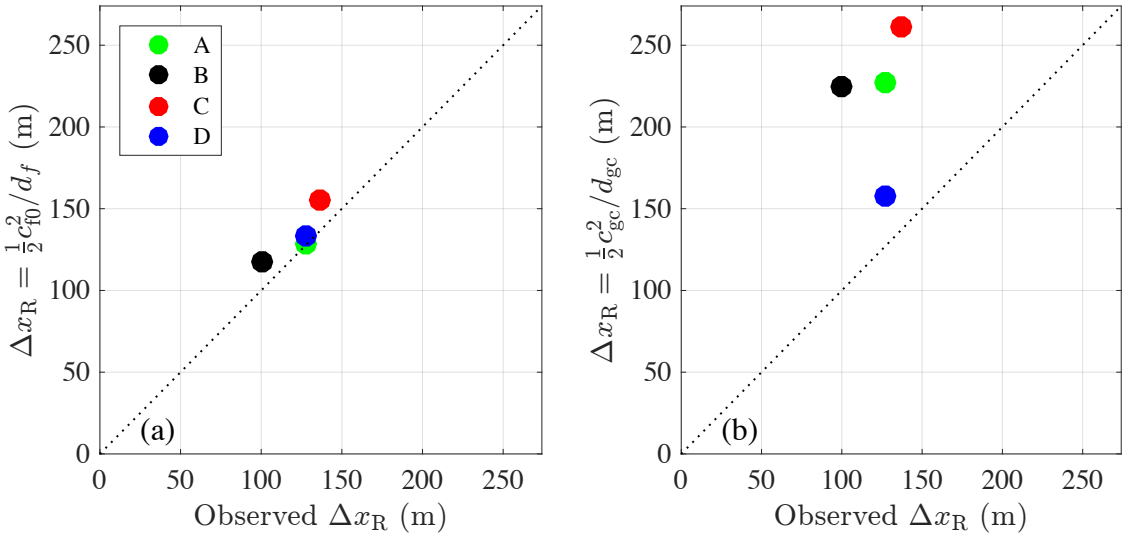

Figure 3.17: Predicted NLIW event A-D (colored) propagation distance Δx_R versus observed Δx_R using (a) best fit front velocity c_{f0} at x_0 and deceleration d_f, and (b) two-layer gravity current velocity c_{gc} and deceleration d_{gc}. The rms error is (a) 13 m and (b) 102 m.

two-layer gravity current speed c_{gc} estimated at x_0 (Figure 3.16a), although c_{gc} is generally larger than c_{f0} by more than a standard error (horizontal lines in Figure 3.16a). The c_{f0} and c_{gc} fit has rms error of 0.013 $\mathrm{m\,s^{-1}}$ and best-fit slope of 1.17. Events A–D d_f is very similar to d_{gc} (always within a standard error) over a large range (factor 2.5) of deceleration (Figure 3.16b). The d_f and d_{gc} fit has rms error of 9×10^{-7} $\mathrm{m\,s^{-2}}$ and best-fit slope of 0.84. The factor 2.5 variation in d_f is largely due to the ΔT_0 variations impacting g'_0. The small error of the c_{f0} and d_f scalings indicates that for normally-incident NLIW events propagating upslope into a homogeneous fluid, the two-layer gravity current scalings are appropriate.

Because both non-dimensional ΔT and z_{IW} are largely self-similar with $\Delta x/\Delta x_R$, the upslope evolution of an offshore (at x_0) observed NLIW runup event can be estimated knowing the total runup distance Δx_R. At the onshore runup limit (Δx_R), the event front speed $c_f = \mathrm{d}x_f/\mathrm{d}t = 0$. With the quadratic front evolution, setting the derivative of (3.11) to zero and substituting yields,

$$\Delta x_R = \frac{1}{2}\frac{c_{f0}^2}{d_f}. \tag{3.13}$$

The Δx_R estimated from (3.13) with c_{f0} and d_f reproduces the observed Δx_R defined in section 3.5.1 well (Figure 3.17a), with rms error of 13 m (less than the 18 m cross-shore resolution of the thermistor array, Figure 3.1b) and a best-fit slope of 0.92 that is near-unity. This demonstrates that with knowledge of offshore event front parameters (c_{f0}, d_f, ΔT_0, and z_{IW_0}) the upslope distribution of these parameters can be well estimated.

However, event front observations from at least three locations along the axis of propagation are required to estimate c_{f0} and d_f and thus Δx_R via (3.13). The gravity current scalings for c_{gc} (3.10) and d_{gc} (3.12) only require vertical temperature coverage at a single location, and can be used to estimate

$$\Delta x_R = \frac{1}{2}\frac{c_{gc}^2}{d_{gc}}. \tag{3.14}$$

The gravity current scaling based Δx_R (3.14) significantly overpredicts the observed Δx_R (Fig-

ure 3.17b), with rms error of 102 m and best-fit slope of 1.75. Relatively small error in $c_{\rm gc}$ and $d_{\rm gc}$ (Figure 3.16) cascade through (3.14) to generate these large errors. For example, with the best-fit slopes for $c_{\rm gc}$ (1.17) and $d_{\rm gc}$ (0.84) and the scaling (3.14), the predicted best-fit slope is 1.63, which is near the observed best-fit slope of 1.75 (Figure 3.17b). This demonstrates that predictions of total runup distance $\Delta x_{\rm R}$ are very sensitive to small errors in runup speed and deceleration.

3.6 Discussion

3.6.1 Internal runup and comparison to laboratory and numerical studies

For the 14 events at S8, the event front speed is consistent with a internal gravity current (Figure 3.11b) and the ratio $|U_b'|/c_{\rm f}$ is generally $O(1)$, suggesting that these events are internal bores e.g., [Pineda, 1994, Moum et al., 2007, Walter et al., 2012, Nam and Send, 2011]. For the four isolated (A–D) events, the ratio $|U_b'|/c_{\rm f}$ is also $O(1)$ (Table 3.1) and the upslope event evolution (speed and constant deceleration) is consistent both with upslope gravity currents [Marleau et al., 2014] and internal runup of laboratory broken internal solitary waves [Helfrich, 1992, Sutherland et al., 2013a]. This all indicates that the internal wave breaking begins well offshore of S8 and that S8 and onshore locations are located within the internal swashzone where events propagate as bores, similar to the swashzone of a beach e.g., [Fiedler et al., 2015].

In a tidal estuary with a planar "internal beach", [Bourgault et al., 2007] observed cross-shore propagating and dissipating internal solitary waves of elevation from 25 m to 10 m depth. In this dissipating region, the wave speed decreased linearly in the cross-shore, ($dc_{\rm f}/dx$ was constant). For the quadratic event front position (11), the event front speed as a function of x can be written as

$$c_{\rm f}(x) = c_{\rm f0}\left(1 - \frac{2d_{\rm f}\Delta x}{c_{\rm f0}^2}\right)^{1/2} \tag{3.15}$$

which yields an approximately constant dc_f/dx for small $2d_f\Delta x/c_{f0}^2$. For the best-fit parameters, the event front dc_f/dx is approximately constant for about half of Δx_R. Thus, the upslope evolution of the internal runup front speed is consistent with that of dissipating internal solitary waves [Bourgault et al., 2007]. However, the [Bourgault et al., 2007] waves speeds were between 0.2–0.5 $m\,s^{-1}$, much faster than observed here due to the much stronger density gradients of the estuary setting than observed near the SIO pier.

The evolution of these continuously stratified dense bores propagating upslope into homogeneous fluid are consistent with two-layer upslope gravity current scalings (e.g., Figure 3.16) using near-bed estimated ΔT and an interface height z_{IW} assuming equivalent potential energy (3.5–3.8). From flat-bottom numerical simulations, a continuously stratified interface between upper and lower layers results in a weak decrease, relative to two-layer theory (3.10), of the gravity current speed c_{gc} [White and Helfrich, 2014]. With stratification similar to that observed in events A-D, the continuously stratified model suggests the c_{gc} found from (3.10) should be reduced by $\approx 5\%$ [White and Helfrich, 2014]. This indicates that applying the two-layer approximation to these continuously stratified internal runup events is appropriate and also may account for some of the c_{gc} bias error (Figure 3.11b).

The constant upslope two-layer gravity current deceleration can be derived by assuming a weak slope such that at all locations the front speed follows the [Shin et al., 2004] gravity current speed (3.10) with constant Froude number F_0 that depends on $\delta = z_{IW}/h$ [Sutherland et al., 2013b, Marleau et al., 2014]. The quadratic in time dependence of the front position is derived with $h(x) = -sx$. This requires that z_{IW}/h be constant upslope. For the four isolated events A–D, $z_{IW}/h \approx 0.3$ at $\Delta x/\Delta x_R = 0$ and doesn't vary by more than ± 0.1 all the way to $\Delta x/\Delta x_R = 1$ (Figure 3.18). The linear upslope reduction in z_{IW}/z_{IW_0} with $\Delta x/\Delta x_R$ is qualitatively consistent with the observed linear upslope amplitude decay of a dissipating internal solitary wave on a linear slope [Bourgault et al., 2007]. Linear upslope z_{IW}/z_{IW_0} reduction is also consistent with laboratory internal solitary wave runup for all incident wave amplitudes [Wallace and Wilkinson,

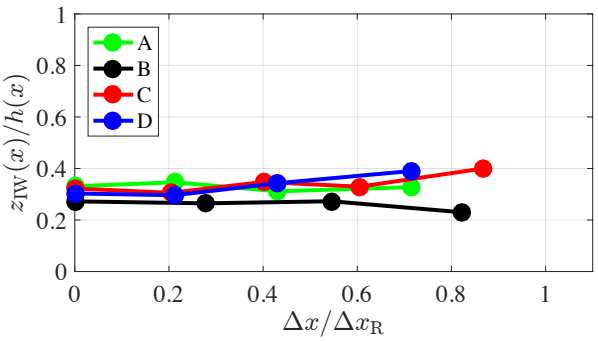

Figure 3.18: NLIW event A-D (colored) normalized z_{IW}/h versus upslope propagation distance $\Delta x/\Delta x_{\mathrm{R}}$.

1988, Helfrich, 1992], and with laboratory observations of a two-layer upslope gravity current on shallow slopes [Marleau et al., 2014]. This all supports the assumption that such internal bores are self-similar [Wallace and Wilkinson, 1988]. Note, however, that in laboratory internal solitary wave experiments, the origin ($\Delta x = 0$) is the location where solitary wave breaking is initiated (breakpoint), which would be offshore of S8 and unlike two layer systems, here ΔT is not constant in the upslope direction resulting in g' variations.

The observed linearly-decaying self-similar $\Delta T/\Delta T_0$ decrease with $\Delta x/\Delta x_{\mathrm{R}}$ is also qualitatively consistent with two-layer laboratory upslope normalized density decay [Wallace and Wilkinson, 1988], although again the origin is relative to the internal solitary wave breakpoint. The two-layer laboratory density decay also contained significantly more scatter than did normalized height [Wallace and Wilkinson, 1988], again consistent with these observations (Figure 3.15). Upslope laboratory $\Delta T/\Delta T_0$ decrease with $\Delta x/\Delta x_{\mathrm{R}}$ was attributed to mixing and entrainment from the surrounding fluid and downrush from previous events. For the continuously stratified events A–D, the reduction in ΔT may also be due to mixing at the event front. Prior to the event start, the temperature was homogeneous. With the event arrival, the S8 onshore near-bed and offshore near-surface flow and the delayed near-surface cooling (Figure 3.8) also suggests mixing in the event front, as the offshore flowing near-surface water would remain warm otherwise. However, the observed ΔT reduction may also be because upslope locations are closer to the

surface (higher z), and S8 temperature drop is reduced at higher z (Figure 3.8). Some combination of these two mechanisms may explain the upslope ΔT decrease.

3.6.2 Potential vertical mixing during the NLIW rundown

Any mixing at the event front cannot be quantified here. However, after internal runup reaches x_{R}, dense water then flows back downslope (rundown) during which significant mixing occurs in both observations in $h \approx 15$ m [Walter et al., 2012] and numerical simulations [Arthur and Fringer, 2014]. Here, vertical mixing in the internal swashzone during the rundown of example event C (temperature in Figure 3.8a) is inferred through the evolution of vertically-integrated and horizontally-averaged potential energy $\Delta\langle \mathrm{PE} \rangle$, buoyancy frequency squared N^2, shear-squared S^2 and gradient Richardson number $\mathrm{Ri} = N^2/S^2$ that indicates when a stratified flow is dynamically unstable (< 0.25).

The time evolution of potential energy (3.5) is horizontally averaged over the wave runup extent

$$\langle \mathrm{PE} \rangle(t) = \Delta x_{\mathrm{R}}^{-1} \int_{\mathrm{S8}}^{x_{\mathrm{R}}} \mathrm{PE}(x,t)\,\mathrm{d}x \tag{3.16}$$

and the change in this quantity from the event arrival at t_{f1} is

$$\Delta\langle \mathrm{PE} \rangle(t) = \langle \mathrm{PE} \rangle(t) - \langle \mathrm{PE} \rangle(t_{\mathrm{f1}}) \tag{3.17}$$

which evolves due to both reversible (adiabatic advection) and irreversible (mixing) density changes e.g., [Winters et al., 1995]. The stratification is given by $N^2 = (g/\rho_0)\,\partial\rho(z)/\partial z$, where $\partial\rho/\partial z$ is found from a least-squares fit over a mid-depth range at S8 (-5.7 m $\leq z \leq$ -2.7 m). Baroclinic velocity shear-squared $S^2 = (\Delta U'/\Delta z)^2 + (\Delta V'/\Delta z)^2$ is found for the same mid-depth range. Here, $\Delta U'$ (and $\Delta V'$) is the difference between the vertically averaged baroclinic velocity near the top of the mid-depth range (-4.2 m $\leq z \leq$ -2.7 m) and near the bottom of the mid-depth range (-5.7 m $\leq z \leq$ -4.2 m). The vertical distance between the centers of the two

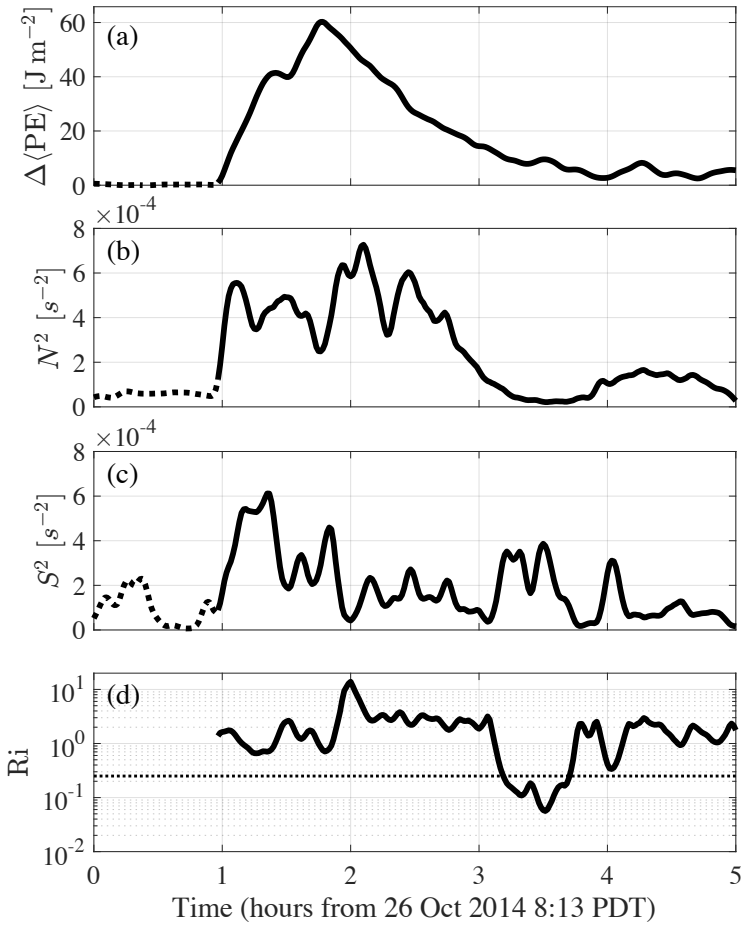

Figure 3.19: Five hour time series during event C of (a) event-induced change in horizontally-averaged potential energy $\Delta\langle \mathrm{PE}\rangle$ (3.17) (b) mid-water squared buoyancy frequency N^2 at S8, (c) squared mid-water shear S^2 at S8, and (d) the gradient Richardson number $\mathrm{Ri} = N^2/S^2$ at S8. All values have been smoothed (5-min filter). Dotted lines in (a-c) indicate measurements recorded before the arrival of the event front at hour 1. The horizontal dotted line in (d) is the critical Richardson value (0.25).

ranges $\Delta z = 1.5$ m.

Before the event arrival, $\Delta\langle \mathrm{PE} \rangle$, N^2 and S^2 were consistent and low (dotted lines, Figure 3.19a-c). After the event onset near hour 1, cold water pulsed onshore, elevating $\Delta\langle \mathrm{PE} \rangle$ to near 60 $\mathrm{J\,m^{-2}}$ approximately 45 minutes later (Figure 3.19a). The cold pulse stratified the water column while creating shear at mid-depths, leading to N^2 and S^2 above 4×10^{-4} $\mathrm{s^{-2}}$ (Figure 3.19b-c). During the onrush (hour 1 to 2 when near bottom U' was positive, Figure 3.8b), Ri was near 1, though always above 0.25, suggesting that sustained local vertical mixing at S8 was unlikely (Figure 3.19d) consistent with model studies and microstructure observations on shallow slopes e.g., [Moore et al., 2016, Bourgault et al., 2008]. Although these observations show no evidence of shear-driven mixing during the onrush, observations of similar bores have measured elevated turbulence (both advected and locally generated) during the bore passage very near the bottom [Richards et al., 2013]. Between hours 2 and 3, near-bed U' is offshore as cold water begins to advect back downslope (Figure 3.8b). As S8 bottom temperature increases (Figure 3.8a), $\Delta\langle \mathrm{PE} \rangle$ and N^2 decrease (Figure 3.19a and b). However, Ri is consistently above the critical value (Figure 3.19d) indicating that local shear-driven mid-water vertical mixing is still unlikely at S8.

As the rundown intensifies after hour 3 at S8, mid-water S^2 at S8 increases again while N^2 is small, causing Ri to drop below the critical value (Figure 3.19b-d). At this time, shear-driven mixing at mid-depths is possible at S8. The timing of this drop in Ri corresponds with a period of bottom warming and surface cooling (Figure 3.8a), with the transition depth between the cooling surface and warming bottom near where U' changes sign ($z \approx -3.5$ m). The direction of U' at this time (onshore at the surface and offshore at depth) potentially advects recently mixed cooler water near the surface offshore of S8 onshore. The difference in local mixing at S8 between internal runup uprush and downrush is consistent with differences in mixing and sediment suspension during uprush and downrush in a surface gravity swashzone [Puleo et al., 2000].

After the event (4–5 h), the internal swashzone is slightly cooler (compare cross-shore bottom temperature before and after the event at locations offshore of x_R in Figure 3.9a and vertical

temperature structure at S8 in Figure 3.8a). Due to the post-event remaining cold water, $\Delta\langle \mathrm{PE} \rangle \approx 4.9\,\mathrm{J\,m^{-2}}$ which is roughly 10% the maximum $\Delta\langle \mathrm{PE} \rangle$. As the sun was warming the nearshore at this time (decreasing $\Delta\langle \mathrm{PE} \rangle$) and alongshore currents were small (mean $\overline{V} < 0.003\,\mathrm{m\,s^{-1}}$), the residual $\Delta\langle \mathrm{PE} \rangle$ is likely due to irreversible mixing during the event. This residual $\Delta\langle \mathrm{PE} \rangle$ implies an average irreversible buoyancy flux of $5 \times 10^{-4}\ \mathrm{W\,m^{-2}}$, which is nearly a factor 50 lower than that inferred from highly stratified estuary observations [Bourgault et al., 2007].

3.6.3 Complexity of NLIW runup in the internal swashzone

For the four isolated events, the upslope evolution of event parameters ($c_\mathrm{f}(x)$, $\Delta T(x)$, $z_\mathrm{IW}(x)$) can be predicted (although Δx_R is over-predicted) given water column observations at some offshore location within the internal swashzone. This can provide insight into the onshore transport of intertidal settling larvae e.g., [Pineda, 1999] and other tracers exchanged with the surfzone. However, these four events were relatively simple (isolated, normally-incident, and homogeneous pre-event) - analogous to laboratory observations. Even the 14 events at S8 (Figures 3.10– 3.11b) were relatively simple. These restrictions on event and isolated event definitions eliminated most period I NLIW cold pulses and several significant events from period II (e.g., Figures 3.3 and 3.4).

In general, the NLIW field is very complex, containing large amplitude isotherm oscillations over a range of frequencies (M2, its harmonics, as well above 1 cph) which evolve over spring-neap conditions. The broad S18 high frequency spectral peak (centered between 6–10 cph) observed during period I (red, Figure 3.7c) is also present in other studies, particularly near topographic features e.g., [Desaubies, 1975, D'Asaro et al., 2007]. Overlapping cold pulses at variable angles of incidence and potential reflection (e.g., Figure 3.12) are common. This region onshore of a submarine canyon system (Figure 3.1a) may also be unusual in terms of the NLIW field. The observed complex NLIW conditions demonstrate that the internal swashzone is more complex than that described only from isolated events, similar to a surface gravity wave

swashzone.

The wave by wave evolution of internal runup is likely affected by interaction between individual runup events. Runup events can interact via bore-bore capture (potentially observed in Figure 3.12), which in a surface gravity swashzone leads to the largest runup events e.g., [García-Medina et al., 2017]. Event interactions also can include modification of background conditions through which subsequent waves propagate, or interference between the previous event rundown and runup of the next event e.g., [Moore et al., 2016, Davis et al., 2017]. Laboratory observations indicate internal wave breaking and elevated mixing due to interaction with a previous event's downrush [Wallace and Wilkinson, 1988, Helfrich, 1992]. Downslope bottom flow prior to the event e.g., [Helfrich, 1992, Sutherland et al., 2013a] was occasionally observed (e.g., hour 1.75 below $z = -6$ m in Figure 3.8b). Although not observed here, the downrush may eventually detach, similar to laboratory observations of gravity current intrusions [Maurer et al., 2010]. Internal bores have been previously observed to resuspend fine sediments creating an intermediate layer offshore [Masunaga et al., 2015]. While the location of maximum sediment suspension is likely offshore of the study area [Bourgault et al., 2014], currents from the nearshore downrush may contribute to sediment redistribution and the formation of intermediate nepheloid layers similar to those observed from internal wave reflection e.g., [McPhee-Shaw and Kunze, 2002].

Statistics of the offshore surface gravity wave field can be related to statistics of runup extent for a surface gravity swashzone e.g., [Holland and Holman, 1993, Raubenheimer and Guza, 1996]. For example offshore significant wave height, peak period, and beach slope can be used to reasonably accurately simulate the cross-shore variance of runup excursion up a beach e.g., [Stockdon et al., 2006, Senechal et al., 2011]. In less complicated locations (with a predictable internal wave climate), offshore internal tide and stratification statistics potentially can be combined with beach slope information to parameterize internal runup statistics.

3.7 Summary

For 30 days between 29 September and 29 October 2014, a dense thermistor array sampled temperature in depths shallower than 18 m, and a bottom-mounted ADCP in 8 m depth sampled 1 minute averaged velocity in 0.5 m vertical bins. A rich and variable internal wave field was observed from 18 m depth to the shoreline, with isotherm oscillations at a variety of periods, and a high frequency spectral peak (near 10 minute periods) when stratification was strong. Isotherm excursions were regularly $\pm$ 6 m during periods of high stratification; though isotherm excursions were less extreme, variability at all frequencies was reduced, and no high frequency spectral peak was observed when stratification decreased.

Cross-shore coherent pulses of cold water at M2 and M4 time scales were regularly observed throughout the observational period. NLIW event (rapid temperature drops and recovery) is evident from the baroclinic transport of cold water upslope, occasionally causing temperature drops of 0.7 °C in five minutes in water as shallow as 2 m. Fourteen isolated NLIW events were observed in 8 m depth propagating upslope with speeds (c_f) ranging from 1.4 $\mathrm{cm\,s^{-1}}$ to 7.4 $\mathrm{cm\,s^{-1}}$, propagation angles (θ) from -5° to 23° and temperature drops (ΔT) between 0.3 °C and 1.7 °C, decreasing upslope. The two-layer equivalent gravity current height (z_IW) decreased linearly upslope from initial values between 2.1 m and 2.5 m in 8 m depth and was consistent with observations of baroclinic velocity. Baroclinic bottom current during the upslope event propagation ($|U_\mathrm{b}'|$) was near the event front propagation speed, indicating high non-linearity, with mean $|U_\mathrm{b}'|/c_\mathrm{f} = 0.7$.

The upslope evolution of ΔT, z_IW, and c_f for four representative events most similar to two-layer laboratory conditions (alongshore uniform, shore-normal, isolated and propagating into homogeneous fluid) are qualitatively consistent with laboratory observations of broken internal wave runup. Normalized ΔT and z_IW for these events collapse as a linearly decaying function of normalized runup distance, and upslope gravity current scalings described the front speed c_f0 and

deceleration d_f well. The associated total runup distance (Δx_R) was also well predicted from c_{f0} and d_f, with rms error less than the resolution of the cross-shore thermistor array. However, Δx_R prediction with gravity current scalings has significant error due to sensitivity to c_{f0}.

Depressed temperature remained in the nearshore region for hours, until receding back downslope. Bottom temperature warmed and surface temperatures cooled during the receding rundown of an example event. The gradient Richardson number remained below the critical value (0.25) at this time, indicating shear driven mixing was occurring consistent with laboratory and modeling studies. The four NLIW events selected to compare with laboratory studies are simple cases. In general, NLIW runup is more complicated due to superposition (in ways similar to bore-bore capture) interaction with previous (receding) events, or as the diverse offshore NLIW field evolves. Any understanding of the internal swashzone beyond the most simple cases may require descriptions of complex interactions or a statistical approach similar to those used to describe the surface gravity wave swashzone.

3.8 Acknowledgments

This publication was prepared under NOAA Grant #NA14OAR4170075/ECKMAN, California Sea Grant College Program Project #R/HCME-26, through NOAAS National Sea Grant College Program, U.S. Dept. of Commerce. The statements, findings, conclusions and recommendations are those of the authors and do not necessarily reflect the views of California Sea Grant, NOAA or the U.S. Dept. of Commerce. Additional support for F. Feddersen was provided by the National Science Foundation, and the Office of Naval Research. B. Woodward, B. Boyd, K. Smith, R. Grenzeback, R. Walsh, J. MacKinnon, A. Waterhouse, M. Hamann and many volunteer scientific divers assisted with field work. Supplemental data was supplied by NOAA, CDIP, SCCOOS and CORDC with help from C. Olfe, B. O'Reilly and M. Otero. D. Grimes, S. Suanda and two anonymous reviewers provided feedback that significantly improved

the manuscript.

Chapter 3, in full, is a reprint of material as it appears in Sinnett, G., F. Feddersen, A. J. Lucas, G. Pawlak, and E. Terrill (2018), "Observations of nonlinear internal wave run-up to the surfzone," Journal of Physical Oceanography, 48(3), 531554. The dissertation author was the primary investigator and author of this paper.

Chapter 4

The Competing Effects of Breaking Waves on the Surfzone Heat Budget

4.1 Abstract

Depth-limited wave breaking modifies surfzone heat flux terms relative to where waves are not breaking. Breaking waves generate heat through viscous dissipation, but also increase surface foam coverage and albedo, thereby reducing solar heating. These two competing breaking wave effects are quantified using yearlong surface gravity wave, shortwave solar radiation, and bathymetric observations at the Scripps Institution of Oceanography Pier. Cross-shore averaged surfzone albedo was more than 3 times higher than inner-shelf albedo (where waves were not breaking), which, over the entire year reduced the cross-shore averaged water-entering shortwave radiation by 41 $\mathrm{W\,m^{-2}}$ in the surfzone relative to the inner-shelf. Breaking wave dissipation added an additional daily-averaged 28 $\mathrm{W\,m^{-2}}$ in the surfzone relative to the inner-shelf. The albedo-related solar heating reduction in spring, summer and fall was typically greater than the wave dissipation heating contribution. However, in winter with large waves and low shortwave solar radiation, contributions were similar with the wave dissipation heating term larger than the albedo-related shortwave solar radiation reduction $\approx 47\%$ of the time. The relationship between these two heat flux terms is coupled via wave breaking. The relative importance between breaking-wave dissipation heating and albedo-related solar radiation reduction (relative to where waves are not breaking) depends on beach slope, significant wave height, and incident shortwave solar radiation (a function of seasons, cloudiness and latitude).

4.2 Introduction

The surfzone (region where waves are breaking) and adjacent shallow inner-shelf (where waves are not breaking) together comprise the nearshore; a physically dynamic, economically important and biologically diverse part of the ocean. Temperature is an important physical attribute here, as temperature variation affects growth rates, recruitment rates and egg mass production rates of various species e.g., [Phillips, 2005, Fischer and Thatje, 2008, Broitman et al.,

2005] as well as pathogen ecology e.g., [Goodwin et al., 2012]. Pathogen mortality is related to both temperature [Surbeck, 2009] and exposure to solar shortwave radiation e.g., [Sinton et al., 1999, Boehm et al., 2002, Sinton et al., 2002]. In the nearshore, temperature can also be a tracer for nutrient delivery e.g., [Omand et al., 2012] or surfzone to inner-shelf water mass exchange e.g., [Hally-Rosendahl et al., 2014].

Consequently, quantitatively understanding physical mechanisms affecting the inner-shelf heat budget has been an active area of recent study. Inner-shelf heat budgets include upwelling e.g., [Lentz, 1987, Fewings and Lentz, 2011], wind stress e.g., [Austin, 1999], eddies e.g., [Wilkin, 2006], internal waves e.g., [Shroyer et al., 2010] and the passage of weather systems on time-scales of days to weeks e.g., [Austin and Lentz, 1999]. Heat transfer between the air/sea interface occurs through radiative solar shortwave heating, net long-wave heat flux, as well as net latent and sensible heat exchange. These terms are difficult to measure directly, and are thus frequently parameterized e.g., [Fairall et al., 1996, Beardsley et al., 1998, Fairall et al., 2003] when applied to observational and modeling studies e.g., [Lentz, 1987, Wilkin, 2006, Etter et al., 2004, Davis et al., 2011].

Closer to shore, rip currents (narrow wave-driven ejections from the surfzone) have been associated with strong temperature variation on the inner-shelf [Arthur, 1955, Smith and Largier, 1995], interacting with and adjusting the vertical temperature profile and influencing the inner-shelf cross-shore heat flux [Kumar and Feddersen, 2017]. Thus, surfzone temperature (relative to the stratified inner-shelf) is an important determining factor for how this transport mechanism is established and evolves. Additionally, the presence of fecal indicator bacteria (FIB) near the Southern California coast varies with temperature [Boehm et al., 2004], and predictive models for pathogen transport in the surfzone include temperature and shortwave radiation e.g., [Boehm, 2003]. Further, solar-radiation induced *Enterococcus* (FIB) mortality contains cross-shore variation, and modeled FIB concentrations and decay rates were best predicted when cross-shore mortality gradients were included [Rippy et al., 2013]. Thus, cross-shore variation of

temperature and solar radiation affect many important biological processes, motivating a more complete understanding of surfzone to inner-shelf temperature and solar radiation differences.

Many aspects of the surfzone heat budget are similar to the inner-shelf heat budget, though strong temperature gradients between rip-current ejected surfzone water and inner-shelf water suggest they are not identical. Frequently, this difference is attributed to differential heating and cooling due to the smaller surfzone volume compared to the inner-shelf. However, waves dissipate energy in the surfzone (but not the inner-shelf) while creating spray and foam, affecting the heat budget as well. Surfzone covariance flux measurements indicate wave-generated spray may increase sensible heat transfer [MacMahan et al., 2018], and laboratory studies over foamy surfaces (such as exist within the surfzone) indicate latent heat transfer may be elevated [Chickadel, 2018]. Here, two additional wave-related modifications to the surfzone heat budget are explored. First, is a surfzone specific heating term arising from the viscous dissipation of breaking wave energy, termed "wave heating". Second, is a reduction in surfzone solar heating relative to the inner-shelf due to breaking-wave induced foam which creates a whiter surface, elevating reflectivity (albedo).

The wave heating contribution to the surfzone heat budget results from mechanical wave energy converted to heat through viscous dissipation and is also directly tied to offshore wave conditions. Waves outside the surfzone shoal and break in the shallow surfzone, generating turbulent energy. Some wave energy is reflected from the shoreline, however on shallow sloping beaches (such as in this study) the percentage of reflected wave energy is typically small ($< 3\%$) [Elgar et al., 1994]. Additional export of mechanical energy from the surfzone (via rip currents or undertow, for example) has been estimated to be many orders of magnitude smaller than incident wave energy flux on similar beaches [Sinnett and Feddersen, 2014]. Thus, the bulk of the incident wave energy is dissipated through turbulence in the water column and at the bed, and eventually converted to heat. Here, we estimate the additional heat to the surfzone through the wave-heating effect compared to the inner-shelf.

Solar heat flux is a major surfzone heat budget term at this site [Sinnett and Feddersen, 2014], so changes to the albedo, and thus the amount of absorbed solar radiation, are consequential. The surfzone surface is a combination of foam-free and foam covered areas due to the recent passage of breaking waves e.g., [Frouin et al., 1996]. As foam has a higher albedo ($\alpha \approx 0.55$ [Whitlock et al., 1982]) than foam free water ($\alpha \approx 0.06$ [Payne, 1972]), the average albedo is higher in the surfzone than in the relatively foam-free inner-shelf. Parameterizations exist for albedo in the presence of wind-generated whitecaps e.g., [Koepke, 1984, Frouin et al., 1996, Jin et al., 2011], however foam exists in the surfzone without wind, making these parameterizations inappropriate for surfzone applications. Recently, surfzone albedo parameterizations have been developed based on offshore wave conditions and bathymetry [Sinnett and Feddersen, 2016]. Here, this parameterization is applied to assess how waves reduce the surfzone solar heat flux relative to the inner-shelf.

The breaking wave related surfzone albedo increase can be large (as much as $8\times$ the inner-shelf albedo [Sinnett and Feddersen, 2016]) and the subsequent decrease in solar radiation significant. Similarly, the wave-heating contribution to the surfzone heat budget can dominate at times [Sinnett and Feddersen, 2014]. However, the relative significance of their combined effect on the surfzone heat budget, and under what conditions each dominate, is unknown. Here, surfzone parameterizations of wave heating [Sinnett and Feddersen, 2014] and wave-induced albedo increase [Sinnett and Feddersen, 2016] are applied to a year-long dataset in order to estimate the affect waves have on the surfzone heat and solar radiation budget. The experiment is detailed in section 4.3.1, with analysis methods described in section 4.3.2. Results are described in section 4.4, with implications for how waves might affect various other locations and beaches are discussed in section 4.5.

4.3 Methods

4.3.1 Instrumentation and Data Processing

A yearlong study was conducted at the Scripps Institution of Oceanography (SIO) pier (La Jolla California, 32.867N, 117.257W) between October 25, 2014 and October 25, 2015. The SIO pier extends 322 m west-north-west (288°) from Scripps beach into water depth $h \approx 7$ m (Figure 4.1a). The roughly alongshore uniform shoreline extends 200 m north to 500 m south of the pier. Cross-shore bathymetry profiles were conducted along the pier at 0.5 to 1 month intervals as wave conditions allowed. The cross-shore profile slopes gently with yearly bathymetric changes less than 0.3 m at any location, causing slope variation of less than 5%. The average slope in depths $h < 3.5$ m (typically includes the surfzone) is $s \approx 0.023$ (Figure 4.1b). The pier-end NOAA station (9410230) measured 6-min averaged tidal elevation η relative to the mean tide level (MTL). The cross-shore x coordinate is positive onshore, with the mean shoreline ($x = 0$) where MTL intersects the mean bathymetry, and alongshore coordinate y is positive toward the north, with $y = 0$ at the northern edge of the pier.

For the 365 days beginning October 25, 2014, hourly significant wave height H_s (zeroth moment of the hourly energy spectrum) and peak period T_p (period of the highest spectral energy density) were observed at the pier end (square, Figure 4.1a and b) by the Coastal Data Information Program (CDIP) station 073 pier-mounted Paros pressure sensor. When the sensor was inoperative ($< 7\%$ of the time), a spectral refraction wave model with very high skill and initialized from offshore buoys was used [O'Reilly and Guza, 1991, O'Reilly, W.C. and Guza, R.T., 1998, O'Reilly et al., 2016].

Concurrently, a Campbell Scientific NR01 four-way radiometer located mid-pier (triangle, Figure 4.1a and b) recorded one-minute averaged downwelling Q_{sw}^{d}, and reflected upwelling Q_{sw}^{u} solar shortwave radiation (wavelengths 300 nm to 2800 nm) as described in [Sinnett and Feddersen, 2016]. Although the radiometer was cleaned at regular intervals, rain or very dense

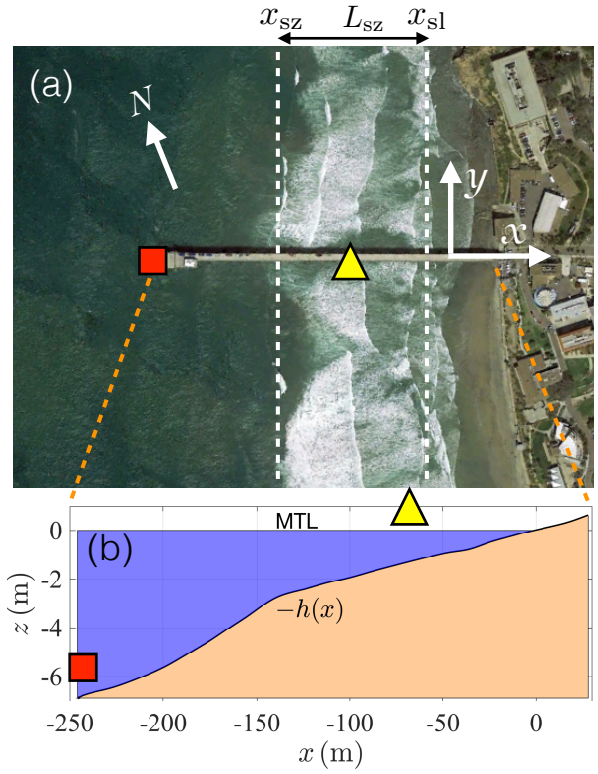

Figure 4.1: (a) Google earth image of the SIO pier experiment site near mid-tide with the x and y coordinates indicated. Locations of the wave and tide gauges (square) and radiometer (triangle) are shown relative to the pier. The surfzone width L_{sz} (white dotted) extends from the offshore limit of breaking x_{sz} to the effective shoreline x_{sl} where $h = 0.28$ m depth. (b) Cross-section along the SIO pier depicting mean tide level (MTL) and mean bathymetry $z = -h(x)$ versus cross-shore coordinate x with wave gauge (square) and radiometer (triangle) locations indicated. The radiometer elevation above MTL is $z = 6.5$ m (not to scale in b).

fog caused water to accumulate on the glass optics. Additionally, rarely occurring extremely low tides moved the shoreline seaward of the radiometer location so that the sensors viewed sand rather than water. Data during these times were flagged and removed from the record (6% of all data). For this study, radiation data was hourly-averaged onto the same temporal grid as the wave observations. Wave and radiation data were used to calibrate a parameterization relating offshore wave energy to surfzone albedo as described in section 4.3.2 and detailed in [Sinnett and Feddersen, 2016].

4.3.2 Analysis

Wave Model

The cross-shore transformation of normally-incident narrow-banded waves on alongshore uniform beaches is described by one-dimensional wave and roller transformation models e.g., [Thornton and Guza, 1983, Battjes and Stive, 1985, Ruessink et al., 2001]. The wave transformation is given by

$$\langle \varepsilon_b \rangle = -\frac{d}{dx}(E c_g), \tag{4.1}$$

where E is the wave energy density, c_g is the linear group velocity given by peak period and depth and $\langle \varepsilon_b \rangle$ is the bulk breaking wave dissipation. The wave energy density $E = 1/16 \rho g H_s^2$, where ρ is water density, g is gravity, and H_s is the significant wave height. The cross-shore wave energy flux at location x is

$$F_{\text{wave}}^{(x)} = E c_g \qquad \left[\mathrm{W\,m^{-1}}\right]. \tag{4.2}$$

The model adapted here follows [Church and Thornton, 1993] with standard breaking parameters ($B = 0.9$ and $\gamma = 0.57$).

Similarly, the wave roller transformation describes the dissipation along a breaking wave face with energy equation e.g., [Ruessink et al., 2001]

$$\frac{d}{dx}(2 E_r c) = -\langle \varepsilon_r \rangle + \langle \varepsilon_b \rangle. \tag{4.3}$$

Here, E_r is the roller energy density, c is the linear phase speed and roller dissipation $\langle \varepsilon_r \rangle$ (analogous to foam) is

$$\langle \varepsilon_r \rangle = \frac{2 g E_r \sin\beta}{c}, \tag{4.4}$$

with wave slope $\beta = 0.1$ e.g., [Deigaard, 1993, Walstra et al., 1996]. The model boundary conditions are the pier-end year-long hourly H_s and peak period observations.

A typical cross-shore wave transformation over bathymetry is illustrated with an example from May 5, 2015 at 14:00 PDT (Figure 4.2a). Observed offshore wave height $H_s = 1.4$ m, slightly increases onshore before breaking due to the shallowing bathymetry (set-up and set-down are ignored in the transformation model). As waves break, H_s decreases from the outer surfzone to the shoreline (black, Figure 4.2b) also reducing the wave energy flux F_{wave} (red, Figure 4.2b). The example cross-shore $\langle\widehat{\varepsilon_r}\rangle$ profile (black, Figure 4.2c) has peaks where waves are breaking over shallowing bathymetry and troughs where bathymetry is flatter or wave height is very low.

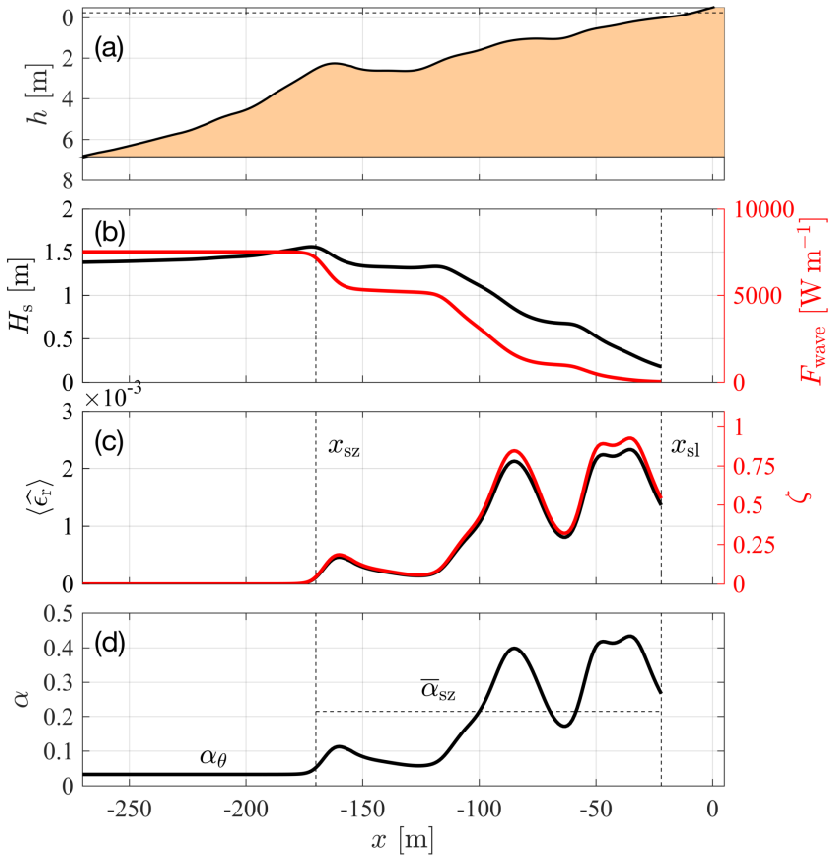

Figure 4.2: Example cross-shore (x) variation of hourly-averaged parameters from May 5, 2015 at 14:00 local time. (a) Bathymetry $h(x)$ (solid) and mean water level η (dotted), (b) significant wave height H_s (black) and associated cross-shore wave energy flux F_{wave} from (4.2) (red), (c) non-dimensionalized roller energy dissipation $\langle\widehat{\varepsilon_r}\rangle$ from (4.11) and foam fraction ζ from (4.12) as black and red respectively, and (d) albedo α_{sz} (4.13). The offshore breaking location $x_{sz} = -170$ m and effective shoreline $x_{sl} = -22$ m (black dashed in b, c and d). The cross-shore averaged surfzone albedo $\alpha_{sz} = 0.21$ (black dashed) and albedo where waves are not breaking (with clear sky conditions) $\alpha_\theta = 0.04$ are indicated in (d).

The outer-surfzone boundary, x_{sz} is defined as the farthest offshore location where $\langle\widehat{\varepsilon_r}\rangle > 1\times10^{-4}$ (vertical dotted in Figure 4.2b, c and d). In very shallow water, wave transformation models contain significant error, so the "effective shoreline," x_{sl} is defined as the first offshore location where $h > 0.28$ m; a depth selected where the average modeled $\langle\widehat{\varepsilon_r}\rangle$ has an onshore minimum. Waves in water shallower than $h = 0.28$ m are considered swash and this region is ignored. The effective surfzone width L_{sz} is

$$L_{sz} = x_{sl} - x_{sz} \qquad [\mathrm{m}]. \tag{4.5}$$

For the example in Figure 4.2, $x_{sz} = -170$ m and $x_{sl} = -22$ m, making the effective surfzone width $L_{sz} = 148$ m.

Wave Heating

Cross-shore wave energy flux is dissipated across the surfzone by breaking (4.1). Since wave reflection on shallow sloping beaches is small [Elgar et al., 1994] as is export of mechanical energy from the surfzone [Sinnett and Feddersen, 2014], the bulk of the wave energy flux is frictionally dissipated inside the surfzone, eventually as heat. Assuming the surfzone is well mixed, the heating from wave energy flux dissipation occurs over the entire surfzone width. Thus, the surfzone area-averaged additional heat flux (relative to no wave breaking on the inner-shelf) due to the dissipation of breaking waves is

$$Q_{wave} = \frac{F_{wave}^{(x_{sz})} - F_{wave}^{(x_{sl})}}{L_{sz}} \qquad \left[\mathrm{W\,m^{-2}}\right], \tag{4.6}$$

where superscripts indicate the cross-shore flux location. In the example, at x_{sz}, $F_{wave}^{x_{sz}} = 7500$ $\mathrm{W\,m^{-1}}$ but at x_{sl} $F_{wave}^{x_{sz}} = 33$ $\mathrm{W\,m^{-1}}$ (red, Figure 4.2b) implying that at this example time, there is a 7467 $\mathrm{W\,m^{-1}}$ energy flux convergence in the surfzone (or ≈ 50 $\mathrm{W\,m^{-2}}$) which is largely viscously dissipated and converted to heat.

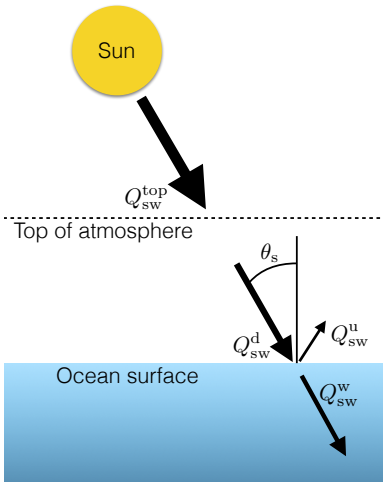

Figure 4.3: Schematic depicting the shortwave solar radiation ($Q_{\rm sw}$, arrows) at different locations: the top of the atmosphere (dotted line) $Q_{\rm sw}^{\rm top}$, downwelling to the ocean surface $Q_{\rm sw}^{\rm d}$, upwelling (reflected) at the ocean surface $Q_{\rm sw}^{\rm u}$, and water-entering $Q_{\rm sw}$. The solar zenith angle is $\theta_{\rm s}$.

Solar Radiation

Top of the atmosphere shortwave solar radiation ($Q_{\rm sw}^{\rm top}$ in Figure 4.3) is

$$Q_{\rm sw}^{\rm top} = S\cos(\theta_{\rm s})\Gamma^{-2} \qquad \left[\mathrm{W\,m^{-2}}\right], \tag{4.7}$$

where S is the solar constant and Γ is the ratio of the actual to mean earth-sun separation distance which varies on annual time-scales e.g., [Whiteman and Allwine, 1986]. Atmospheric attenuation and clouds reduce $Q_{\rm sw}^{\rm top}$ so that the downwelling radiation at the ocean surface is $Q_{\rm sw}^{\rm d} < Q_{\rm sw}^{\rm top}$ (Figure 4.3). The atmospheric reduction in downwelling shortwave solar radiation is defined as

$$\Delta Q_{\rm sw}^{\rm d} = Q_{\rm sw}^{\rm top} - Q_{\rm sw}^{\rm d} \qquad \left[\mathrm{W\,m^{-2}}\right], \tag{4.8}$$

and indicates cloudiness.

The shortwave albedo (reflectance) of the ocean surface is the ratio of the reflected

(upward) solar radiation to the downwelling solar radiation at the ocean surface,

$$\alpha = \frac{Q_{\mathrm{sw}}^{\mathrm{u}}}{Q_{\mathrm{sw}}^{\mathrm{d}}}, \tag{4.9}$$

so that the water-entering shortwave radiation (Figure 4.3) is

$$Q_{\mathrm{sw}} = Q_{\mathrm{sw}}^{\mathrm{d}}(1-\alpha) \qquad \left[\mathrm{W\,m^{-2}}\right]. \tag{4.10}$$

Thus, changes to either the available downwelling radiation $Q_{\mathrm{sw}}^{\mathrm{d}}$ or the albedo α affect the water-entering shortwave radiation and thus solar heating.

Breaking Wave-induced Albedo Increase

Standard non-wave breaking albedo parameterizations depend on the solar zenith angle θ_{s} (sun declination angle from vertical) [Payne, 1972, Briegleb et al., 1986, Taylor et al., 1996]. Yet in diffuse light (defined here when the ratio of atmospheric reduction in shortwave radiation to top-of-atmosphere shortwave radiation $\Delta Q_{\mathrm{sw}}^{\mathrm{d}}/Q_{\mathrm{sw}}^{\mathrm{top}} > 0.5$) ocean surface albedo is near 0.06 and no longer depends on θ_{s} [Payne, 1972]. Thus, in this study, the inner-shelf albedo (where waves are not breaking) α_θ is defined following [Taylor et al., 1996] treating the surface of the ocean as a specular reflector in direct sunlight making albedo only a function of solar zenith angle θ_{s}. Latitude and local time define θ_{s} following [Reda and Andreas, 2008]. In diffuse light, $\alpha_\theta = 0.06$.

In the surfzone, however, albedo is also dependent on the amount of surface foam present due to the passage of breaking waves. Following [Sinnett and Feddersen, 2016], foam fraction ζ is a function of the non-dimensionalized wave roller dissipation $\langle\widehat{\varepsilon_{\mathrm{r}}}\rangle$ (denoted with $\widehat{(\cdot)}$),

$$\langle\widehat{\varepsilon_{\mathrm{r}}}\rangle = \frac{\langle\varepsilon_{\mathrm{r}}\rangle}{\rho(gh)^{3/2}}. \tag{4.11}$$

Over the range of $\langle\widehat{\varepsilon_{\mathrm{r}}}\rangle$ typically observed at this location, the foam fraction ζ and $\langle\widehat{\varepsilon_{\mathrm{r}}}\rangle$ are linearly

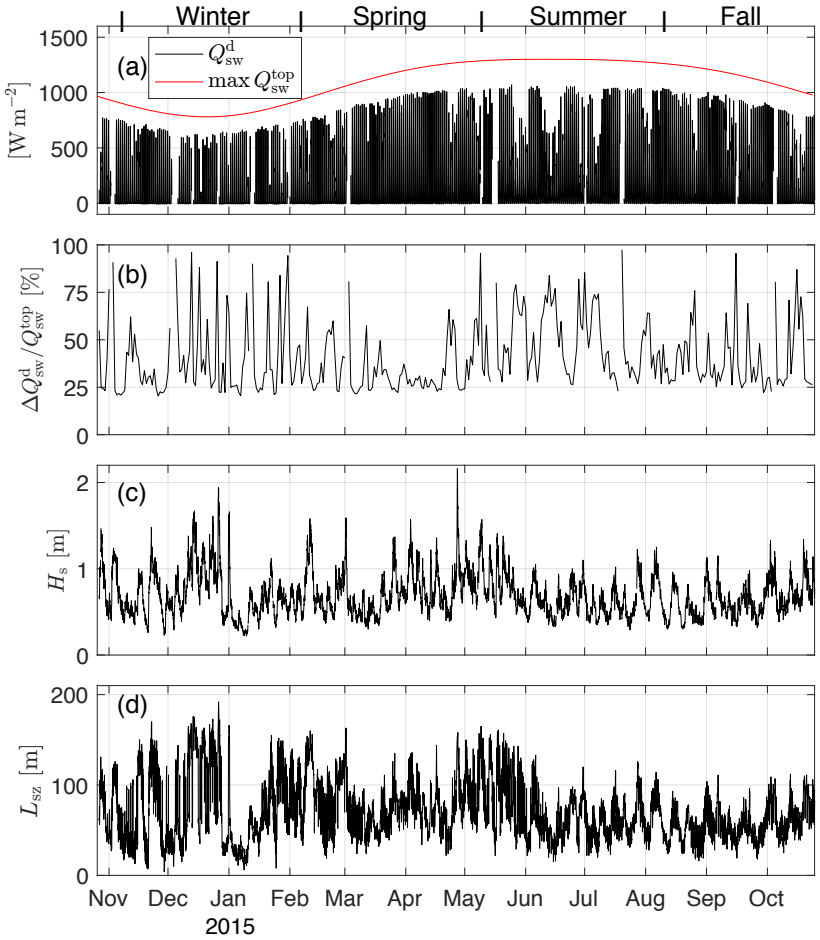

Figure 4.4: Yearlong time series of (a) daily maximum solar radiation at the top of atmosphere (max)$Q^{\mathrm{top}}_{\mathrm{sw}}$ (red) and hourly averaged downwelling shortwave solar radiation to the ocean surface $Q^{\mathrm{d}}_{\mathrm{sw}}$ (black), (b) daily percent reduction of downwelling solar shortwave radiation due to cloud cover $\Delta Q^{\mathrm{d}}_{\mathrm{sw}}/Q^{\mathrm{top}}_{\mathrm{sw}}$, (c) pier-end significant wave height H_{s}, and (d) surfzone width L_{sz} (4.5). Seasons denoted in (a) are 91 days long, centered on each solstice and equinox. Data in (a) is removed when rain obscured the radiometer.

related [Sinnett and Feddersen, 2016] so that

$$\zeta(x) = m\langle\widehat{\varepsilon_{\mathrm{r}}}\rangle(x), \tag{4.12}$$

where, $m = 398$ is a constant fit parameter. The example cross-shore ζ profile (red, Figure 4.2c) includes locations near $x = -75$ m and $x = -40$ m that are nearly continuously covered in foam, while only a few (large) waves break seaward of $x = -150$ m reducing ζ. Under extremely

energetic wave conditions, parts of the surfzone can saturate so that the fit produces $\zeta > 1$. When this occurs (less than 4% of the time) the foam fraction is restricted to the physical maximum $\zeta = 1$.

The wave affected (surfzone) albedo α_{sz} has contributions from both the foam-covered and foam-free surface, making

$$\alpha_{sz}(x) = \zeta(x)\alpha_f + (1-\zeta(x))\alpha_\theta, \tag{4.13}$$

(Figure 4.2d). Here, $\alpha_f = 0.465$ from the best-fit slope in [Sinnett and Feddersen, 2016], and α_θ is the parameterized albedo of foam-free water as a function of solar zenith angle e.g., [Taylor et al., 1996]. The cross-shore surfzone average foam fraction is

$$\overline{\zeta} = \frac{1}{L_{sz}} \int_{x_{sl}}^{x_{sz}} \zeta \, dx. \tag{4.14}$$

which yields a cross-shore average surfzone albedo α_{sz} through (4.13),

$$\alpha_{sz} = \overline{\zeta}\alpha_f + (1-\overline{\zeta})\alpha_\theta, \tag{4.15}$$

The area-averaged difference in water-entering solar radiation (4.10) between the surfzone and inner-shelf is then

$$\Delta Q_{sw}^{w} = Q_{sw}^{d}(\alpha_\theta - \alpha_{sz}) \qquad \left[\mathrm{W\,m^{-2}}\right]. \tag{4.16}$$

Both the amount of available downwelling radiation Q_{sw}^{d} and the albedo difference between surfzone and inner-shelf affect ΔQ_{sw}^{w}. As $\alpha_{sz} > \alpha_\theta$, the foam-induced surfzone albedo creates a net surfzone cooling relative to the inner-shelf.

4.4 Observations and Results

4.4.1 Observed $Q_{\mathrm{sw}}^{\mathrm{d}}$, H_{s}, F_{wave} and Albedo

At the top of the atmosphere at the experiment site, solar radiation $Q_{\mathrm{sw}}^{\mathrm{top}}$ varies with θ_{s} on diurnal and seasonal time scales, so that the daily maximum $Q_{\mathrm{sw}}^{\mathrm{top}}$ (red, Figure 4.4a) contains only seasonal variation. At the water surface (bottom of the atmosphere) available downwelling solar radiation $Q_{\mathrm{sw}}^{\mathrm{d}}$ primarily varied diurnally, but also varied at synoptic to seasonal time scales (black, Figure 4.4a). On clear days, atmospheric attenuation caused the ratio of the atmospheric shortwave reduction to the radiation at the top of the atmosphere ($\Delta Q_{\mathrm{sw}}^{\mathrm{d}}/Q_{\mathrm{sw}}^{\mathrm{top}}$) to be near 0.25, whereas clouds decreased the available $Q_{\mathrm{sw}}^{\mathrm{d}}$ further (Figure 4.4b). In winter, cloudy periods usually lasted a few days (jagged peaks, Figure 4.4b) and were frequently accompanied by rain causing short $Q_{\mathrm{sw}}^{\mathrm{d}}$ data gaps. In the very late spring and early summer, coastal fog persisted for longer periods causing $\Delta Q_{\mathrm{sw}}^{\mathrm{d}}/Q_{\mathrm{sw}}^{\mathrm{top}}$ to remain elevated longer (Figure 4.4b). Early spring, late summer and early fall were typically less cloudy.

Pier-end significant wave height H_{s} typically varied synoptically between 0.5 m and 1.5 m, with generally larger wave events in winter and spring, and smaller waves in summer and fall (Figure 4.4c). Pier-end peak period (wave period containing maximal spectral energy) was usually between 7 s and 13 s. The mixed barotropic tide typically varied $\pm$ 1 m (not shown) inducing a roughly $\pm$43 m variation in x_{sl}. Wave and tide conditions, together with the evolving bathymetry, affected the surfzone width L_{sz} (Figure 4.4d). Average $L_{\mathrm{sz}} = 84$ m, but was at times above 150 m during strong wave events and as small as 4 m when waves were small. Time periods were excluded when waves were small and x_{sz} was in less than 0.5 m depth (*i.e.*, $L_{\mathrm{sz}} < 10$, less than 0.2% of all data).

At the outer surfzone boundary, wave energy flux $F_{\mathrm{wave}}^{(x_{\mathrm{sz}})} = 2149 \pm 1826\,\mathrm{W\,m^{-1}}$ driven primarily by variable H_{s} through (4.2) on synoptic time scales (Figure 4.5a). The quadratic relationship between F_{wave} and H_{s} (4.2) means large wave events (typically in winter with a few

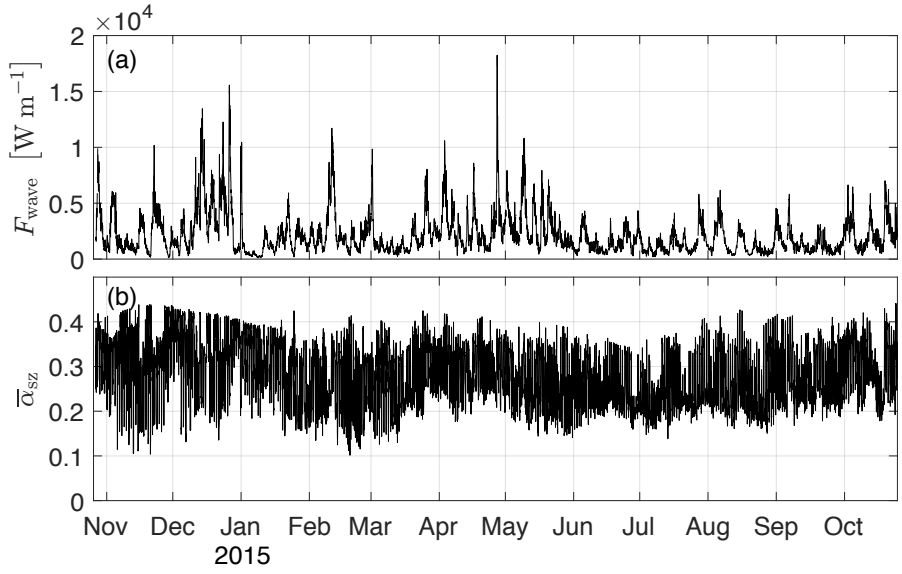

Figure 4.5: Hourly (a) pier-end wave energy flux F_{wave} (4.2) and (b) cross-shore averaged surfzone albedo α_{sz} (4.15) versus time of year.

in spring) have an outsized contribution to F_{wave}. Seasonal H_{s} variability affected F_{wave}, with F_{wave} generally elevated in wintertime and reduced in summertime. The cross-shore average surfzone albedo α_{sz} (4.15) had mean value of 0.28 (more than 3 times the mean inner-shelf albedo), and varied with standard deviation of 0.07 (Figure 4.5b). Variation in α_{sz} is due to both diurnal variation in α_θ (related to θ_{s}) and the foam fraction ζ through (4.13).

As the reduction in water entering shortwave solar energy $\Delta Q^{\text{w}}_{\text{sw}}$ (4.16) depends on α_θ, α_{sz} and Q^{d}_{sw} (all of which have diurnal dependance), and Q^{d}_{sw} is constant over the surfzone and inner-shelf, the overall impact of α_{sz} relative to α_θ is effectively demonstrated over daylight time-periods with ensemble averages. Observations made when solar zenith angle $|\theta_{\text{s}}| > 80^\circ$ are removed to avoid interference with a coastal bluff or atmospheric effects near the horizon. The remaining data are then binned by each 24-hour period and daylight hours are normalized onto a standard 12 hour vector to remove seasonal daylight variation, allowing direct inter-day albedo comparison. Daily ensemble averaged α_θ (blue line, Figure 4.6) has solar zenith angle θ_{s} dependence, with elevated albedo at low sun angles near sunrise and sunset. Seasonal variation in θ_{s} and cloud cover variation account for the α_θ deviation from the mean (blue shaded). As the

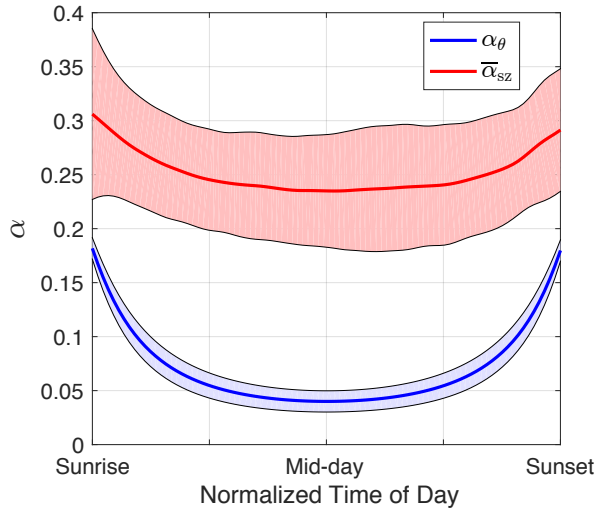

Figure 4.6: Daily ensemble averaged albedo with no wave breaking α_θ (blue) and daily ensemble averaged cross-shore averaged surfzone albedo α_{sz} [Sinnett and Feddersen, 2016] (red) versus normalized time of day. Shading is $\pm$ one standard deviation from the mean.

surfzone has fractional foam coverage, α_{sz} retains some θ_s dependance and is similarly elevated at high sun angles (red line, Figure 4.6). However, mid-day ensemble averaged α_{sz} is 0.19 larger than α_θ. Wave, tide and bathymetry variability influence $\overline{\zeta}$ and thus contributes to the added α_{sz} variability (red shaded).

4.4.2 Competing Wave Effects: ΔQ_{sw}^{w} and Q_{wave}

Wave breaking has two competing effects that heat and cool the surfzone relative to the inner-shelf (where waves are not breaking). Breaking wave energy dissipation Q_{wave} (4.6) leads to surfzone heating. Wave breaking also increases albedo, thereby reducing the water-entering shortwave solar radiation relative to the inner-shelf by an amount ΔQ_{sw}^{w} (4.16). Hourly observations of H_s and Q_{sw}^{d} (section 4.4.1) are used to estimate Q_{wave} through (4.6) and (4.2), and ΔQ_{sw}^{w} through (4.16) and (4.15). Variability in Q_{wave} and ΔQ_{sw}^{w} occur on seasonal, synoptic, diurnal and semi-diurnal timescales through variation in H_s, θ_s and L_{sz}. Here, Q_{wave} and ΔQ_{sw}^{w} are daily (24 h) averaged to examine breaking-wave effects on the longer synoptic and seasonal timescales. Henceforth all "Q" variables will be daily-averaged.

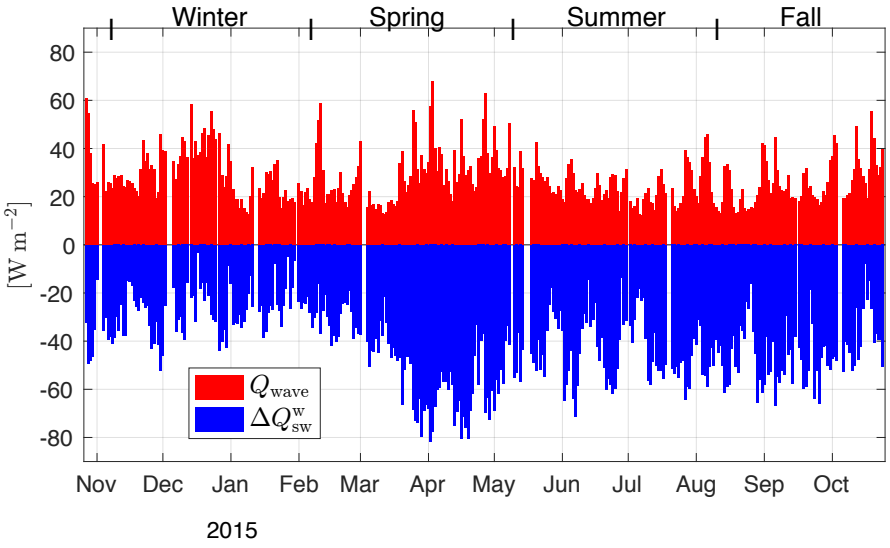

Figure 4.7: Yearlong time series of daily (24-hour) averaged wave-heating Q_{wave} (4.6), and reduction in solar heating through the breaking wave albedo reduction in solar heating $\Delta Q^{\mathrm{w}}_{\mathrm{sw}}$ (4.16) as indicated in the legend.

Breaking-wave related heat-flux contributions varied over the year (Figure 4.7) with Q_{wave} always increasing (positive) heat flux and $\Delta Q^{\mathrm{w}}_{\mathrm{sw}}$ always reducing (negative) heat flux to the surfzone relative to the inner-shelf. Over the year, the mean and standard deviation of the daily-averaged $Q_{\mathrm{wave}} = 28 \pm 11$ W m^{-2} (red) and $\Delta Q^{\mathrm{w}}_{\mathrm{sw}} = -41 \pm 16$ W m^{-2} (blue), thus at this location, wave breaking typically reduced the surfzone heat flux relative to the inner-shelf. Daily averaged Q_{wave} and $\Delta Q^{\mathrm{w}}_{\mathrm{sw}}$ were uncorrelated ($r^2 = 0.04$). Both Q_{wave} and $\Delta Q^{\mathrm{w}}_{\mathrm{sw}}$ had similar variability at synoptic (2-10 day) timescales. Monthly to seasonal variations in Q_{wave} are driven by variations in H_{s} (Figure 4.4c), while monthly to seasonal variation in $Q^{\mathrm{d}}_{\mathrm{sw}}$ are driven by variations in clouds, $Q^{\mathrm{top}}_{\mathrm{sw}}$, and waves. Throughout most of summer, clouds reduced $Q^{\mathrm{d}}_{\mathrm{sw}}$ and waves were small (Figure 4.4a-c). Thus, the yearly maximum $\Delta Q^{\mathrm{w}}_{\mathrm{sw}}$ occurred in April when waves were larger and cloudiness lower, and not at the summer solstice when $Q^{\mathrm{top}}_{\mathrm{sw}}$ is maximum.

The relative effects of Q_{wave} and $\Delta Q^{\mathrm{w}}_{\mathrm{sw}}$ have a seasonal dependance (Figure 4.8). In winter, $Q^{\mathrm{top}}_{\mathrm{sw}}$ is low and cloudiness $\Delta Q^{\mathrm{d}}_{\mathrm{sw}}/Q^{\mathrm{top}}_{\mathrm{sw}}$ can be high reducing $\Delta Q^{\mathrm{w}}_{\mathrm{sw}}$. Wintertime waves are also relatively large with $Q_{\mathrm{wave}} > 40$ W m^{-2} about 20% of the time. The combined effect in winter heats

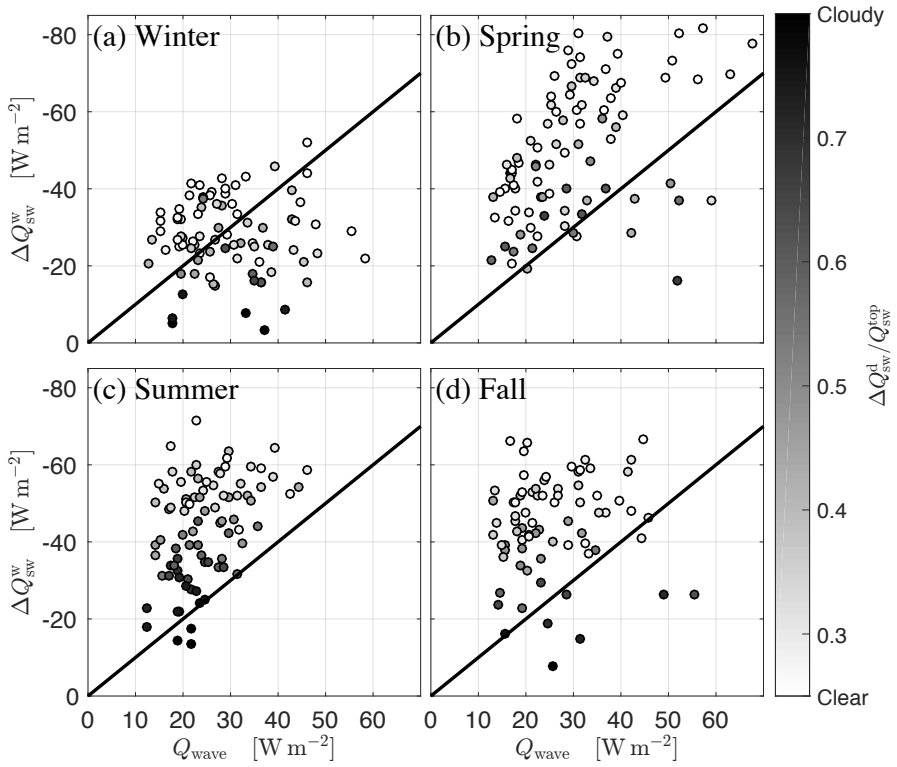

Figure 4.8: Daily averaged change to solar heating ΔQ_{sw}^{w} versus the daily averaged wave heating Q_{wave} for each season. Symbols are shaded according to $\Delta Q_{sw}^{d}/Q_{sw}^{top}$ representing bulk cloudiness (Figure 4.4b). Daily-averaged values fall to the right or left of the 1:1 line (solid black) contributing to net heating or cooling respectively (relative to the inner-shelf).

the surfzone relative to the inner-shelf 47% of the time (Figure 4.8a). In contrast, summertime waves were relatively small with $Q_{wave} > 40$ W m^{-2} only 5% of the time. The combined effect in summer cools the surfzone relative to the inner-shelf 89% of the time (Figure 4.8c).

Spring is characterized by a wide distribution of both Q_{wave} and ΔQ_{sw}^{w} (Figure 4.8b). Spring had few clouds, with $\Delta Q_{sw}^{d}/Q_{sw}^{top} > 40\%$ roughly a quarter of the time (compared to over half the time in summer). Spring also contained some of the largest observed H_s, with daily-averaged $Q_{wave} > 50$ W m^{-2} 11% of the time. Such large Q_{wave} conditions also happened 4% of the time in winter, and not at all in summer. Fall is characterized by only a slightly lower ΔQ_{sw}^{w} distribution compared to summer (Figure 4.8d). Fall Q_{sw}^{top} is smaller than in summer (red, Figure 4.4a), yet fall $\Delta Q_{sw}^{d}/Q_{sw}^{top}$ was lower (33% compared to 58%) such that mean Q_{sw}^{d} was

reduced by only 5%. Occasional large wave events in late fall (more typical of winter conditions) widened the fall Q_{wave} distribution compared to summer.

4.4.3 Surfzone Adiabatic Temperature Change

As temperature is the relevant physical quantity to circulation dynamics and ecology, relating Q_{wave} and $\Delta Q_{\text{sw}}^{\text{w}}$ to an adiabatic temperature change is useful for gauging the relative effects. Relative to the inner-shelf, the daily-averaged combined (Q_{wave} and $\Delta Q_{\text{sw}}^{\text{w}}$) surfzone heat flux Q_{net} is

$$Q_{\text{net}} = Q_{\text{wave}} + \Delta Q_{\text{sw}}^{\text{w}} \qquad \left[\text{W m}^{-2}\right], \tag{4.17}$$

with positive Q_{net} implying surfzone warming relative to the inner-shelf. The daily adiabatic temperature change ΔT caused by Q_{net} at a surfzone of constant slope is

$$\Delta T = \frac{t_{\text{day}}\, Q_{\text{net}}}{1/2\, h_{\text{sz}}\, \rho\, |c_{\text{p}}|} \qquad [^{\circ}\text{C}], \tag{4.18}$$

where $t_{\text{day}} = 86400$ s is the duration of a day and h_{sz} is the depth of the outer surfzone boundary. This assumes no heat exchange between surfzone and inner-shelf or other breaking-wave related air-sea fluxes.

At the experiment site, ΔT (black dots, Figure 4.9) was negative 75% of the time due to Q_{net}, with a yearly mean and standard deviation of $\Delta T = -0.5 \pm 0.6\ ^{\circ}$C. The ΔT mean and standard deviation also varied seasonally (red dots and red lines, Figure 4.9). Wintertime mean and standard deviation $\Delta T = 0.0 \pm 0.4\ ^{\circ}$C as wintertime Q_{net} is near zero (compare red and blue, Figure 4.7). Beginning in early spring, ΔT typically becomes negative, with mean and standard deviation $\Delta T = -0.7 \pm 0.5\ ^{\circ}$C between March and September. In late summer and early fall ΔT can be as low as $-1.9\,^{\circ}$C when cloudiness is low. Daily ΔT variability was also largest in spring and late summer when $Q_{\text{sw}}^{\text{top}}$ was high, but the presence of clouds or coastal fog caused large changes in $\Delta Q_{\text{sw}}^{\text{d}}$. The late fall reduction in $Q_{\text{sw}}^{\text{top}}$ and general increase in H_{s} (see Figure 4.4a

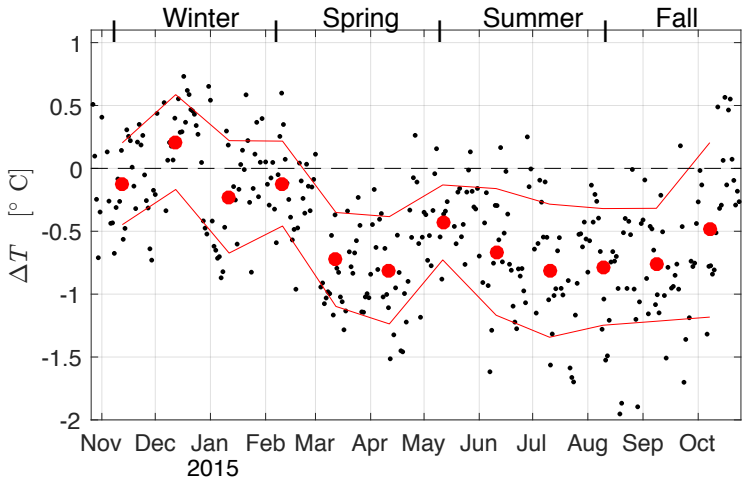

Figure 4.9: Yearly time series of daily adiabatic surfzone temperature change ΔT (black dots) as in (4.18) due to the competing wave effects of wave heating Q_{wave} and albedo-induced reduction of solar heating $\Delta Q^{\text{w}}_{\text{sw}}$. Monthly averages (red dots) and $\pm$ standard deviation (red lines), along with the $\Delta T = 0$ (dashed black) are highlighted for reference.

and c) prompts a return to winter conditions. The relative $Q^{\text{top}}_{\text{sw}}$, clouds, and H_{s} magnitudes in turn affect the relative strength of Q_{wave} and $\Delta Q^{\text{w}}_{\text{sw}}$. Different locations containing different parameter space will respond differently.

4.5 Discussion

At the La Jolla CA experiment site, the parameters H_{s}, $h(x)$, Q^{d}_{sw}, $Q^{\text{top}}_{\text{sw}}$, and cloudiness $\Delta Q^{\text{d}}_{\text{sw}}/Q^{\text{top}}_{\text{sw}}$ have been shown to contribute to the breaking-wave induced heating or cooling of the surfzone relative to the inner-shelf. Here, Q_{wave} and $\Delta Q^{\text{w}}_{\text{sw}}$ are placed in the context of a previous surfzone heat budget. Then, Q_{wave} and $\Delta Q^{\text{w}}_{\text{sw}}$ scalings for a constant slope surfzone are explored, leading to potential application at other sites with variable $Q^{\text{top}}_{\text{sw}}$, clouds, incident waves, and beach slope. Lastly, Q_{wave} and $\Delta Q^{\text{w}}_{\text{sw}}$ are considered in the context of other possible breaking wave effects to the sensible and latent heat.

4.5.1 Q_{wave} and $\Delta Q^{\text{w}}_{\text{sw}}$ in Context

The inclusion of wave-heating improved a summertime binned-mean surfzone heat budget on diurnal and longer time-scales [Sinnett and Feddersen, 2014]. However here summertime $|\Delta Q^{\text{w}}_{\text{sw}}| > |Q_{\text{wave}}|$, though as there is no correlation between Q_{wave} and $\Delta Q^{\text{w}}_{\text{sw}}$ ($r^2 < 0.04$), including Q_{wave} but not $\Delta Q^{\text{w}}_{\text{sw}}$ still improved the binned mean slope by reducing the unexplained variance. [Sinnett and Feddersen, 2014] found a net surfzone cooling of $\approx 5200\ \text{W}\,\text{m}^{-1}$ (or $\approx\ 62\ \text{W}\,\text{m}^{-2}$ over the average L_{sz}). Thus, $\Delta Q^{\text{w}}_{\text{sw}}$ may account for over half the inferred net cooling. Advective processes, such as transient rip currents or internal waves e.g., [Sinnett et al., 2018], or wave-related modifications to the latent of sensible heat flux may contribute to the remaining required surfzone cooling. Examination of the full surfzone heat budget is warranted to address the remaining residual cooling and variability at diurnal and faster time scales.

4.5.2 Scaling for an idealized surfzone

The surfzone averaged $Q_{\text{wave}} = F_{\text{wave}}/L_{\text{sz}}$. Similarly, the surfzone averaged non-dimensionalized roller dissipation is scaled as

$$\langle \widehat{\varepsilon_{\text{r}}} \rangle = \frac{F_{\text{wave}}/L_{\text{sz}}}{\rho \left(g\overline{h}_{\text{sz}}\right)^{3/2}}, \tag{4.19}$$

where the average surfzone depth $\overline{h}_{\text{sz}} = H_{\text{s}}/(2\gamma)$ and γ is a standard breaking parameter as in section 4.3.2. Although $\Delta Q^{\text{w}}_{\text{sw}}$ and Q_{wave} are uncorrelated, both parameterizations depend on incident wave conditions, so a relationship exists between the two with added variability from the other non-wave factors such as slope s and Q^{d}_{sw}. Here, we investigate how parameterized Q_{wave} and $\Delta Q^{\text{w}}_{\text{sw}}$ on an idealized beach with constant slope s and incident plane-parallel narrow-banded waves respond to changes in H_{s}, s and Q^{d}_{sw}.

As the surfzone averaged wave and roller dissipation are equivalent, non-dimensionalizing (4.1) and substituting in (4.12) then (4.14) allows estimation of $\overline{\zeta}$ for an idealized surfzone of

constant slope s as

$$\overline{\zeta} = \frac{mQ_{\text{wave}}}{\rho\left(g\overline{h}_{\text{sz}}\right)^{3/2}} = \frac{\sqrt{2}}{8}ms\gamma^2 \tag{4.20}$$

For an idealized surfzone with constant γ, the area-averaged foam fraction (and thus α_{sz}) is independent of H_{s} to leading order. Instead, $\overline{\zeta}$ is linearly related to beach slope. Daily averaged $\Delta Q^{\text{w}}_{\text{sw}}$ and Q^{d}_{sw} are expected to be related such that

$$\frac{\Delta Q^{\text{w}}_{\text{sw}}}{Q^{\text{d}}_{\text{sw}}} = \overline{\zeta}\left(\alpha_\theta - \alpha_{\text{f}}\right). \tag{4.21}$$

The right hand side of (4.21) is constant for constant s, meaning $\Delta Q^{\text{w}}_{\text{sw}}$ versus Q^{d}_{sw} (Figure 4.10) should have a constant slope.

Daily averaged $\Delta Q^{\text{w}}_{\text{sw}}$ is correlated with Q^{d}_{sw} ($r^2 = 0.5$) (Figure 4.10) with best-fit slope -0.19 (red line) representing the right hand side of (4.21) or the daily averaged albedo difference between the inner-shelf and the surfzone $\alpha_\theta - \alpha_{\text{sz}}$ (as in 4.16). Deviations from this slope are due to the uncorrelated tidal and H_{s} variation interacting with the real and slowly varying bathymetry causing variance in α_{sz} and L_{sz}. With an idealized (constant) bathymetric slope, the surfzone averaged foam fraction (4.20) applied to (4.22) yields a slope $\overline{\zeta}(\alpha_\theta - \alpha_{\text{f}}) = -0.21$ (black line, Figure 4.10). The correlation between $\Delta Q^{\text{w}}_{\text{sw}}$ and Q^{d}_{sw} and the similarity between the theoretical and best-fit slope (Figure 4.10) demonstrate the suitability of (4.20) and (4.21) to effectively scale $\Delta Q^{\text{w}}_{\text{sw}}$ on gently sloping and alongshore uniform beaches.

The relative importance of surfzone area-averaged $\Delta Q^{\text{w}}_{\text{sw}}$ to Q_{wave} for an idealized bathymetry is derived from (4.20) using (4.15) and (4.16), expressed as

$$\frac{|\Delta Q^{\text{w}}_{\text{sw}}|}{Q_{\text{wave}}} = \left[\left|\frac{2\sqrt{2}m\gamma^{3/2}\left(\alpha_\theta - \alpha_{\text{f}}\right)}{\rho\, g^{3/2}}\right|\right]\frac{Q^{\text{d}}_{\text{sw}}}{H^{3/2}_{\text{sb}}}, \tag{4.22}$$

which is independent of the bathymetric slope. Here, H_{sb} is the significant wave height at breaking (x_{sz}). With the daily-averaged clear-sky inner-shelf albedo $\langle\alpha_\theta\rangle = 0.06$ e.g., [Payne, 1972], the

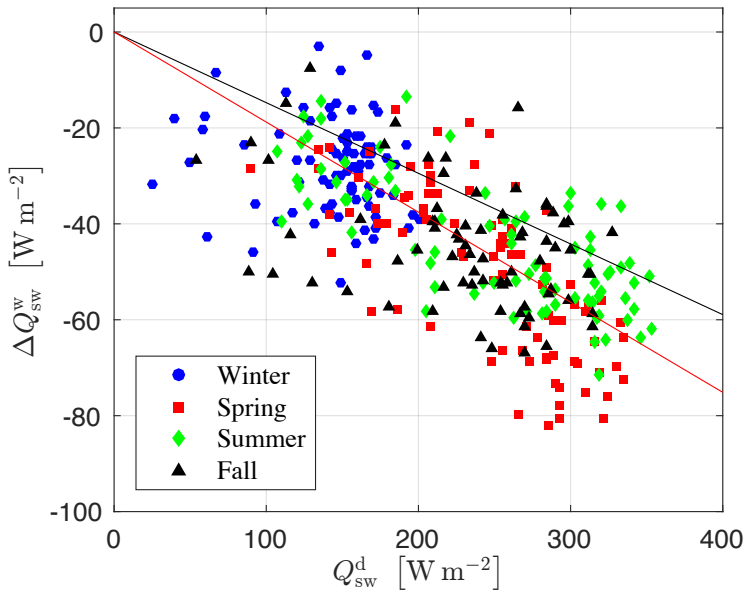

Figure 4.10: Daily-averaged change in water-entering shortwave solar radiation ΔQ^{w}_{sw} (4.16) between the surfzone and inner-shelf versus observed daily-averaged downwelling solar radiation Q^{d}_{sw}. Symbols are identified (color and shape) by season with the best-fit slope of -0.19 (red line) and idealized slope from (4.20 and 4.22) of -0.21 (black line). The squared correlation $r^2 = 0.5$.

bracketed quantity is constant and $\approx 6.212 \times 10^{-3}$. Thus, the seasonal variation in Figure 4.8 (points relative to the 1:1 line) can be understood from (4.22) as dependent on the ratio of Q^{d}_{sw} to $H^{3/2}_{sb}$.

The Q^{d}_{sw} to $H^{3/2}_{sb}$ ratio affecting the relative contribution of surfzone to inner-shelf ΔQ^{w}_{sw} cooling and Q_{wave} heating through (4.22) is affected by three varying parameters. Cloudiness and Q^{top}_{sw} affect Q^{d}_{sw}, in the numerator of (4.22). The Q^{top}_{sw} can be easily estimated through (4.7), and cloudiness (atmospheric attenuation or optical depth) may be obtained from terrestrial or satellite products such as e.g., [CERES, 2018]. The third parameter is wave height at the breakpoint H_{sb}, which is commonly measured with predictions available at many locations (as here with data from CDIP e.g., [O'Reilly and Guza, 1991, O'Reilly, W.C. and Guza, R.T., 1998, O'Reilly et al., 2016]).

These three parameters (clouds, Q^{top}_{sw} and H_{sb}) vary by season and location affecting

(4.22). For example, when clouds are low in tropical latitudes where Q_{sw}^{top} is very high, Q_{sw}^{d} is also high. Thus, surfzone cooling relative to the inner-shelf (ΔQ_{sw}^{w}) is dominant except for only extreme H_s conditions. When there are clouds, or in latitudes or seasons with low Q_{sw}^{top}, Q_{sw}^{d} drops. Subsequently, ΔQ_{sw}^{w} is reduced allowing Q_{wave} to become relatively more important, even during relatively low H_{sb} conditions. Thus, the scalings for $\langle \widehat{\varepsilon_r} \rangle$ (4.19), $\overline{\zeta}$ (4.20), and ΔQ_{sw}^{w} (4.21) allow for estimation of the relative importance of ΔQ_{sw}^{w} to Q_{wave} (4.22) for a variety of locations and conditions.

4.5.3 Application to the Surfzone Heat Budget

Breaking waves induce other heat fluxes in the surfzone relative to the inner-shelf. For example, breaking waves affect the sensible and latent heat flux. Surfzone sensible heat flux covariance measurements had an additional contribution due to spray from breaking waves not included in the COARE parameterization [MacMahan et al., 2018]. For the average wave dissipation observed at this site, additional sensible heat flux due to breaking wave spray is approximately to be $\approx 5\ \mathrm{W\,m^{-2}}$; relatively small compared to Q_{wave} and ΔQ_{sw}^{w} at Scripps Beach. Spray droplets produced by breaking are typically large [Andreas, 2016] and quickly fall back to the surface before exchanging latent heat [Veron, 2015, MacMahan et al., 2018]. However, the enthalpy exchange coefficient may be larger for a foamy sea surface than a foam-free ocean [Chickadel, 2018]. Separate spray-mediated and interfacial parameterizations may be required to accurately account for enthalpy fluxes in high spray conditions, similar to those done for high winds e.g., [Andreas, 2011, Richter and Stern, 2014]. Thus, accurate surfzone spray models may be needed in addition to the surface foam fraction ζ to parameterize wave effects on latent heat exchange. Surfzone spray and aerosol properties also depend on breaking wave dissipation $\langle \varepsilon_r \rangle$ [van Eijk et al., 2011b].

4.6 Summary

The nearshore (surfzone and adjacent inner-shelf) region is a dynamic and biologically important region. Temperature can affect many biological processes here, with temperature gradients also affecting transport and mixing between the surfzone and inner-shelf. Heat and solar radiation budgets for this region typically overlook breaking wave effects, and the relative importance of this adjustment is unknown. Here, wave heating due to viscous dissipation of breaking waves Q_{wave} is parameterized from [Sinnett and Feddersen, 2014], and surfzone cooling relative to the inner-shelf due to the presence of breaking wave foam through $\Delta Q_{\text{sw}}^{\text{w}}$ is parameterized from [Sinnett and Feddersen, 2016] using yearlong observations of waves and solar radiation. The resulting competing heating and cooling effects are quantified for this site, while scalings for these terms suggest how surfzone waves may affect heat and radiation budgets at other locations and beaches.

Wave energy flux at the outer surfzone boundary $F_{\text{wave}}^{x_{\text{sz}}} = 2149 \pm 1826 \text{ W m}^{-1}$, which dissipated over L_{sz} yielding a daily-averaged wave heating contribution $Q_{\text{wave}} = 28 \pm 11 \text{ W m}^{-2}$. Breaking surfzone waves partially covered the surfzone in foam, increasing albedo on average by a factor of 3 relative to the inner-shelf. The increased surfzone albedo subsequently reduced the shortwave solar radiation relative the inner-shelf creating a shortwave radiation difference $\Delta Q_{\text{sw}}^{\text{w}} = -41 \pm 16 \text{ W m}^{-2}$. The combined relative effect of Q_{wave} and $\Delta Q_{\text{sw}}^{\text{w}}$ to the surfzone heat budget had seasonal dependence, with a positive heat flux 47% of the time in winter, but only 11% of the time in summer. Usually at this location, Q_{wave} and $\Delta Q_{\text{sw}}^{\text{w}}$ together act to cool the surfzone relative to the inner-shelf.

On a flat and constantly sloping shallow beach, the average surfzone foam fraction can be scaled as a function of beach slope (4.20). Thus, surfzone averaged α_{sz} is independent of H_{s} and the albedo difference between the surfzone and where waves are not breaking is constant. The relationship between $\Delta Q_{\text{sw}}^{\text{w}}$ and Q_{sw}^{d} at the experiment site (Figure 4.10) predicts a surfzone

albedo 0.19 higher than the inner-shelf. The scaled albedo difference for a beach with constant (similar) slope has good agreement (within 0.04). Similar scalings are applied to the relative breaking wave surfzone heat flux contribution (4.22). The amount of additional surfzone cooling or heating relative to the inner-shelf is related to the ratio of $Q_{\mathrm{sw}}^{\mathrm{d}}$ to $H_{\mathrm{s}}^{3/2}$ at the outer surfzone boundary. Thus, for locations that are usually very sunny (few clouds and low latitudes) $Q_{\mathrm{sw}}^{\mathrm{d}}$ is high and waves act more to cool the surfzone. Conversely, in high latitudes, where there are clouds, or when $H_{\mathrm{sb}}^{3/2}$ is large, waves may heat the surfzone relative to the inner-shelf.

The Q_{wave} and $\Delta Q_{\mathrm{sw}}^{\mathrm{w}}$ contributions to the surfzone heat budget are uncorrelated, allowing the addition of just Q_{wave} to improve the fit to a surfzone heat budget [Sinnett and Feddersen, 2014]. A residual net surfzone cooling may be partially attributed to $\Delta Q_{\mathrm{sw}}^{\mathrm{w}}$, though breaking waves may also impact the surfzone sensible [MacMahan et al., 2018] and latent [Chickadel, 2018] heat fluxes. The wave-induced competing heat flux terms Q_{wave} and $\Delta Q_{\mathrm{sw}}^{\mathrm{w}}$ are large enough to have a significant effect on the surfzone heat budget.

4.7 Acknowledgments

This chapter is currently being prepared for publication with support from the National Science Foundation (Award Number 1558695) and the Office of Naval Research. B. Woodward, B. Boyd, K. Smith, R. Grenzeback, R. Walsh, and many volunteer scientific divers assisted with field work. Supplemental data was supplied by NOAA, CDIP, SCCOOS and CORDC with help from C. Olfe, B. O'Reilly and M. Otero. R. Clemesha, J. Norris, D. Grimes, S. Suanda provided feedback that significantly improved this chapter.

Chapter 4, in part, is currently being prepared for submission for publication of the material. Sinnett, G., F. Feddersen. The dissertation author was the primary investigator and author of this paper.

Bibliography

[Alberty et al., 2017] Alberty, M. S., Billheimer, S., Hamann, M. M., Ou, C. Y., Tamsitt, V., Lucas, A. J., and Alford, M. H. (2017). A reflecting, steepening, and breaking internal tide in a submarine canyon. *Journal of Geophysical Research: Oceans*, pages n/a–n/a.

[Almar et al., 2010] Almar, R., Castelle, B., Ruessink, B., Sénéchal, N., Bonneton, P., and Marieu, V. (2010). Two- and three-dimensional double-sandbar system behaviour under intense wave forcing and a meso–macro tidal range. *Continental Shelf Research*, 30(7):781 – 792.

[Andreas, 2011] Andreas, E. L. (2011). Fallacies of the enthalpy transfer coefficient over the ocean in high winds. *Journal of the Atmospheric Sciences*, 68(7):1435–1445.

[Andreas, 2016] Andreas, E. L. (2016). Sea spray generation at a rocky shoreline. *Journal of Applied Meteorology and Climatology*, 55(9):2037–2052.

[Andreas et al., 2008] Andreas, E. L., Persson, P. O. G., and Hare, J. E. (2008). A bulk turbulent air-sea flux algorithm for high-wind, spray conditions. *J. Phys. Ocean.*, 38(7):1581–1596.

[Arthur, 1955] Arthur, R. S. (1955). Oscillations in sea temperature at Scripps and Oceanside piers. *Deep Sea Research (1953)*, 2(2):107 – 121.

[Arthur and Fringer, 2014] Arthur, R. S. and Fringer, O. B. (2014). The dynamics of breaking internal solitary waves on slopes. *J. Fluid Mech.*, 761:360–398.

[Arthur and Fringer, 2016] Arthur, R. S. and Fringer, O. B. (2016). Transport by breaking internal solitary waves on slopes. *J. Fluid Mech.*, 789:93–126.

[Austin, 1999] Austin, J. A. (1999). The role of the alongshore wind stress in the heat budget of the North Carolina inner shelf. *J. Geophys. Res.*, 104(C8):18187–18203.

[Austin and Lentz, 1999] Austin, J. A. and Lentz, S. J. (1999). The relationship between synoptic weather systems and meteorological forcing on the north carolina inner shelf. *Journal of Geophysical Research: Oceans*, 104(C8):18159–18185.

[Battjes, 1975] Battjes, J. (1975). Modeling of turbulence in the surfzone. In *Proc. Symposium Modeling Techniques*, pages 1050–1061. ASCE.

[Battjes and Stive, 1985] Battjes, J. A. and Stive, M. J. F. (1985). Calibration and verification of a dissipation model for random breaking waves. *Journal of Geophysical Research: Oceans*, 90(C5):9159–9167.

[Beardsley et al., 1998] Beardsley, R. C., Dever, E. P., Lentz, S. J., and Dean, J. P. (1998). Surface heat flux variability over the northern california shelf. *Journal of Geophysical Research: Oceans*, 103(C10):21553–21586.

[Boehm, 2003] Boehm, A. B. (2003). Model of microbial transport and inactivation in the surf zone and application to field measurements of total coliform in northern orange county, california. *Environmental Science & Technology*, 37(24):5511–5517. PMID: 14717158.

[Boehm et al., 2002] Boehm, A. B., Grant, S. B., Kim, J. H., McGee, C. D., Mowbray, S., Clark, C., Foley, D., and Wellmann, D. (2002). Decadal and shorter period variability of surfzone water quality at Huntington Beach, California. *Environ. Sci. Technol.*, 36:3885–3892.

[Boehm et al., 2004] Boehm, A. B., Lluch-Cota, D. B., Davis, K. A., Winant, C. D., and Monismith, S. G. (2004). Covariation of coastal water temperature and microbial pollution at interannual to tidal periods. *Geophysical Research Letters*, 31(6). L06309.

[Bourgault et al., 2007] Bourgault, D., Blokhina, M. D., Mirshak, R., and Kelley, D. E. (2007). Evolution of a shoaling internal solitary wavetrain. *Geophysical Research Letters*, 34(3).

[Bourgault et al., 2011] Bourgault, D., Janes, D. C., and Galbraith, P. S. (2011). Observations of a large-amplitude internal wave train and its reflection off a steep slope. *Journal of Physical Oceanography*, 41(3):586–600.

[Bourgault et al., 2008] Bourgault, D., Kelley, D. E., and Galbraith, P. S. (2008). Turbulence and boluses on an internal beach. *Journal of Marine Research*, 66(5):563–588.

[Bourgault et al., 2014] Bourgault, D., Morsilli, M., Richards, C., Neumeier, U., and Kelley, D. (2014). Sediment resuspension and nepheloid layers induced by long internal solitary waves shoaling orthogonally on uniform slopes. *Continental Shelf Research*, 72:21 – 33.

[Briegleb et al., 1986] Briegleb, B., Minnis, P., Ramanathan, V., and Harrison, E. (1986). Comparison of regional clear-sky albedos inferred from satelliete observations and model computations. *Journal of Climate and Applied Meteorology*, 25:214–226.

[Broitman et al., 2005] Broitman, B., Blanchette, C., and Gaines, S. (2005). Recruitment of intertidal invertebrates and oceanographic variability at Santa Cruz Island, California. *Limnology and Oceanography*, 50(5):1473–1479.

[Carini et al., 2015] Carini, R. J., Chickadel, C. C., Jessup, A. T., and Thomson, J. (2015). Estimating wave energy dissipation in the surf zone using thermal infrared imagery. *Journal of Geophysical Research: Oceans*, 120(6):3937–3957.

[CERES, 2018] CERES (2018). Clouds and the Earth's Radiant Energy System. https://ceres.larc.nasa.gov/index.php.

[Chickadel, 2018] Chickadel, C. (2018). Personel Comm. email interview.

[Chickadel et al., 2003] Chickadel, C. C., Holman, R. A., and Freilich, M. H. (2003). An optical technique for the measurement of longshore currents. *Journal of Geophysical Research: Oceans*, 108(C11):n/a–n/a. 3364.

[Church and Thornton, 1993] Church, J. and Thornton, E. (1993). Effects of breaking wave-induced turbulence within a longshore-current model. *Coastal Eng.*, 20(1-2):1–28.

[Coakley and Davies, 1986] Coakley, J. A. and Davies, R. (1986). The effect of cloud sides on reflected solar radiation as deduced from satellite observations. *Journal of the Atmospheric Sciences*, 43(10):1025–1035.

[Dalrymple et al., 2011] Dalrymple, R. A., MacMahan, J. H., Reniers, A. J., and Nelko, V. (2011). Rip currents. *Annual Review of Fluid Mechanics*, 43(1):551–581.

[D'Asaro et al., 2007] D'Asaro, E. A., Lien, R.-C., and Henyey, F. (2007). High-frequency internal waves on the Oregon continental shelf. *Journal of Physical Oceanography*, 37(7):1956–1967.

[Davies, 1978] Davies, R. (1978). The effect of finite geometry on the three-dimensional transfer of solar irradiance in clouds. *Journal of the Atmospheric Sciences*, 35(9):1712–1725.

[Davis et al., 2017] Davis, K. A., Arthur, R. S., Reid, E. C., DeCarlo, T. M., and Cohen, A. L. (2017). Fate of internal waves on a shallow shelf. *Nature Communications*. submitted.

[Davis et al., 2011] Davis, K. A., Lentz, S. J., Pineda, J., Farrar, J. T., Starczak, V. R., and Churchill, J. H. (2011). Observations of the thermal environment on Red Sea platform reefs: A heat budget analysis. *Coral Reefs*, 30(1, SI):25–36.

[Deigaard, 1993] Deigaard, R. (1993). A note on the three dimensional shear stress distribution in a surfzone. *Coastal Engineering*, 20:157–171.

[Desaubies, 1975] Desaubies, Y. J. F. (1975). A linear theory of internal wave spectra and coherences near the Väisälä frequency. *Journal of Geophysical Research*, 80(6):895–899.

[Dever and Lentz, 1994] Dever, E. P. and Lentz, S. J. (1994). Heat and salt balances over the Northern California shelf in winter and spring. *Journal of Geophysical Research: Oceans*, 99(C8):16001–16017.

[Dorfman and Rosselot, 2009] Dorfman, M. and Rosselot, K. S. (2009). Testing the Waters: A guide to water quality at vacation beaches. Technical Report http://marineeconomics.noaa.gov/SCBeach/laobeach1.html, National Resrouces Defense Council.

[Elgar et al., 2001] Elgar, S., Guza, R. T., O'Reilly, W. C., Raubenheimer, B., and Herbers, T. H. C. (2001). Wave energy and direction observed near a pier. *J. Waterw. Port Coastal Ocean Eng.*, 127:2–6.

[Elgar et al., 1994] Elgar, S., Herbers, T., and Guza, R. T. (1994). Reflection of ocean surface gravity waves from a natural beach. *J. Phys. Ocean.*, 24:1503–1511.

[Etter et al., 2004] Etter, P. C., Howard, M. K., and Cochrane, J. D. (2004). Heat and freshwater budgets of the texaslouisiana shelf. *Journal of Geophysical Research: Oceans*, 109(C02024).

[Fairall et al., 2003] Fairall, C., Bradley, E., Hare, J., Grachev, A., and Edson, J. (2003). Bulk parameterization of air-sea fluxes: Updates and verification for the coare algorithm. *Journal of Climate*, 16(4):571–591.

[Fairall et al., 1996] Fairall, C., Bradley, E., Rogers, D., Edson, J., and Young, G. (1996). Bulk parameterization of air-sea fluxes for tropical ocean-global atmosphere coupled-ocean atmosphere response experiment. *Journal of Geophysical Research*, 101(C2):3747–3764.

[Feddersen, 2012a] Feddersen, F. (2012a). Observations of the surfzone turbulent dissipation rate. *J. Phys. Ocean.*, 42:386–399.

[Feddersen, 2012b] Feddersen, F. (2012b). Scaling surfzone dissipation. *Geophys. Res. Lett.*, 39(L18613).

[Feddersen and Guza, 2003] Feddersen, F. and Guza, R. T. (2003). Observations of nearshore circulation: Alongshore uniformity. *J. Geophys. Res.*, 108.

[Feddersen et al., 1998] Feddersen, F., Guza, R. T., Elgar, S., and Herbers, T. H. C. (1998). Alongshore momentum balances in the nearshore. *J. Geophys. Res.*, 103:15,667–15,676.

[Feddersen and Trowbridge, 2005] Feddersen, F. and Trowbridge, J. H. (2005). The effect of wave breaking on surf-zone turbulence and alongshore currents: a modelling study. *J. Phys. Ocean.*, 35:2187–2204.

[Fewings and Lentz, 2011] Fewings, M. R. and Lentz, S. J. (2011). Summertime cooling of the shallow continental shelf. *J. Geophys. Res.*, 116(C7).

[Fiedler et al., 2015] Fiedler, J. W., Brodie, K. L., McNinch, J. E., and Guza, R. T. (2015). Observations of runup and energy flux on a low-slope beach with high-energy, long-period ocean swell. *Geophysical Research Letters*, 42(22):9933–9941.

[Fischer and Thatje, 2008] Fischer, S. and Thatje, S. (2008). Temperature-induced oviposition in the brachyuran crab Cancer setosus along a latitudinal cline: Aquaria experiments and analysis of field-data. *J. Experimental Marine Biology and Ecology*, 357(2):157–164.

[Frouin et al., 2001] Frouin, R., Iacobellis, S. F., and Deschamps, P.-Y. (2001). Influence of oceanic whitecaps on the global radiation budget. *Geophysical Research Letters*, 28(8):1523–1526.

[Frouin et al., 1996] Frouin, R., Schwindling, M., and Deschamps, P.-Y. (1996). Spectral reflectance of sea foam in the visible and near-infrared: In situ measurements and remote sensing implications. *J. Geophys. Res.*, 101(C6):14361–14371.

[García-Medina et al., 2017] García-Medina, G., Özkan-Haller, H. T., Holman, R. A., and Ruggiero, P. (2017). Large runup controls on a gently sloping dissipative beach. *Journal of Geophysical Research: Oceans*, 122(7):5998–6010.

[Garrett and Kunze, 2007] Garrett, C. and Kunze, E. (2007). Internal tide generation in the deep ocean. *Annual Review of Fluid Mechanics*, 39(1):57–87.

[Goodwin et al., 2012] Goodwin, K. D., McNay, M., Cao, Y., Ebentier, D., Madison, M., and Griffith, J. F. (2012). A multi-beach study of Staphylococcus aureus, MRSA, and enterococci in seawater and beach sand. *Water Research*, 46(13):4195–4207.

[Haile et al., 1999] Haile, R. W., Witte, J. S., Gold, M., Cressey, R., McGee, C. D., Millikan, R. C., Glasser, A., Harawa, N., Ervin, C., Harmon, P., Harper, J., Dermand, J., J. Alamillo, K. B., Nides, M., and Wang, G. (1999). The health effects of swimming in ocean water contaminated by storm drain runoff. *Epidemiology*, 10:355–363.

[Halliday, 2012] Halliday, E. E. A. (2012). *Sands and environmental conditions impact the abundance and persistence of the fecal indicator bacteria Enterococcus at recreational beaches*. PhD thesis, Massachusetts Institute of Technology.

[Hally-Rosendahl et al., 2014] Hally-Rosendahl, K., Feddersen, F., and Guza, R. T. (2014). Cross-shore tracer exchange between the surfzone and the inner-shelf. *J. Geophys. Res.* submitted.

[Hansen et al., 1983] Hansen, J., Russell, G., Rind, D., Stone, P., Lacis, A., Lebedeff, S., Ruedy, R., and Travis, L. (1983). Efficient three-dimensional global models for climate studies: Models i and ii. *Mon. Weather Rev*, 111:609–662.

[Helfrich, 1992] Helfrich, K. R. (1992). Internal solitary wave breaking and run-up on a uniform slope. *J. Fluid Mech.*, 243:133–154.

[Hokajarvi et al., 2013] Hokajarvi, A.-M., Pitkanen, T., Siljanen, H. M. P., Nakari, U.-M., Torvinen, E., Siitonen, A., and Miettinen, I. T. (2013). Occurrence of thermotolerant Campylobacter spp. and adenoviruses in Finnish bathing waters and purified sewage effluents. *Journal of Water and Health*, 11(1):120–134.

[Holland et al., 1997] Holland, K., Holman, R., Lippmann, T., Stanley, J., and Plant, N. (1997). Practical use of video imagery in nearshore oceanographic field studies. *Oceanic Engineering, IEEE Journal of*, 22(1):81–92.

[Holland and Holman, 1993] Holland, K. T. and Holman, R. A. (1993). The statistical distribution of swash maxima on natural beaches. *Journal of Geophysical Research: Oceans*, 98(C6):10271–10278.

[Holloway et al., 1999] Holloway, P. E., Pelinovsky, E., and Talipova, T. (1999). A generalized Korteweg-de Vries model of internal tide transformation in the coastal zone. *Journal of Geophysical Research: Oceans*, 104(C8):18333–18350.

[Inman et al., 1976] Inman, D., Nordstrom, C., and Flick, R. (1976). Currents in submarine canyons: An air-sea-land interaction. *Annual Review of Fluid Mechanics*, 8(1):275–310.

[Jaffe et al., 2017] Jaffe, J. S., Franks, P. J. S., Roberts, P. L. D., Mirza, D., Schurgers, C., Kastner, R., and Boch, A. (2017). A swarm of autonomous miniature underwater robot drifters for exploring submesoscale ocean dynamics. *Nature Communications*, 8.

[Jin et al., 2004] Jin, Z., Charlock, T., Smith, W., and Rutledge, K. (2004). A parameterization of ocean surface albedo. *Geophysical Research Letters*, 31(22).

[Jin et al., 2011] Jin, Z., Qiao, Y., Wang, Y., Fang, Y., and Yi, W. (2011). A new parameterization of spectral and broadband ocean surface albedo. *Optics Express*, 19(27).

[Josey et al., 1997] Josey, S. A., Oakley, D., and Pascal, R. W. (1997). On estimating the atmospheric longwave flux at the ocean surface from ship meteorological reports. *Journal of Geophysical Research*, 102(C13):27,961–27,972.

[Kim et al., 2010] Kim, T., Cho, Y., You, K., and Jung, K. (2010). Effect of tidal flat on seawater temperature variation in the southwest coast of korea. *Journal of Geophysical Research*, 115(C02007).

[Koepke, 1984] Koepke, P. (1984). Effective reflectance of oceanic whitecaps. *Applied Optics*, 23(11).

[Kumar and Feddersen, 2017] Kumar, N. and Feddersen, F. (2017). The effect of stokes drift and transient rip currents on the inner shelf. part ii: With stratification. *Journal of Physical Oceanography*, 47(1):243–260.

[Leichter et al., 1996] Leichter, J., Wing, S., Miller, S., and Denny, M. (1996). Pulsed delivery of subthermocline water to conch reef (Florida Keys) by internal tidal bores. *Limnology and Oceanography*, 41(7):1490–1501.

[Lennert-Cody and Franks, 1999] Lennert-Cody, C. E. and Franks, P. J. (1999). Plankton patchiness in high-frequency intenral waves. *Marine Ecology Progress Series*, 186:59–66.

[Lentz, 1987] Lentz, S. J. (1987). A heat budget for the Northern California shelf during CODE 2. *J. Geophys. Res.*, 92(C13):14491–14509.

[Lerczak et al., 2003] Lerczak, J. A., Winant, C. D., and Hendershott, M. C. (2003). Observations of the semidiurnal internal tide on the southern california slope and shelf. *Journal of Geophysical Research*, 108(C3).

[Lilly, 2016] Lilly, J. M. (2016). jlab: A data analysis package for matlab, v. 1.6.2. *http://www.jmlilly.net/jmlsoft.html*.

[Lippmann and Holman, 1990] Lippmann, T. and Holman, R. (1990). The spatial and temporal variability of sand-bar morphology. *J. Geophys. Res.*, 95(C7):11575–11590.

[Lucas et al., 2011a] Lucas, A., Dupont, C., Tai, V., Largier, J. L., Palenik, B., and Franks, P. J. (2011a). The green ribbon: Multiscale physical control of phytoplankton productivity and community structure over a narrow continental shelf. *Limnology and Oceanography*, 56(2):611–626.

[Lucas et al., 2011b] Lucas, A., Franks, P., and Dupont, C. (2011b). Horizontal internal-tide fluxes support elevated phytoplankton productivity over the inner continental shelf. *Limnology and Oceangraphy: Fluids and Environment*, 1:56–74.

[Ludka et al., 2015] Ludka, B. C., Guza, R. T., O'Reilly, W. C., and Yates, M. L. (2015). Field evidence of beach profile evolution toward equilibrium. *J. Geophys. Res., Oceans*, 120.

[Ma et al., 2011] Ma, G., Shi, F., and Kirby, J. T. (2011). A polydisperse two-fluid model for surf zone bubble simulation. *Journal of Geophysical Research: Oceans*, 116(C5):n/a–n/a. C05010.

[MacKinnon and Gregg, 2005] MacKinnon, J. A. and Gregg, M. C. (2005). Spring mixing: Turbulence and internal waves during restratification on the new england shelf. *Journal of Physical Oceanography*, 35(12):2425–2443.

[MacMahan et al., 2018] MacMahan, J., Thornton, E., Koscinski, J., and Wang, Q. (2018). Field observations and modeling of surf zone sensible heat flux. *Journal of Applied Meteorology and Climatology*, 0(0):10.1175/JAMC–D–17–0228.1.

[Marino et al., 2005] Marino, B., Thomas, L., and Linden, P. (2005). The front condition for gravity currents. *J. Fluid Mech.*, 536:49–78.

[Marleau et al., 2014] Marleau, L. J., Flynn, M. R., and Sutherland, B. R. (2014). Gravity currents propagating up a slope. *Physics of Fluids*, 26(4):046605.

[Masunaga et al., 2015] Masunaga, E., Homma, H., Yamazaki, H., Fringer, O. B., Nagai, T., Kitade, Y., and Okayasu, A. (2015). Mixing and sediment resuspension associated with internal bores in a shallow bay. *Continental Shelf Research*, 110:85 – 99.

[Maurer et al., 2010] Maurer, B. D., Bolster, D. T., and Linden, P. F. (2010). Intrusive gravity currents between two stably stratified fluids. *Journal of Fluid Mechanics*, 647:53–69.

[McPhee-Shaw and Kunze, 2002] McPhee-Shaw, E. E. and Kunze, E. (2002). Boundary layer intrusions from a sloping bottom: A mechanism for generating intermediate nepheloid layers. *Journal of Geophysical Research: Oceans*, 107(C6).

[Monahan et al., 1986] Monahan, E., Niocaill, G., and Koepke, P. (1986). *Oceanographic Sciences Library*, volume 2, pages 251–260. Springer Netherlands.

[Monahan, 1971] Monahan, E. C. (1971). Oceanic whitecaps. *Journal of Physical Oceanography*, 1(2):139–144.

[Monahan and Muircheartaigh, 1980] Monahan, E. C. and Muircheartaigh, I. (1980). Optimal power-law description of oceanic whitecap coverage dependence on wind speed. *Journal of Physical Oceanography*, 10(12):2094–2099.

[Moore et al., 2016] Moore, C. D., Koseff, J. R., and Hult, E. L. (2016). Characteristics of bolus formation and propagation from breaking internal waves on shelf slopes. *Journal of Fluid Mechanics*, 791:260–283.

[Moore et al., 2000] Moore, K. D., Voss, K. J., and Gordon, H. R. (2000). Spectral reflectance of whitecaps: Their contribution to water-leaving radiance. *Journal of Geophysical Research: Oceans*, 105(C3):6493–6499.

[Moum et al., 2003] Moum, J., Farmer, D., Smyth, W., Armi, L., and Vagle, S. (2003). Structure and generation of turbulence at interfaces strained by internal solitary waves propagating shoreward over the continental shelf. *JOURNAL OF PHYSICAL OCEANOGRAPHY*, 33(10):2093–2112.

[Moum et al., 2007] Moum, J. N., Klymak, J. M., Nash, J. D., Perlin, A., and Smyth, W. D. (2007). Energy transport by nonlinear internal waves. *Journal of Physical Oceanography*, 37(7):1968–1988.

[Nam and Send, 2011] Nam, S. and Send, U. (2011). Direct evidence of deep water intrusions onto the continental shelf via surging internal tides. *J. Geophys. Res.*, 116.

[Nash et al., 2012] Nash, J. D., Kelly, S. M., Shroyer, E. L., Moum, J. N., and Duda, T. F. (2012). The unpredictable nature of internal tides on continental shelves. *J. Phys. Ocean.*, 42(11):1981–2000.

[Omand et al., 2012] Omand, M. M., Feddersen, F., Franks, P. J. S., and Guza, R. T. (2012). Episodic vertical nutrient fluxes and nearshore phytoplankton blooms in Southern California. *Limnol. Oceanogr.*, 57:1673–1688.

[Omand et al., 2011] Omand, M. M., Leichter, J. J., Franks, P. J. S., Lucas, A. J., Guza, R. T., and Feddersen, F. (2011). Physical and biological processes underlying the sudden appearance of a red-tide surface patch in the nearshore. *Limnol. Oceanogr.*, 56:787–801.

[O'Reilly and Guza, 1991] O'Reilly, W. and Guza, R. (1991). Comparison of spectral refraction and refraction-diffraction wave models. *Journal of Waterway Port Coastal and Ocean Engineering-ASCE*, 117(3):199–215.

[O'Reilly et al., 2016] O'Reilly, W., Olfe, C. B., Thomas, J., Seymour, R., and Guza, R. (2016). The california coastal wave monitoring and prediction system. *Coastal Engineering*, 116:118 – 132.

[O'Reilly, W.C. and Guza, R.T., 1998] O'Reilly, W.C. and Guza, R.T. (1998). Assimilating coastal wave observations in regional swell predictions. Part I: Inverse methods. *J. Phys. Ocean.*, 28:679–691.

[Payne, 1972] Payne, R. E. (1972). Albedo of the sea surface. *J. Atmos. Sci.*, 29:959–970.

[Phillips, 2005] Phillips, N. (2005). Growth of filter-feeding benthic invertebrates from a region with variable upwelling intensity. *Marine Ecology Progress Series*, 295:79–89.

[Pineda, 1991] Pineda, J. (1991). Predictable upwelling and the shoreward transport of planktonic larvae by internal tidal bores. *Science*, 253(5019):548–551.

[Pineda, 1994] Pineda, J. (1994). Internal tidal bores in the nearshore - warm-water fronts, seaward gravity currents and the onshore transport of neustonic larvae. *J. Marine Res.*, 52(3):427–458.

[Pineda, 1999] Pineda, J. (1999). Circulation and larval distribution in internal tidal bore warm fronts. *Limnology and Oceanography*, 44(6):1400–1414.

[Puleo et al., 2000] Puleo, J. A., Beach, R. A., Holman, R. A., and Allen, J. S. (2000). Swash zone sediment suspension and transport and the importance of bore-generated turbulence. *Journal of Geophysical Research: Oceans*, 105(C7):17021–17044.

[Quaresma et al., 2007] Quaresma, L. S., Vitorino, J., Oliveira, A., and da Silva, J. (2007). Evidence of sediment resuspension by nonlinear internal waves on the western portuguese mid-shelf. *Marine Geology*, 246(2):123 – 143.

[Raubenheimer and Guza, 1996] Raubenheimer, B. and Guza, R. T. (1996). Observations and predictions of run-up. *Journal of Geophysical Research: Oceans*, 101(C11):25575–25587.

[Reda and Andreas, 2008] Reda, I. and Andreas, A. (2008). Solar position algorithm for solar radiation applications (revised). Technical report, National Renewable Energy Laboratory, Golden, CO.

[Richards et al., 2013] Richards, C., Bourgault, D., Galbraith, P. S., Hay, A., and Kelley, D. E. (2013). Measurements of shoaling internal waves and turbulence in an estuary. *Journal of Geophysical Research: Oceans*, 118(1):273–286.

[Richter and Stern, 2014] Richter, D. H. and Stern, D. P. (2014). Evidence of spraymediated airsea enthalpy flux within tropical cyclones. *Geophysical Research Letters*, 41:2997–3003.

[Rinehimer and Thomson, 2014] Rinehimer, J. and Thomson, J. T. (2014). Observations and modeling of heat fluxes on tidal flats. *Journal of Geophysical Research: Oceans*, 119:1–14.

[Rippy et al., 2013] Rippy, M., Franks, P., Feddersen, F., Guza, R., and Moore, D. (2013). Factors controlling variability in nearshore fecal pollution: The effects of mortality. *Marine Pollution Bulletin*, 66(1):191 – 198.

[Rippy et al., 013a] Rippy, M. A., Franks, P. J. S., Feddersen, F., Guza, R. T., and Moore, D. F. (2013a). Factors controlling variability in nearshore fecal pollution: Fecal indicator bacteria as passive particles. *Mar. Poll. Bull.*, 66:151–157.

[Rippy et al., 013b] Rippy, M. A., Franks, P. J. S., Feddersen, F., Guza, R. T., and Moore, D. F. (2013b). Factors controlling variability in nearshore fecal pollution: The effects of mortality. *Marine Pollution Bulletin*, 66(1-2):191–198.

[Ross and Dion, 2007] Ross, V. and Dion, D. (2007). Sea surface slope statistics derived from sun glint radiance measurements and their apparent dependence on sensor elevation. *Journal of Geophysical Research: Oceans*, 112(C9):n/a–n/a. C09015.

[Ruessink et al., 2003] Ruessink, B., Walstra, D., and Southgate, H. (2003). Calibration and verification of a parametric wave model on barred beaches. *Coastal Engineering*, 48(3):139 – 149.

[Ruessink, 2010] Ruessink, B. G. (2010). Observations of turbulence within a natural surf zone. *J. Phys. Ocean.*, 40(12):2696–2712.

[Ruessink et al., 2001] Ruessink, B. G., Miles, J. R., Feddersen, F., Guza, R. T., and Elgar, S. (2001). Modeling the alongshore current on barred beaches. *J. Geophys. Res.*, 106:22,451–22,463.

[Saunders, 1967] Saunders, P. M. (1967). Shadowing on the ocean and the existence of the horizon. *J. Geophys. Res.*, 72(18):4643–4649.

[Senechal et al., 2011] Senechal, N., Coco, G., Bryan, K. R., and Holman, R. A. (2011). Wave runup during extreme storm conditions. *Journal of Geophysical Research: Oceans*, 116(C7):n/a–n/a. C07032.

[Shepard et al., 1974] Shepard, F., Marshall, N., and McLoughlin, P. (1974). Currents in submarine canyons. *Deep-Sea Research*, 21:691–706.

[Shin et al., 2004] Shin, J. O., Dalziel, S. B., and Linden, P. (2004). Gravity currents produced by lock exchange. *J. Fluid Mech.*, 521:1–34.

[Shroyer et al., 2011] Shroyer, E., Moum, J., and Nash, J. (2011). Nonlinear internal waves over New Jersey's continental shelf. *J. Geophys. Res.*, 116(C03022).

[Shroyer et al., 2010] Shroyer, E. L., Moum, J. N., and Nash, J. D. (2010). Vertical heat flux and lateral mass transport in nonlinear internal waves. *Geophysical Research Letters*, 37(L08601).

[Sinnett and Feddersen, 2014] Sinnett, G. and Feddersen, F. (2014). The surf zone heat budget: The effect of wave heating. *Geophysical Research Letters*, 41(20):7217–7226.

[Sinnett and Feddersen, 2016] Sinnett, G. and Feddersen, F. (2016). Observations and parameterizations of surfzone albedo. *Methods in Oceanography*, 17:319 – 334.

[Sinnett et al., 2018] Sinnett, G., Feddersen, F., Lucas, A. J., Pawlak, G., and Terrill, E. (2018). Observations of nonlinear internal wave run-up to the surfzone. *Journal of Physical Oceanography*, 48(3):531–554.

[Sinton et al., 1994] Sinton, L., Davies-Colley, R., and Bell, R. G. (1994). Inactivation of enterococci and fecal coliforms from sewage and meatworks effluents in seawater chambers. *Applied and Environmental Microbiology*, 60(6):2040–2048.

[Sinton et al., 2002] Sinton, L., Hall, C., Lynch, P., and Davies-Colley, R. (2002). Sunlight inactivation of fecal indicator bacteria and bacteriophages from waste stabilization pond effluent in fresh and saline waters. *Applied and Environmental Microbiology*, 68(3):1122–1131.

[Sinton et al., 1999] Sinton, L. W., Finlay, R. K., and Linch, F. A. (1999). Sunlight inactivation of fecal bacteriophages and bacteria in sewage-polluted seawater. *Appl. Environ. Microbiol.*, 65(8):3605–3613.

[Smith and Largier, 1995] Smith, J. A. and Largier, J. L. (1995). Observations of nearshore circulation: Rip currents. *Journal of Geophysical Research: Oceans*, 100(C6):10967–10975.

[Stanton and Ostrovsky, 1998] Stanton, T. P. and Ostrovsky, L. A. (1998). Observations of highly nonlinear internal solitons over the continental shelf. *Geophysical Research Letters*, 25(14):2695–2698.

[Stockdon and Holman, 2000] Stockdon, H. F. and Holman, R. A. (2000). Estimation of wave phase speed and nearshore bathymetry from video imagery. *Journal of Geophysical Research: Oceans*, 105(C9):22015–22033.

[Stockdon et al., 2006] Stockdon, H. F., Holman, R. A., Howd, P. A., and Sallenger, A. H. (2006). Empirical parameterization of setup, swash, and runup. *Coastal Engineering*, 53(7):573 – 588.

[Suanda and Barth, 2015] Suanda, S. H. and Barth, J. A. (2015). Semidiurnal baroclinic tides on the central Oregon inner shelf. *J. Phys. Ocean.* revised.

[Suanda et al., 2014] Suanda, S. H., Barth, J. A., Holman, R. A., and Stanley, J. (2014). Shore-based video observations of nonlinear internal waves across the inner shelf. *Journal of Atmospheric and Oceanic Technology*, 31:714–728.

[Surbeck, 2009] Surbeck, C. Q. (2009). Factors influencing the challenges of modelling and treating fecal indicator bacteria in surface waters. *Ecohydrology*, 2(4):399–403.

[Sutherland et al., 2013a] Sutherland, B., Barrett, K., and Ivey, G. (2013a). Shoaling internal solitary waves. *Journal of Geophysical Research: Oceans*, 118:4111–4124.

[Sutherland et al., 2013b] Sutherland, B. R., Polet, D., and Campbell, M. (2013b). Gravity currents shoaling on a slope. *Physics of Fluids*, 25(8):086604.

[Taylor et al., 1996] Taylor, J., Edwards, J., Glew, M., Hignett, P., and Slingo, A. (1996). Studies withi a flexible new radiation code. ii: Comparisons with aircraft short-wave observations. *Q. J. R. Meteorol. Soc.*, 122:839–861.

[Thomson, 1982] Thomson, D. J. (1982). Spectrum estimation and harmonic analysis. *Proceedings of the IEEE*, 70:1055–1096.

[Thomson, 1946] Thomson, G. W. (1946). The antoine equation for vapor pressure data. *Chemical Reviews*, 38(1):1–39.

[Thornton and Guza, 1983] Thornton, E. B. and Guza, R. T. (1983). Transformation of wave height distribution. *J. Geophys. Res.*, 88(C10):5925–5938.

[Thorpe, 1999] Thorpe, S. (1999). The generation of alongslope currents by breaking internal waves. *J. Phys. Ocean.*, 29:29–38.

[van Eijk et al., 2011a] van Eijk, A. M. J., Kusmierczyk-Michulec, J. T., Francius, M. J., Tedeschi, G., Piazzola, J., Merritt, D. L., and Fontana, J. D. (2011a). Sea-spray aerosol particles generated in the surf zone. *Journal of Geophysical Research*, 116(D19210).

[van Eijk et al., 2011b] van Eijk, A. M. J., KusmierczykMichulec, J. T., Francius, M. J., Tedeschi, G., Piazzola, J., Merritt, D. L., and Fontana, J. D. (2011b). Seaspray aerosol particles generated in the surf zone. *Journal of Geophysical Research: Atmospheres*, 116(D19).

[van Haren et al., 2012] van Haren, H., Gostiaux, L., Laan, M., van Haren, M., van Haren, E., and Gerringa, L. J. A. (2012). Internal wave turbulence near a texel beach. *PLOS ONE*, 7(3).

[Veron, 2015] Veron, F. (2015). Ocean spray. *Annual Review of Fluid Mechanics*, 47(1):507–538.

[Wallace and Wilkinson, 1988] Wallace, B. and Wilkinson, D. (1988). Run-up of internal waves on a gentle slope in a two-layered system. *J. Fluid Mech.*, 191:419–442.

[Walstra et al., 1996] Walstra, D., Mocke, G. P., and Smit, F. (1996). Roller contributions as inferred from inverse modelling techniques. *Proceedings 25th International Coastal Engineering Conference*, pages 1205–1218.

[Walter et al., 2016] Walter, R. K., Stastna, M., Woodson, C. B., and Monismith, S. G. (2016). Observations of nonlinear internal waves at a persistent coastal upwelling front. *Continental Shelf Research*, 117:100 – 117.

[Walter et al., 2012] Walter, R. K., Woodson, C. B., Arthur, R. S., Fringer, O. B., and Monismith, S. G. (2012). Nearshore internal bores and turbulent mixing in southern Monterey Bay. *J. Geophys. Res.*, 117.

[Walter et al., 2014] Walter, R. K., Woodson, C. B., Leary, P. R., and Monismith, S. G. (2014). Connecting wind-driven upwelling and offshore stratification to nearshore internal bores and oxygen variability. *J. Geophys. Res., Oceans*, 119:3517–3534.

[White and Helfrich, 2014] White, B. L. and Helfrich, K. R. (2014). A model for internal bores in continuous stratification. *Journal of Fluid Mechanics*, 761:282–304.

[Whiteman and Allwine, 1986] Whiteman, C. and Allwine, K. (1986). Extraterrestrial solar radiation on inclined surfaces. *Environmental Software*, 1(3):164 – 169.

[Whitlock et al., 1982] Whitlock, C. H., Bartlett, D. S., and Gurganus, E. A. (1982). Sea foam reflectance and influence on optimum wavelength for remote sensing of ocean aerosols. *Geophysical Research Letters*, 9(6):719–722.

[Wilkin, 2006] Wilkin, J. L. (2006). The summertime heat budget and circulation of southeast new england shelf waters. *Journal of Physical Oceanography*, 36(11):1997–2011.

[Winant, 1974] Winant, C. (1974). Internal surges in coastal waters. *J. Geophys. Res.*, 79(30):4523–4526.

[Winant and Bratkovich, 1981] Winant, C. D. and Bratkovich, A. W. (1981). Temperature and Currents on the Southern California Shelf: A Description of the Variability. *Journal of Physical Oceanography*, 11(1):71–86.

[Winters et al., 1995] Winters, K. B., Lombard, P. N., Riley, J. J., and D'Asaro, E. A. (1995). Available potential energy and mixing in density-stratified fluids. *Journal of Fluid Mechanics*, 289:115–128.

[Wong et al., 2012] Wong, S. H. C., Santoro, A. E., Nidzieko, N. J., Hench, J. L., and Boehm, A. B. (2012). Coupled physical, chemical, and microbiological measurements suggest a connection between internal waves and surf zone water quality in the Southern California Bight. *Continental Shelf Research*, 34:64–78.

[Woodson et al., 2007] Woodson, C., Eerkes-Medrano, D., Flores-Morales, A., Foley, M., Henkel, S., Hessing-Lewis, M., Jacinto, D., Needles, L., Nishizaki, M., O'Leary, J., Ostrander, C., Pespeni, M., Schwager, K., Tyburczy, J., Weersing, K., Kirincich, A., Barth, J., McManus, M., and Washburn, L. (2007). Local diurnal upwelling driven by sea breezes in northern Monterey Bay. *Continental Shelf Research*, 27(18):2289 – 2302.

[Wunsch, 1996] Wunsch, C. (1996). *The Ocean Circulation Inverse Problem*. Cambridge University Press.

[Yates et al., 2009] Yates, M. L., Guza, R. T., and O'Reilly, W. C. (2009). Equilibrium shoreline response: Observations and modeling. *J. Geophys. Res.*, 114.

[Young et al., 2013] Young, A. P., Guza, R. T., Dickson, M. E., O'Reilly, W. C., and Flick, R. E. (2013). Ground motions on rocky, cliffed, and sandy shorelines generated by ocean waves. *J. Geophys. Res.*, 118(12):6590–6602.

[Zhang et al., 2015] Zhang, S., Alford, M. H., and Mickett, J. B. (2015). Characteristics, generation and mass transport of nonlinear internal waves on the washington continental shelf. *Journal of Geophysical Research: Oceans*, 120:741–758.

[Zhang et al., 2014] Zhang, Y., Wang, X., Hu, R., Pan, Y., and Zhang, H. (2014). Variation of albedo to soil moisture for sand dunes and biological soil crusts in arid desert ecosystems. *Environmental Earth Sciences*, 71(3):1281–1288.